Accurate and rapid gravitational waveform models for binary black hole coalescences

Von der QUEST-Leibniz-Forschungsschule
der Gottfried Wilhelm Leibniz Universität Hannover

zur Erlangung des Grades
DOKTORIN DER NATURWISSENSCHAFTEN
Dr. rer. nat

genehmigte
Dissertation
von
M.Sc. Yoshinta Eka Setyawati

2021

Referent	Dr. Frank Ohme Albert Einstein Institute Hannover
Korreferent	Prof. Dr. Harald Pfeiffer Albert Einstein Institute Potsdam
Korreferent	Prof. Dr. Badri Krishnan Radboud University Nijmegen, the Netherlands
Tag der Promotion	29 September 2021

“

Do you not know that in a race all the runners run, but only one gets the prize? Run in such a way as to get the prize.
Everyone who competes in the games goes into strict training. They do it to get a crown that will not last, but we do it to get a crown that will last forever.
Therefore I do not run like someone running aimlessly; I do not fight like a boxer beating the air. No, I strike a blow to my body and make it my slave so that after I have preached to others, I myself will not be disqualified for the prize.

”

1 Corinthians 9:24-27

Abstrakt

Der erste direkte Nachweis von Gravitationswellen durch LIGO und Virgo im Jahr 2015 markierte den Beginn der Ära der Gravitationswellenastronomie. Gravitationswellen sind ein hervorragendes Werkzeug, um die allgemeine Relativitätstheorie zu beweisen und die Dynamik kompakter Objekte im Universum zu enthüllen. Im Laufe der Jahre beobachten wir immer mehr Signale vom Verschmelzen von Doppelsystemen Schwarzer Löcher.

Die Signale der Detektoren werden durch zahlreiche Wellenformvorlagen gefiltert, die aus theoretischen Vorhersagen stammen. Einige Modelle sind genauer, aber langsam, und einige andere sind weniger genau, aber schnell. Die Anforderungen an die Genauigkeit, Geschwindigkeit und Parameterabdeckung der Wellenformmodelle steigen mit zunehmender Anzahl von Detektionen. Daher untersuchen wir Strategien, um die Wellenformerzeugung zu beschleunigen, ohne viel Genauigkeit für die zukünftige Signalanalyse zu verlieren. In dieser Dissertation stellen wir unseren Ansatz wie folgt vor:

1. Entwicklung einer Methode zur dynamischen Abstimmung eines weniger genauen (aber schnellen) Modells mit einem genaueren (aber langsamen) Modell durch eine iterative Technik zur Dimensionalitätsreduktion.

2. Untersuchung der Leistung von Regressionsmethoden, einschließlich maschinellem Lernen für höhere Dimensionen.

3. Hinzufügen der Exzentrizität zum quasizirkulären analytischen Modell durch eine Anpassungstechnik.

Wir analysieren die Zuverlässigkeit unserer Ergebnisse, sowie das Potential einer Beschleunigung der Wellenformerzeugung. Unsere Methoden können leicht angewendet werden, um die Komplexität und die Zeit für die Erstellung eines neuen Wellenformmodells zu reduzieren. Zusätzlich bauen wir ein Python-Paket `pyrex`, um die quasizirkuläre Berechnung welche sich in eine exzentrische wandelte zu übernehmen. Diese Studie ist entscheidend für die Entwicklung von Modellen, die mehr Parameter enthalten.

Stichwörter

Gravitationswelle, binäres schwarzes Loch, Wellenformmodellierung, Hauptkomponentenanalyse, Regression, maschinelles Lernen, Exzentrizität

Abstract

The first direct gravitational wave detection by LIGO and Virgo in 2015 marked the beginning of the gravitational wave astronomy era. Gravitational waves are an excellent tool to prove general relativity and unveil compact objects' dynamics in the universe. Over the years, we observe more signals from coalescing black hole binaries.

Signals from the detectors are filtered through numerous waveform templates coming from theoretical predictions. Some models are more accurate but slow, and the others are less accurate but fast. We face ever-increasing demands for accuracy, speed, and parameter coverage of waveform models with more detections. Thus, we investigate strategies to speed up waveform generation without losing much accuracy for future signal analysis. In this dissertation, we present our approach as follows:

1. developing a method to dynamically tune less accurate (but fast) models with a more accurate (but slow) models through an iterative dimensionality reduction technique,

2. investigating the performance of regression methods, including machine learning for higher dimensions,

3. adding eccentricity to quasicircular analytical models through fitting technique.

We analyze our results' faithfulness and prospects to speed up waveform generation. Our methods can readily be applied to reduce the complexity and time of building a new waveform model. Additionally, we build a python package `pyrex` to carry out the quasicircular turned eccentric computation. This study is crucial for the development of models which include more parameters.

Keywords

gravitational wave, binary black-hole, waveform modeling, principal component analysis, regression, machine learning, eccentricity

Contents

Preamble

Publications

Closure

Appendix

Additional Material

List of Tables

List of Figures

1.1 Systematic diagram of gravitational wave spectrum, sources, and detectors. 2
1.2 GW150914 signal in LIGO Hanford and Livingston. 4
1.3 Pictures of LIGO Hanford, Livingston, GEO600, and Virgo. . . . 5

2.1 Illustrative plot of the polarizations. 10
2.2 Schematic diagram an interferometer. 13
2.3 LIGO design sensitivity and noise curves. 15
2.4 Example of waveform model varies in mass ratios and spins. . . . 19
2.5 Schematic diagram of the align spin systems. 24
2.6 Systematic diagram of validity range for different approximations. 25
2.7 Schematic foliation of the spacetime manifold with three-dimensional hypersurfaces. 26
2.8 Moving puncture diagram in numerical simulations. 27
2.9 Systematic plot of a hybrid waveform. 30

List of Abbreviations

aLIGO advanced Laser Interferometer Gravitational-wave Observatory

ANN artificial neural networks

AZDHP aLIGO zero detuned high power density

BBH binary black-hole

BH black hole

BNS binary neutron star

CE Cosmic Explorer

EB enriched basis

EI empirical interpolation

EM electromagnetic

EMRI extreme mass ratio inspiral

EOB effective-one-body

EOS equation of state

ET Einstein Telescope

GMVP greedy multivariate polynomial fits

GPR Gaussian process regression

GR general relativity

GW gravitational wave

IMR inspiral-merger-ringdown

IMRI intermediate mass ratio inspiral

ISCO innermost stable circular orbit

LAL LIGO algorithm library

ML machine learning

MLP multi-layer-perceptron

NR numerical relativity

NS neutron star

NSF National Science Foundation

PCA principal component analysis

PE parameter estimation

PN post-Newtonian

PSD power spectral density

RBF radial basis functions

RBFN radial basis function network

RGI regular grid interpolator

ROM reduced-order model

ROQ reduced-order quadrature

SNR signal-to-noise ratio

SPA stationary-phase approximation

SVD singular value decomposition

TPI tensor-product interpolation

BSSNOK Baumgarte-Shapiro-Shibata-Nakamura-Oohara-Kojima

BSSN Baumgarte-Shapiro-Shibata-Nakamura

ADM Arnowitt-Deser-Misner

Preface

1 Introduction

"If you ask me whether there are gravitational waves or not, I must answer that I do not know, but it is a highly interesting problem."

Albert Einstein

The Einstein general theory of relativity, also known as general relativity (GR) provides a theoretical framework that describes the relationship between the distribution of matter, space, and time [1]. In GR, the spacetime curvature is strongly related to matter and radiation, producing energy and momentum. American physicist John Wheeler summarized the theory's core as "matter tells spacetime how to curve, and curved spacetime tells matter how to move" [2]. Consequently, gravity can be interpreted as a free fall in a curved spacetime due to uneven mass distribution.

In July 1905, Henri Poincaré proposed that gravity was transmitted through a wave and introduced the term gravitational wave (GW) [3]. Later in 1916, Einstein predicted the existence of GWs as a consequence of GR [1]. This phenomenon comes from a non-stationary mass distribution that deforms the curvature of spacetime and transports energy. GWs are spacetime waves oscillating perpendicular to the direction of propagation and moving at the speed of light. As GWs cross an observer, the observer will find spacetime distorted by GWs strain. It stretches in one direction and compresses the other direction simultaneously. We explain the GW strain and its derivation from GR in more detail in section 2.1.

Similar to electromagnetic (EM) waves, the GW spectrum range from low

($< 10^{-9}$Hz) to high frequencies (kHz). The frequency range covered by GWs highly depends on the source's type (see Fig. 1.1). Furthermore, the wave's properties such as amplitude, phase, and duration encode vital information about the astrophysical object behind it. We can trace the signal's origin, such as neutron stars (NSs) and black holes (BHs).

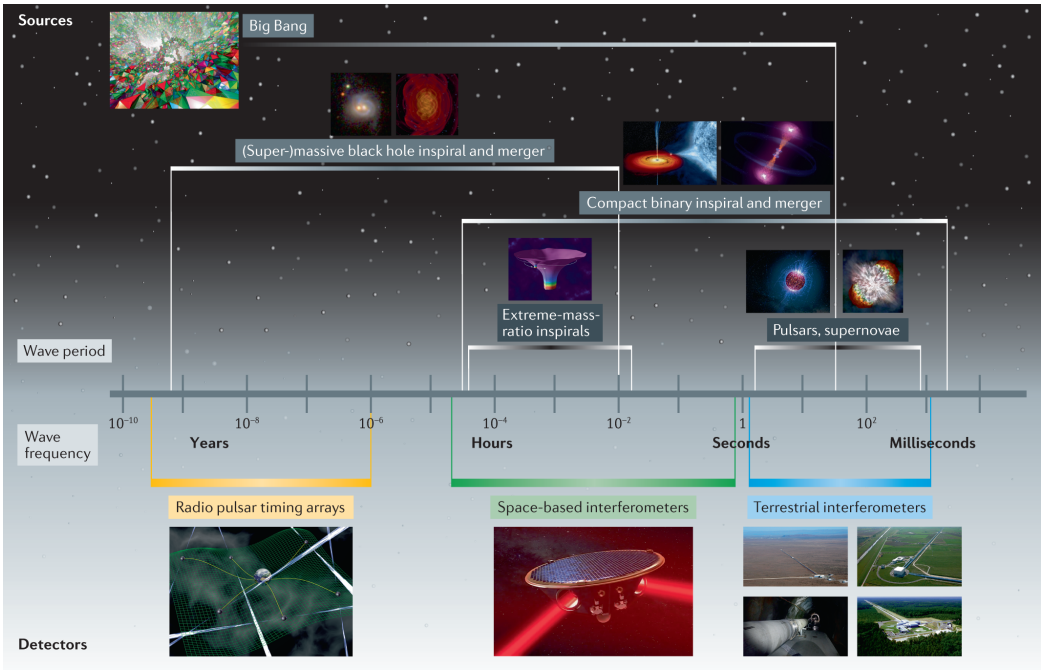

Figure 1.1: GW spectrum, wavelength, frequency ranges, sources, and detectors [4].

A NS is a compact remnant of a massive star that has reached the end of its life. It has high density because of the extreme amount of matter compressed into a small volume. Thus, it has a strong gravitational pull. Due to subatomic glue, the behavior of matter inside the NS's core is still unknown. Hence, a NS is a perfect natural laboratory to study the interaction of the four fundamental forces[1] in such an extreme condition. A possible hint to this problem is constraining the mass-radius relation determined by the equation of state (EOS). GWs radiated from a binary neutron-star (BNS) collision can be used to constraint their EOS [5].

A BH is a dense object with extreme gravitational fields. The gravity is very strong due to enormous mass squeezed into a tiny volume, preventing matter and even light to escape from it. The no escape boundary is called the *event horizon*. GR predicts that the presence of such a dense object would deform its surrounding spacetime. In astronomy, BHs are classified by their total masses, namely

[1] electromagnetism, gravity, weak force, and strong force.

miniature, stellar, intermediate, and supermassive BHs. This dissertation focuses on GW radiated by the collision of two stellar-mass BHs, where each body has a mass between several to several tens of solar masses [6].

Proving the existence of GWs was one of the most ambitious projects in the physics community. We can use GWs to test GR and to understand various phenomena in our universe. Important applications include

- the behavior of matter in the strong-field regime,
- the nature of compact objects,
- the dynamical evolution of black-hole binaries, and
- the expansion of the Universe by constraining the Hubble constant.

Thus, detecting GWs is a key to open a new chapter in physics and astronomy.

The 1993 Nobel-winning research gave the first indirect evidence of GWs by observing the orbital decay of two spinning NSs known as the Hulse-Taylor binary [7]. The first direct detection of GWs was made on 14 September 2015 (see Fig. 1.2). The signal originated from a coalescing binary black-hole (BBH) [8]. The frequency range of the signals is within the sensitivity of the ground-based detectors[2], LIGO, Virgo, and KAGRA.

These ground-based observatories adopt the Michelson interferometer experiment [9] to observe GW signals. Each instrument divides a beam of light into two perpendicular arms of the same length and joins the beams back into one. If no GWs pass by, the beams reunited from both arms cancel each other. However, one arm will be longer than the other with the presence of GWs. Therefore, the combined light beams do not cancel each other, and we observe an output signal. We explain the development and data analysis behind GW interferometers in more detail in section 2.2.

Fig. 1.3 shows pictures of the current detectors. The two LIGO observatories are located in Hanford, Washington and Livingston, Louisiana, USA. Each site consists of an L-shaped interferometer with 4 km long arms. To date, LIGO interferometers are the most sensitive instruments to observe GWs. GEO600 is a 600m interferometer located in Hannover, Germany. Although it has a shorter arm length than other interferometers, it uses advanced technology. It became the key site for the development of GW detector technology. Technologies tested and developed in GEO600 are used in other large-scale detectors. Virgo is located near Pisa, Italy and started to join the observation in 2017. Additionally, KAGRA is a 3 km underground interferometer in Japan that recently joined the observation in 2020.

[2]also known as terrestrial interferometers in some literature.

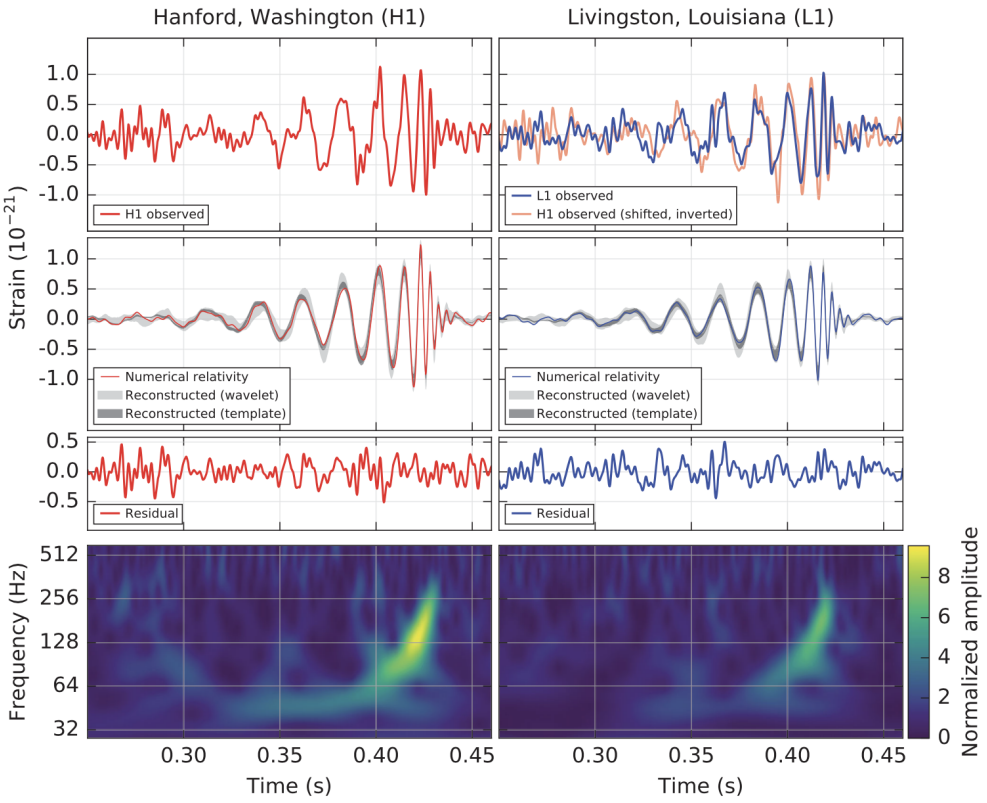

Figure 1.2: Top panels: GW signal in LIGO Hanford and Livingston on 14 September 2015, at 09:50:45 UTC. Bottom panel: the strain signal from a coalescing black-hole binary in time-frequency plot, showing the increase of frequency over time [8]).

The first direct detection of GWs involved many scientists and students who have been working for many years on understanding and detecting signals from an interferometer. In 2017, this research yielded a Noble Prize in Physics. We highlight that the first GW detection is fundamental due to the following reasons:

1. it directly proves the existence of GWs and tests of GR,
2. it directly proves the existence of BHs,
3. it proves the existence of stellar-mass BBHs,
4. it opens an opportunity to observe violent events in the universe such as compact binary coalescences, and
5. it opens an opportunity to study unknown objects in the universe through GWs.

Figure 1.3: LIGO Hanford (top left), LIGO Livingston (topright), GEO600 (bottom left), and Virgo (bottom right).

As the detectors are being developed with better sensitivity, we expect to observe more GW events. During the first three observing runs (2015-2020), we have detected more than 50 signals (see Appendix. B and reference [10]). Each signal is filtered with many waveform templates coming from theoretical models. These models have been developed in the community with various parameters such as mass components, angular momentum, and even eccentricities. The shape and duration of the signal are affected by these parameters, as shown in the python interactive visualization `GWaviz` [11].

We estimate the source parameters for each signal, where the analysis may take days or even months. One bottleneck is the slow waveform generation. Hence, having a fast and reliable waveforms is critical for the analysis. Some waveform models are computationally expensive but have better accuracy. Some others are computationally efficient but less accurate, especially when the binary moves fast towards each other (see section 2.3). We highlight this issue and address our approaches to build a fast and reliable model in our studies through publications I, II, and III. A summary of our strategies is presented in section 3. Finally, we conclude our studies and discuss prospects for future research in section 4.

2
Theoretical background

"Extraordinary claims require extraordinary evidence."

Carl Sagan

2.1 Gravitational waves

The Universe was assumed to have a three-dimensional geometry independent of time until the 20$^{\text{th}}$ century when Albert Einstein proposed the idea that space and time are related through his theory, GR [1]. GR relies on differential geometry, a mathematical coordinate-independent modern framework for geometries. The derivation presented in this section summarizes the details in Refs. [12, 13, 14, 15].

A key concept in GR that describes the spacetime's local geometry is called the *metric tensor* [12], often expressed as the line element in a four-dimensional manifold[1]

$$ds^2 = g_{\mu\nu}\, dx^\mu\, dx^\nu. \tag{2.1}$$

Following Ref. [12], we can sum over all the indices and write in the Cartesian coordinates (t, x, y, z). For flat space or *Minkowski* with convention $\eta_{\mu\nu}$=(-1,1,1,1),

[1] A manifold is a set of points that locally looks like $\mathbb{R}^n$, where n is the dimensionality of the manifold.

it satisfies

$$\begin{aligned} ds^2 =& - dt^2 + dx^2 + dy^2 + dz^2 \\ =& \eta_{\mu\nu}\, dx^\mu\, dx^\nu. \end{aligned} \tag{2.2}$$

Note that we use the geometric units where $c = G = 1$ throughout this dissertation.

The main concept of GR describes the interaction between the distribution of matter and spacetime. This theory is mathematically expressed in the Einstein's field equations

$$G_{\mu\nu} = R_{\mu\nu} - \frac{1}{2} g_{\mu\nu} R = 8\pi T_{\mu\nu}, \tag{2.3}$$

where the *Ricci tensor*, $R_{\mu\nu}$ is a geometric object defined by a choice of *Riemannian* manifold that will be discussed later in this section. R is the contraction of the Ricci tensor, known as the *Ricci scalar*, and $T_{\mu\nu}$ is the stress-energy tensor that describes the distribution of energy and momentum.

Let us assume that the spacetime is almost flat. There exists a coordinate system with a small perturbation $h_{\mu\nu}$ such that

$$g_{\mu\nu} = \eta_{\mu\nu} + h_{\mu\nu}, \qquad \|h_{\mu\nu}\| \ll 1. \tag{2.4}$$

We will only keep terms up to linear order in the small perturbation $h_{\mu\nu}$.

We follow the discussion in Ref. [12, 16], where the movement of vectors in a manifold is expressed through the *Christoffel symbol*

$$\Gamma^\delta_{\alpha\beta} = \frac{1}{2} h^{\delta\sigma} (\partial_\beta h_{\alpha\sigma} + \partial_\alpha h_{\beta\sigma} - \partial_\sigma h_{\alpha\beta}), \tag{2.5}$$

and the curvature of spacetime is described by the *Riemann tensor* via

$$R^\beta{}_{\mu\alpha\nu} = \partial_\alpha \Gamma^\beta_{\mu\nu} - \partial_\nu \Gamma^\beta_{\mu\alpha} + \Gamma^\beta_{\alpha\sigma} \Gamma^\sigma_{\mu\nu} - \Gamma^\beta_{\nu\sigma} \Gamma^\sigma_{\mu\alpha}. \tag{2.6}$$

We should note that the perturbation theory around Minkowski spacetime is known as the *linearized gravity*. Indices can be raised and lowered with $g^{\mu\nu}$, i.e., $h_\alpha{}^\mu = g^{\mu\nu} h_{\alpha\nu}$. Let us express Eq. (2.6) with the definition of Christoffel symbol in Eq. (2.5)

$$g_{\sigma\beta} R^\beta{}_{\mu\alpha\nu} = R_{\sigma\mu\alpha\nu} \tag{2.7}$$

$$= \frac{1}{2} (\partial_\alpha \partial_\mu h_{\sigma\nu} - \partial_\alpha \partial_\sigma h_{\mu\nu} - \partial_\nu \partial_\mu h_{\sigma\alpha} + \partial_\nu \partial_\sigma h_{\mu\alpha}). \tag{2.8}$$

We can obtain the Ricci tensor by contracting the Riemann tensor

$$\begin{aligned} R_{\mu\nu} =& R^\alpha{}_{\mu\alpha\nu} \\ =& \frac{1}{2} (-\Box h_{\mu\nu} + \partial_\mu \partial^\alpha h_{\alpha\nu} + \partial_\nu \partial^\alpha h_{\alpha\mu} - \partial_\mu \partial_\nu h), \end{aligned} \tag{2.9}$$

and the Ricci scalar

$$R = R^{\sigma}{}_{\sigma} = \partial^{\sigma}\partial^{\alpha}h_{\sigma\alpha} - \Box h, \tag{2.10}$$

where we have introduced $h = h^{\alpha}{}_{\alpha}$ and d'Alembertian operator,

$$\Box = \partial^{\alpha}\partial_{\alpha} = -\frac{\partial^2}{\partial t^2} + \frac{\partial^2}{\partial x^2} + \frac{\partial^2}{\partial y^2} + \frac{\partial^2}{\partial z^2}. \tag{2.11}$$

We shall note that the stress-energy tensor vanishes in *vacuum*,

$$T = g^{\mu\nu}T_{\mu\nu} = T^{\mu}_{\mu} = 0. \tag{2.12}$$

By calculating the trace of the Einstein's field equations (2.3), one finds $R = -8\pi T$ [12]. Therefore, we obtain

$$R_{\mu\nu} = 0 \qquad \text{(vacuum)}. \tag{2.13}$$

We want to maintain the form of Eq. (2.4) so that it satisfies the properties of a tensor field in Minkowski space. Thus, we can only allow a small *gauge* or coordinate condition that takes the form

$$x'^{\mu} = x^{\mu} + \xi^{\mu}, \tag{2.14}$$

where $\xi^{\mu}(x^{\nu})$ is an arbitrary infinitesimal vector field and $|\partial_{\nu}\xi^{\mu}| \ll 1$. This transformation changes the metric via

$$h'_{\mu\nu} = h_{\mu\nu} - \partial_{\mu}\xi_{\nu} - \partial_{\nu}\xi_{\mu}. \tag{2.15}$$

Rather than working with the metric perturbation $h_{\mu\nu}$, one can use the *trace-reversed* perturbation,

$$\bar{h}_{\mu\nu} = h_{\mu\nu} - \frac{1}{2}\eta_{\mu\nu}h \tag{2.16}$$

and imposing harmonic gauge (also known as Hilbert or de Donder or *Lorenz*[2] gauge),

$$\partial^{\nu}\bar{h}_{\mu\nu} = 0. \tag{2.17}$$

Thus, the Einstein's field equations (2.3) with a small perturbation of the flat Minkowski (2.4) read to first order

$$\Box\bar{h}_{\mu\nu} = \partial^{\delta}\partial_{\delta}\bar{h}_{\mu\nu} = -16\pi T_{\mu\nu}. \tag{2.18}$$

[2]often erroneously written as *Lorentz gauge* in many literature.

We should notice that the $\Box$ operator forms a classic *wave equation* and can be interpreted as follows. We can solve the wave equation with the perturbations of the spacetime metric in the old coordinate system (2.4) to find a coordinate transformation in (2.14). The general complex solutions of (2.18) reads

$$\bar{h}_{\mu\nu} = A_{\mu\nu} e^{ik_\alpha x^\alpha}, \tag{2.19}$$

only if

$$k^\alpha k_\alpha = 0 = -\omega^2 + ||\vec{k}||^2, \tag{2.20}$$

where

$$\omega = 2\pi f = ||\vec{k}|| = \frac{2\pi}{\lambda}, \tag{2.21}$$

where λ is the wavelength. We can satisfy (2.20) and (2.21) only if k^α is a null vector. Consequently, GWs move with the speed of light.

The coordinate transformation we employed is not unique. One can freely choose another coordinate transformation ξ^μ that fulfills the wave equation, $\Box\xi^\mu = 0$ to maintain the Lorenz gauge.

We now focus on globally vacuum spacetime, $T_{\mu\nu} = 0$ everywhere and asymptotically flat ($h_{\mu\nu} \to 0$ at large distance). We can impose without violating the Lorenz gauge, $\bar{h} = 0$. Note that if $\bar{h} = 0$, then $\bar{h}_{\mu\nu} = h_{\mu\nu}$. Within the Lorenz gauge, we can apply a further gauge transformation that will maintain the Lorenz gauge so long as the additional transformation satisfies the wave equation. We use these additional degrees of freedom to set 4 components of $h_{\mu\nu}$ to zero,

$$\begin{aligned} h_{ti} = h_{0i} = 0, \qquad & (i = 1, 2, 3), \\ h^\sigma_\sigma = 0. \qquad & \end{aligned} \tag{2.22}$$

In the *transverse-traceless* (TT) gauge, the *Lorenz gauge* becomes

$$\partial_\sigma h_\mu{}^\sigma = 0 \quad \Rightarrow 0 = \eta^{\sigma\alpha}\partial_\sigma h_{t\alpha} = \partial_t h_{tt} = i\omega A_{tt} e^{ik_\alpha x^\alpha} \tag{2.23}$$

$$\Rightarrow 0 = \eta^{\sigma\alpha}\partial_\sigma h_{i\alpha} = ik^j A_{ij} e^{ik_\alpha x^\alpha}, \tag{2.24}$$

where $A_{tt} = 0$ and $k^j A_{ij}$ satisfy the conditions above. The gauge choices have eliminated 8 out of 10 independent components of the symmetric perturbation $h_{\mu\nu}$. Thus, the wave tensor only left with two independent components called *polarizations*. Let us orient our coordinate system such that the GW propagates along the z axis. The wave vector reads

$$\underline{k} = (\omega, 0, 0, \omega). \tag{2.25}$$

In the tensor form, it reads

$$h_{\mu\nu} = \begin{pmatrix} 0 & 0 & 0 & 0 \\ 0 & h_+ & h_\times & 0 \\ 0 & h_\times & -h_+ & 0 \\ 0 & 0 & 0 & 0 \end{pmatrix} e^{i\omega(z-t)}. \tag{2.26}$$

We can be interpret it as follows. GWs propagating in the z-direction move with the speed of light and have two polarizations, *plus* and *cross*. These two polarizations squeeze and stretch spaces between particles simultaneously and are rotated 45° relatives to each other (see illustrative plot in Fig. 2.1).

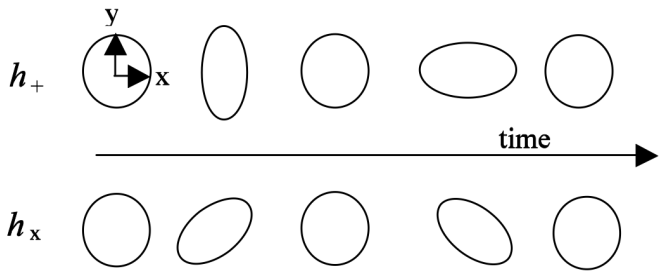

Figure 2.1: Illustrative plot of GW polarizations, + and ×. h_+ is rotated 45° in from $h_\times$ simultaneously on the $x-y$ plane where GWs propagate in the z direction [17].

Revisiting Eq. 2.18, GWs are generated by a matter of source in the linearized Einstein's equation. For a slow motion sources[3] such as compact object coalescences, we want to compute the TT piece of the metric perturbation and obtain the standard quadrupole formula of the gravitational radiation. We follow the derivations in Refs. [12, 13, 18] to obtain the general solution of equation (2.18) in terms of the retarded integral

$$\bar{h}_{\mu\nu}(t, \vec{x}) = 4 \int \frac{T_{\mu\nu}(\vec{x}', t - |\vec{x} - \vec{x}'|)\, d^3x'}{|\vec{x} - \vec{x}'|}, \tag{2.27}$$

where $\vec{x}$ is the position vector of the first BH, and $\vec{x}'$ for the second BH. For a slow-moving source at a distant location, we can approximate $|\vec{x} - \vec{x}'|$ with a constant distance R. The Fourier transform of eq. (2.27) then reads

$$\tilde{h}_{\mu\nu}(\omega, \vec{x}) = \frac{4e^{i\omega R}}{R} \int \tilde{T}_{\mu\nu}(\omega, \vec{x}')\, d^3x'. \tag{2.28}$$

[3] the internal motions are far slower than the speed of light.

The energy-momentum tensor satisfies the conservation law, $\partial_\mu T^{\mu\nu} = 0$. We can solve by applying integration by part as explained in more detail in [13] and assuming a localized source,

$$\begin{aligned} h_{jk}(t,\vec{x}) &= \frac{2}{R}\frac{\partial^2}{\partial t^2}\int x'^j x'^k T^{00}(t-R,x'^i)\,d^3x \\ &= \frac{2}{R}\frac{\partial^2}{\partial t^2}\int x'^j x'^k \rho(t-R,x'^i)\,d^3x, \end{aligned} \tag{2.29}$$

where ρ is the mass-energy density of the source. Note that we apply the harmonic gauge that implies $-i\omega\tilde{h}^{0\nu} = \partial_j \tilde{h}^{j\nu}$. Thus, the spatial components determine $h_{\mu\nu}$.

Defining the second moment I_{ij} of the mass distribution via

$$I_{ij}(t) = x'^j x'^k \rho(t-R,x'^i), \tag{2.30}$$

and combining Eq 2.27 and 2.29 gives

$$h_{jk}^{TT} = \frac{2}{R}\ddot{\mathcal{I}}_{jk}^{TT}(t-R), \tag{2.31}$$

where r is the relative distance from the binary, and $\mathcal{I}$ is the reduced quadrupole moment tensor,

$$\mathcal{I}^{jk} = I^{jk} - \frac{1}{3}\delta^{jk}\delta_{\ell m} I^{\ell m}, \tag{2.32}$$

with

$$I^{jk} = \int \rho(t,\vec{x}) x^j x^k\, d^3x. \tag{2.33}$$

The radiated power in the form of GW satisfies

$$\frac{dE_{\rm GW}}{dt} = \frac{1}{5} < \dddot{\mathcal{I}}_{jk} \dddot{\mathcal{I}}^{jk} > . \tag{2.34}$$

Let us focus on this dissertation's topic, two black-holes orbiting each other. In a circular orbit, their equation of motion in Keplerian orbit satisfies

$$v^2 = \frac{M}{R}, \qquad \omega_{\rm orb} = \sqrt{\frac{M}{R^3}} = \frac{v}{R}, \tag{2.35}$$

where $R \ll r$ is the binary separation. Let us assume a coordinate system originated at the center-of-mass and the two black-holes are located in the $x-y$ plane. The position is given by:

$$x_1 = \frac{\mu R}{m_1}(\cos(\omega_{\rm orb}t)\hat{\mathbf{i}} + \sin(\omega_{\rm orb}t)\hat{\mathbf{j}}), \qquad x_2 = -\frac{m_1}{m_2}x_1, \tag{2.36}$$

where μ is the reduced mass, $\mu = m_1 m_2/M$. We employ these relations to eq. (2.29) and solve the integral, so that

$$h_{jk} = \frac{4\mu R^2 \omega_{\rm orb}^2}{r} \begin{pmatrix} -\cos[2\omega_{\rm orb}(t-r)] & -\sin[2\omega_{\rm orb}(t-r)] & 0 \\ -\sin[2\omega_{\rm orb}(t-r)] & \cos[2\omega_{\rm orb}(t-r)] & 0 \\ 0 & 0 & 0 \end{pmatrix}. \tag{2.37}$$

The amplitude factor is $4\mu v^2/r$. In terms of familiar scales, the typical strain of GW is

$$\begin{aligned} h &\approx \frac{4\mu R^2 \omega_{\rm orb}^2}{r}, \\ &\approx 10^{-21} \frac{1\text{Mpc}}{r} \frac{\mu}{1\text{M}_\odot} \left(\frac{\omega_{\rm orb}}{1\text{Hz}}\right)^2. \end{aligned} \tag{2.38}$$

Eq. (2.38) shows that the GW strain produced from a coalescing BBH is tiny. Hence, direct detection of GW is challenging.

2.2 Detecting gravitational waves

The detection of GWs involves collaborative work between experimental and theoretical physics. We divide this section into the basic principle and the development of GW detectors 2.2.1 and data analysis of the signals 2.2.2.

2.2.1 Detectors

The direct detection of GW signals is known as an ambitious project spanning over decades. It is due to the need to a build high sensitivity detector to measure small distortion in spacetime. Experimental studies to detect GWs start to attract physicist more than 40 years after GWs were predicted by Einstein.

In the late 1950s, Joseph Weber suggested an apparatus designed to detect GWs called the *Weber bars* [19, 20]. He predicted that GW signals arrive at frequencies around 1660 Hz and built a massive aluminum cylinders with resonant frequency following his theoretical prediction. It is expected that a GW signal would change the amplitude or phase of the bar's oscillation. The cylinder was expected to change its length around 10^{-16} meters and rang when a GW signal passed by. Later, he claimed the Weber bar detected GWs from the center of the Galaxy. Through careful investigation, it was proven that there was miscalculation and that he did not detected GWs [17].

In 1967, Rainer Weiss of MIT published an analysis of an interferometer used to detect GWs. Kip Thorne of Caltech followed up his work in 1968 by developing theoretical calculation for GW signals. In 1980, the National Science

Foundation (NSF) funded the study of the large laser interferometer. This experiment's concept is motivated by the Michelson interferometer in 1880 with longer arms and increased sensitivity. Over the years, this project involved thousands of scientists and students. Finally, in 2015, the two LIGO interferometers detected the first GW signal from a BBH collision. Because of this work, Rainer Weiss, Kip Thorne, and Barry Barish were awarded the Nobel prize in physics in 2017.

LIGO and Virgo interferometers share a similar concept to observe GWs. Each instrument consists of an L-shaped interferometer splitting the laser beam along 4 km arm. Lasers are split and bounced back and forth inside each arm by the mirrors before they hit the detector. If no GW signal is observed, signals from both arms cancel each other. When GWs pass by, one arm is shorter than the other simultaneously. The laser beam that traveled through the shorter arm arrives earlier than the other. Hence, the signal do not meet up nicely when recombined at the detector, and we see fringe pattern as shown in Fig. 2.2. What we measure is the change of length of the X arm relative to the Y arm. These interferometers are sensitive in a 10 Hz to kHz band, where the main sources are compact binary coalescences, such as BBH, BNS, and neutron-star black-hole (NSBH) collisions, continuous waves from spinning NSs, and supernovae.

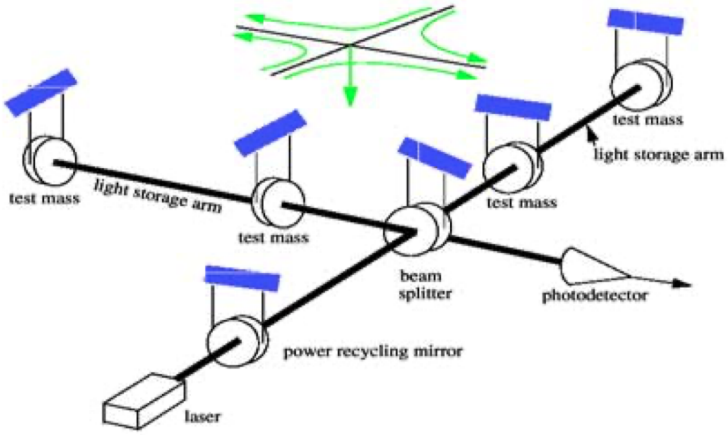

Figure 2.2: Schematic diagram of LIGO interferometer [17]. A laser beam is split by the beamsplitter into two perpendicular arms and bounced many times through each test mass (mirror). The beams are reunited and measured in a photodetector. Without GW, laser beam from each arm cancels each other due to superposition, no signals is detected in the photodetector. When a GW signal passes by, it shrinks one arm and stretches the other. The reunited laser beam does not cancel each other. Hence, we measure a signal in the photodetector.

The sensitivity of these detectors are limited by some noise background. Some conditions and glitches can mimic astrophysical signals and contaminate the mea-

surements. Noises are generated by many physical phenomena on Earth and the sum leads to the familiar sensitivity curves of the instrument. We highlight main noise sources and briefly explain as follows: [21]

i Seismic noise. This noise causes the motion of the mirrors and dominant at low frequencies. The main sources of seismic noise are the ground vibrations, caused by earthquakes, wind, ocean waves, and human activities in the surrounding area.

ii Thermal noise. As the laser ray hits the mirrors, it increases the mirrors' temperature. This condition is known as the suspension thermal noise, caused by the microscopic fluctuations of the individual mirror and its suspensions. One way to reduce this noise is to have increased the beam size such that it averages over the mirror surface. Another source of the thermal noise comes from the coating and known as the Brownian coating noise. It arises from the mechanical dissipation of the coating and is related to the coating material.

iii Quantum noise. This noise is mainly caused by the statistical fluctuations of the photons that arrive in the photo detector.

iv Gravity gradients. This noise is caused by fluctuating gravitational forces on the test masses due to seismic wave perturbations in the earth.

The design sensitivity of the advanced LIGO interferometer is shown in Fig. 2.3. Both LIGO instruments have similar lengths and shapes, situated in Hanford and Livingston, USA. The distance between the two observatories is 3002 km or 10ms travel at the speed of light. When both observatories detect a similar signal within 10 ms, it is more likely that the signal is astrophysical. This time delay is also used to pinpoint the sky position of the source. Furthermore, the x arm of the Livingston observatory is oriented almost aligned with the y arm of the Hanford one. One of the main reasons is to measure the orientation parameter of a GW signal (see Ref. [22] for more detail).

To pinpoint the source's sky location, we employ a triangulation method that is similar to GPS. Hence, more interferometers would give higher precision. These interferometers have or will join the science run. First, Virgo is a 3 km GW interferometer in Italy that joined the second and third science run. Second, GEO600 is a 600-meter interferometer near Hannover, Germany. Many parts of LIGO instruments were built in Hannover. Subsequently, two detectors, KAGRA and LIGO India are currently in the final building stage and will join the observing run shortly. KAGRA is an underground observatory in Japan, and LIGO India is planned to be built in the Hingoli District of Maharashtra state in western India. They are known as the second generation or 2G and 2.5G detectors.

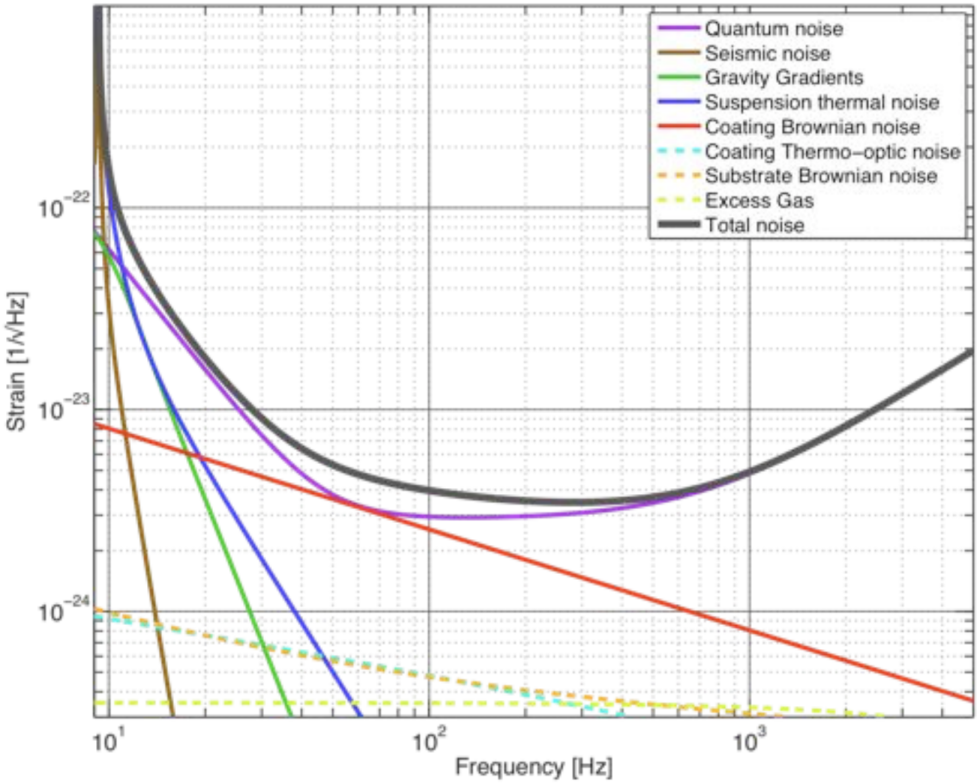

Figure 2.3: aLIGO design sensitivity at different frequencies and noise curves (see more detail in [21]).

Consecutively, higher sensitivity GW detectors are planned to begin observing in the 2030s. These 3G detectors are as follows. First, Einstein telescope [16] is a 10 km GW observatory planned between Belgium, the Netherlands, and Germany or in Sardinia, Italy. Second, Cosmic Explorer [23] is a 40 km L-shaped observatory that is expected to be built in the USA. Third, NEMO [24] is a detector currently planned to be built in Australia focusing on high sensitivity for the study of NS post-merger signals. The coordinates of the GW observatories are shown in Table 2.1. These projects are about to begin or in the early phase. Therefore, they may change their plan such as location, length, or timeline in the future.

2.2.2 Data analysis

The detector's sensitivity is limited by the noise sources. We can express the detector output $s(t)$ as a linear superposition between the noise $n(t)$ and the signal

Observatory	Latitude	Longitude	Orientation	ζ
LIGO Livingston	30.56^0	-90.77^0	243^0	90^0
LIGO Hanford	46.45^0	-119.41^0	171.8^0	90^0
Virgo	43.63^0	10.5^0	116.5^0	90^0
GEO600	52.14^0	9.48^0	94.19^0	90^0
KAGRA	36.25^0	137.18^0	0^0	90^0
LIGO India	19.09^0	74.05^0	0^0	90^0
Einstein Telescope	43.54^0	10.42^0	19.48^0	60^0
Cosmic Explorer	30.54^0	-90.53^0	162.15^0	90^0
Assumed detector in Australia	-31.51^0	115.74^0	0^0	-

Table 2.1: The coordinates of the current and proposed GW observatories. Orientation is the smallest angle made by any of the arms and the local north direction and ζ is the angle between two arms (see Ref. [25]).

$h_0(t;\vec{\lambda})$, where $\vec{\lambda} = \{\lambda_k | k = 1, 2, \ldots, N_s\}$ denotes the N_s parameters,

$$s(t) = n(t) + h_0(t;\vec{\lambda}). \tag{2.39}$$

Assuming the detector noise is stationary Gaussian with zero mean, we find

$$\overline{n(t)} = 0, \tag{2.40}$$

where the overline denotes the average. The one-sided power spectral density $S_n(|f|)$ is then defined by

$$\overline{\tilde{n}(f)\tilde{n}^*(f')} = \frac{1}{2} S_n(|f|)\delta(f - f'), \tag{2.41}$$

where $\tilde{n}$ denotes the Fourier transform, * is the complex conjugation, and $\delta(f - f')$ is the δ-distribution. $S_n(f)$ is the noise spectral density shown with the black line in Fig. 2.3. We use the convention of the Fourier transform as follows

$$\tilde{x} = \int_{-\infty}^{\infty} x(t) e^{2\pi i t f}\, dt. \tag{2.42}$$

The detector sensitivity $S_n(|f|)$ is defined such that $\overline{(n|n)} = 1$. We shall introduce the inner product defined by

$$(s|h) = 4\mathcal{R} \int_0^{\infty} \frac{\tilde{s}(f)\tilde{h}^*(f)}{S_n(f)}\, df. \tag{2.43}$$

The determination whether a signal is present or absent is made by setting a threshold on the *likelihood ratio* with template signal h that reads

$$\Lambda = \frac{P(s|h)}{P(s|0)} = \frac{p(s|h)ds}{p(s|0)ds} = \frac{p(s|h)}{p(s|0)}, \tag{2.44}$$

where $P(s|h)$ is the probability that the signal is present in the detector output data stream and $P(s|0)$ is the null hypothesis (no signal in the data). Instead of using probability, we can express the likelihood ratio with the corresponding probability densities $p(s|h)$ and $p(s|0)$. In the absence of signal $p(s|0)$, it is defined by

$$p(s|0) = p(s) = \mathcal{K} \exp\Big[-\frac{1}{2}(s|s)\Big], \tag{2.45}$$

where $\mathcal{K}$ is a normalization constant.

Consider a condition when a signal present, the probability density is given by

$$p(s|h) = p(s-h) = \mathcal{K}\Big[-\frac{1}{2}(s-h)|(s-h)\Big], \tag{2.46}$$

with $n(t) = s(t) - h(t)$. Thus, the likelihood ratio reads

$$\begin{aligned}
\Lambda =& \frac{p(s|h)}{p(s|0)} = \frac{p(s-h)}{p(s)} \\
=& \frac{\exp\big[-\frac{1}{2}(s-h)|(s-h)\big]}{\exp\big[-\frac{1}{2}(s|s)\big]} \\
=& \exp\Big\{ -\frac{1}{2}\big[(s|s) - 2(s|h) - 2(s|h) - (h|h)\big] + \frac{1}{2}(s|s)\Big\} \\
=& \exp\Big[(s|h) - \frac{1}{2}(h|h)\Big].
\end{aligned} \tag{2.47}$$

In practice, we obtain $(s|h)$ from the detector's data and $(h|h)$ is constant for a particular $S_n(f)$ and h.

According to the *Neyman-Pearson* criterion, the signal is present if it surpasses some statistical threshold Λ (or equivalently $\ln\Lambda$) [26, 14]. This threshold is set according to the tolerated *false alarm probability*. Now, given the norm of the template signal $||h|| = \sqrt{(h|h)}$ and the normalized waveform $\hat{h} = h/||h||$, we can maximize Eq. (2.47) if the $||h|| = (h_0|\hat{h})$ so that

$$\max_{||h||} \ln\Lambda = \frac{1}{2}\Big[\frac{(h_0|h)}{||h||}\Big]^2 = \frac{1}{2}\Big[||h_0||(\hat{h}_0|\hat{h})\Big]^2. \tag{2.48}$$

The signal is present if the likelihood value is large enough over $h(\vec{\lambda})$ in the template bank. This can be obtained with large signal-to-noise ratio (SNR) $\rho = ||h_0||$ or high overlap or match between the signal and the template waveform,

$$O[(h_0|h(\vec{\lambda}))] = \frac{(h_0|h(\vec{\lambda})}{||h_0||||h(\vec{\lambda})||}, \qquad (-1 \leq O \leq 1). \tag{2.49}$$

Since the shape and length of the waveforms depend on various parameters, the signal is filtered over numerous templates. During the first LIGO observing run, more than 250,000 waveforms varying in masses and spins were employed and even more in the more recent observing runs. This method is called *matched filtering*.

2.3 Modeling gravitational wave sources

Thanks to advanced developments in detector technology and data analysis, LIGO and Virgo detected 48 BBH and 2 BNS events during the first three observing runs, O1–O3a (see Table. B.1 [27] and Table. B.2 [28] of Appendix. B). Additionally, 2 NSBH collisions have been observed for the first time in January 2020 [10].

The detected signals vary in parameters, namely intrinsic and extrinsic parameters. These parameters govern the shape and length of waveform. While the intrinsic parameters describe the binary's astrophysical constraints, extrinsic parameters depend on the binary position relative to the observer. Intrinsic parameters are mass ratio (q), the dimensionless angular velocity known as spins ($\vec{\chi}_1, \vec{\chi}_2$), and eccentricity ($e$). BH size and its total mass have linear relations. Thus, we can also scale the waveform's amplitude with the total mass M. The extrinsic parameters are the time of coalescence (t_c), the angle between the binary and the observer (ι), azimuthal phase (ϕ_c), sky location (θ, ϕ), polarization angle (ψ), and the luminosity distance (D_L). Given two GW polarizations, + and ×, that corresponds to antenna pattern F_+ and $F_\times$, the arm length difference when GW pass by is expressed by the following relation [29]:

$$\frac{\delta L}{L} = h = h_+(t)F_+(\theta, \phi, \psi) + h_\times(t)F_\times(\theta, \phi, \psi). \tag{2.50}$$

The above equation is in the time domain. For the purpose of source analysis, it is easier and faster to compute in the frequency domain. However, applying Fourier transform for each source with different parameters is computationally expensive. The most common approach is using the stationary-phase approximation (SPA), an approach for the signal expression in the Fourier domain. Following ref [29], the interferometer response in the SPA is expressed by

$$h(f; \mathcal{A}, \mathcal{M}, \psi) \equiv \mathcal{A}\mathcal{M}(\pi f \mathcal{M})^{2/3} \cos(\Phi + \psi), \tag{2.51}$$

with

$$f \equiv \frac{1}{\mathcal{M}}\Big[\frac{5}{256}\frac{\mathcal{M}}{\mathrm{t}_c - t}\Big]^{3/8}, \tag{2.52}$$

where $\mathcal{A}$ is an amplitude function, Φ is a phase function, and ψ is a constant. $\mathcal{M}$ is known as chirp mass and expresses by the following relation

$$\mathcal{M} = \frac{(m_1 m_2)^{3/5}}{M^{1/5}}. \tag{2.53}$$

The shape of the waveform changes with the inclusion of the intrinsic parameters such as the mass components, spin, eccentricity or tidal deformability (λ) for BNS coalescences. Fig. 2.4 shows how different mass ratios and spin parameters change the waveform shape. See the interactive visualization [11] for waveforms with different parameters.

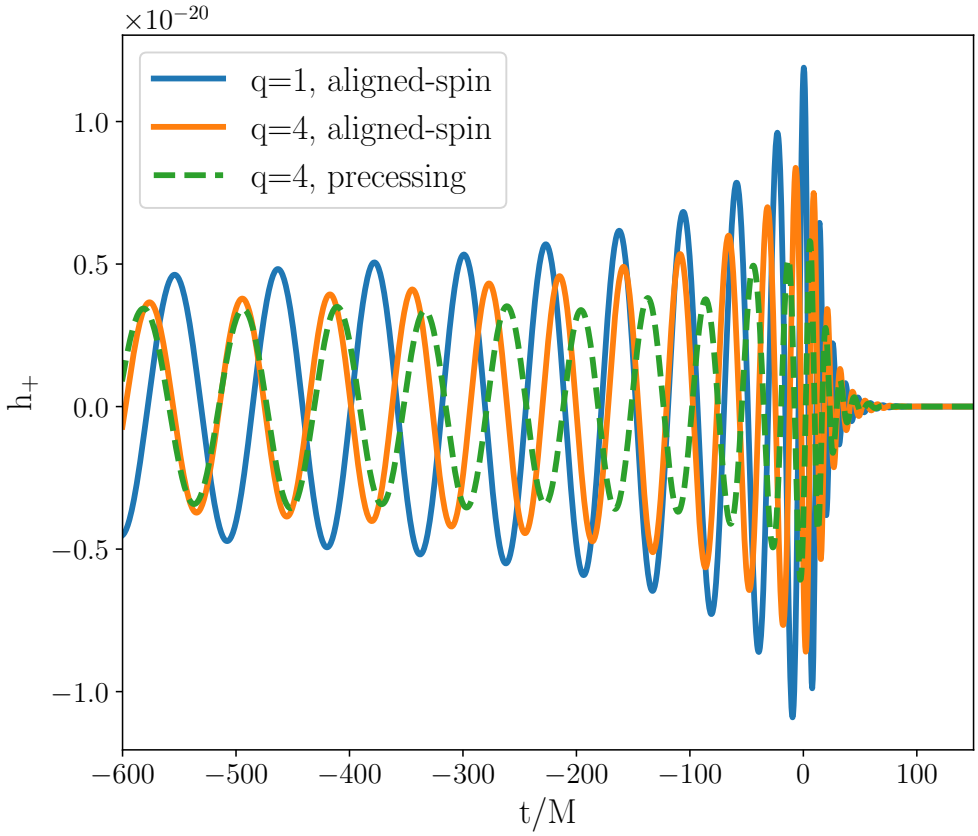

Figure 2.4: Different mass ratios ($q=m_1/m_2$) and spin parameters affect the waveform shape. The blue and orange lines are the aligned-spin model ($\chi_{1x,y} = \chi_{2x,y} = 0$), the green line is the precessing model ($\chi_{1x,y} = \chi_{2x,y} \neq 0$). We use `SEOBNRv4` *waveform model to generate this plot.*

2.3.1 Post-Newtonian approximation

It is not our intention to review all of the post-Newtonian (PN) theory but to provide the necessary background information for the techniques used in this dissertation. A more detailed overview of PN formalism can be found in [30, 31] and references therein.

Let us start with Eq. (2.38). The signal satisfies:

$$h(t) = \frac{4M\eta v^2}{r} e^{-i(2\omega_t + \phi_0)}, \tag{2.54}$$

where v is the linear velocity. The orbital frequency $\omega_{\rm orbit}$ relies on the orbital phase Φ with the following relation:

$$\omega_{\rm orbit} = \frac{d\Phi_{\rm orbit}}{dt} \equiv \dot{\Phi}, \tag{2.55}$$

and the Newtonian energy of a circular binary is given by

$$E = -\frac{M\eta}{2} v^2. \tag{2.56}$$

Eq. (2.56) shows that the binary loses its energy as it moves faster. Under the assumption that the binary orbit shrinks merely due to GW emission, we can write the flux of energy radiated away in the form of GW radiation at a large distance from the source:

$$\frac{dE(v)}{dt} = -\mathcal{F}, \tag{2.57}$$

or equivalently:

$$\dot{v} = -\frac{\mathcal{F}(v)}{dE(v)/dv}, \tag{2.58}$$

with

$$\mathcal{F} = \frac{1}{5} \overline{\frac{d^3 Q^{jk}}{dt^3} \frac{d^3 Q_{jk}}{dt^3}}, \tag{2.59}$$

and

$$Q_{jk} = \int \rho(t, x^i) \left(x_j x_k - \frac{1}{3} \delta_{jk} x^l x_l \right) d^3 x. \tag{2.60}$$

Here $\mathcal{F}$ is the energy radiated over time, also known as the luminosity, ρ is mass distribution, and δ_{jk} is the standard Kronecker delta symbol. If we assume a condition where the fractional change in the orbital frequency for one cycle is insignificant, known as the *adiabatic inspiral*, we find:

$$\dot{\Phi}(t) = \frac{v^3}{M}. \tag{2.61}$$

We shall call the commonly used notations of the parameters as follows:

$$q = m_1/m_2 \geq 1, \tag{2.62}$$
$$M = m_1 + m_2, \tag{2.63}$$
$$\eta = \frac{m_1 m_2}{M^2}, \tag{2.64}$$
$$\delta = \frac{m_1 - m_2}{M}, \tag{2.65}$$
$$v = M\omega^{1/3}, \tag{2.66}$$
$$\chi_i = \frac{\vec{S}_i \cdot \vec{L}}{||\vec{L}||m_i^2}, \tag{2.67}$$
$$\chi_a = \frac{\chi_1 - \chi_2}{2}, \tag{2.68}$$
$$\chi_s = \frac{\chi - 1 + \chi_2}{2}, \tag{2.69}$$
$$\chi_{\text{eff}} = \frac{\chi_{1z} m_1 + \chi_{2z} m_2}{M}, \tag{2.70}$$

where $\vec{L}$ is the binary's orbital angular velocity in the (x, y, z) coordinates.

PN approximation expands the relationship between the energy E and the flux $\mathcal{F}$ to a higher power of v/c. The order can be explicitly seen through the power of v. The generic expression of waveform polarizations, $h_{+,\times}$ is described by:

$$h_{+,\times}(n) = \frac{2M\eta}{D_L} v^2 \sum_{n=0}^{\infty} v^n H_{+,\times}^{(n/2)}, \tag{2.71}$$

where n denotes the PN orders and $H_{+,\times}$ needs to be calculated (see the generic expression in [32] and [33]).

We start with a quasicircular BBH system with spins aligned to the orbital angular momentum $\vec{L}$ (see Fig. 2.5). Although precessing systems with six individual spin components may capture more physical phenomena, we focus on the aligned binaries because these systems can cover a large fraction of BBH coalescences. Besides, we can systematically map align spin binaries into precessing ones through analytical computation (see Ref. [34, 35, 36] and references therein).

Moreover, we can translate the relation between the two polarizations and the binary parameters, amplitude A, phase $\phi_{\rm orbit}$ in the time domain as follows:

$$\begin{aligned} h(t) =& h_+(t) - ih_\times(t), \\ =& A(t)\exp\left(i\Phi_{\rm orbit}(t)\right), \end{aligned} \tag{2.72}$$

where amplitude A is given by Eq. (2.54). Now, we only need to obtain the analytical expression of the phase $\Phi_{\rm orbit}$ through the derivation of energy and flux.

Following the derivation in [30], the explicit expression of energy reads:

$$\begin{aligned} E(v) = -\frac{M\eta v^2}{2}\Big\{1 &- v^2\Big(\frac{3}{4}+\frac{\eta}{12}\Big) + v^3\Big[\frac{8\delta\chi_a}{3} + \Big(\frac{8}{3}-\frac{4\eta}{3}\Big)\chi_s\Big] \\ &+ v^4\Big[\frac{19\eta}{8} - 2\delta\chi_a\chi_s - \frac{\eta^2}{24} + (4\eta-1)\chi_a^2 - \chi_s^2 - \frac{27}{8}\Big] \\ &+ v^5\Big[\chi_a\Big(8\delta - \frac{31\delta\eta}{9}\Big) + \Big(\frac{2\eta^2}{9} - \frac{121\eta}{9} + 8\Big)\chi_s\Big] \\ &- v^6\Big[\frac{35\eta^3}{5184} + \frac{155\eta^2}{96} - \Big(\frac{34445}{576} - \frac{205\pi^2}{96}\Big)\eta + \frac{675}{64}\Big], \Big\} \end{aligned} \tag{2.73}$$

and the flux is given by:

$$\begin{aligned} \mathcal{F} = \frac{32}{5}\eta^2 v^{10}\Big\{1 &- v^2\Big(\frac{1247}{336}+\frac{35}{12}\eta\Big) \\ &+ v^3\Big[4\pi - \frac{11\delta\chi_a}{4} + \Big(3\eta - \frac{11}{4}\Big)\chi_s\Big] \\ &+ v^4\Big[\frac{33\delta\chi_a\chi_s}{8} + \frac{65\eta^2}{18} + \Big(\frac{33}{16} - 8\eta\Big)\chi_a^2 + \Big(\frac{33}{16} - \frac{\eta}{4}\Big)\chi_s^2 + \frac{9271\eta}{504} - \frac{44711}{9072}\Big] \\ &+ v^5\Big[\Big(\frac{701\delta\eta}{36} - \frac{59\delta}{16}\Big)\chi_a + \Big(\frac{227\eta}{9} - \frac{157\eta^2}{9} - \frac{59}{16}\Big)\chi_s - \frac{583\pi\eta}{24} - \frac{8191\pi}{672} \\ &- \frac{1-3\eta}{4}\chi_s(1+3\chi_s^2+9\chi_a^2) - \frac{1-\eta}{4}\delta\chi_a(1+3\chi_a^2+9\chi_s^2)\Big] \\ &+ v^6\Big[-\frac{1712}{105}\ln(4v) - \frac{1712\gamma_E}{105} - \frac{775\eta^3}{324} - \frac{94403\eta^2}{3024} \\ &+ \Big(\frac{41\pi^2}{48} - \frac{134543}{7776}\Big)\eta + \frac{16\pi^2}{3} + \frac{6643739519}{69854400}\Big] \\ &+ v^7\pi\Big[\frac{193385\eta^2}{3024} + \frac{214745\eta}{1728} - \frac{16285}{504} + O\Big(\frac{1}{c^8}\Big)\Big]\Big\}, \end{aligned} \tag{2.74}$$

where the Euler constant $\gamma_E \approx 0.5772$.

One way to solve this is to obtain the expression of $t(v)$. One can compute the inverse of Eq. (2.58) in v and analytically integrate as explained in [14]. After

obtaining $t(v)$, we can compute the analytical expression $\Phi_{\rm orbit}$ up to 3.5 PN order by integrating Eq. (2.61) so that:

$$
\begin{aligned}
\Phi_{\rm orbit}(v) = \Phi_0^{\rm orbit} - \frac{1}{32\eta v^5}\Big\{ & 1 + v^2\Big[\frac{3715}{1008} + \frac{55\eta}{12}\Big] + v^3\Big[-10\pi + \frac{565\delta\chi_a}{24} + \Big(\frac{565}{24} - \frac{95\eta}{6}\Big)\chi_s\Big] \\
& + v^4\Big[\frac{15293365}{1016064} + \frac{27145\eta}{1008} + \frac{3085\eta^2}{144} - \frac{405}{8}\delta\chi_a\chi_s - \Big(\frac{405}{16} - \frac{5\eta}{4}\Big)\chi_s^2 - \Big(\frac{405}{16} - 100\eta\Big)\chi_a^2\Big] \\
& + v^5 \ln v\Big[\frac{38645\pi}{672} - \frac{65\pi\eta}{8} - \Big(\frac{735505}{2016} - \frac{12265\eta}{36} - \frac{85\eta^2}{2}\Big)\chi_s \\
& - \Big(\frac{735505}{2016} + \frac{65\eta}{4}\Big)\delta\chi_a - \Big(\frac{45}{4} - \frac{45\eta}{4}\Big)\delta\chi_s^2\chi_a - \Big(\frac{45}{4} - \frac{135\eta}{4}\Big)\chi_s\chi_a^2 - \Big(\frac{15}{4} - \frac{45\eta}{4}\Big)\chi_s^3 - \Big(\frac{15}{4} - \frac{15\eta}{4}\Big)\delta\chi_a^3\Big] \\
& + v^6\Big[\frac{12348611926451}{18776862720} - \frac{1712\gamma_E}{21} - \frac{160\pi^2}{3} - \Big(\frac{15737765635}{12192768} - \frac{2255\pi^2}{48}\Big)\eta + \frac{76055\eta^2}{6912} \\
& - \frac{127825\eta^3}{5184} - \frac{1712\ln(4v)}{21} + \Big(\frac{730\pi}{3} - \frac{560\pi\eta}{3}\Big)\chi_s - \Big(\frac{34225}{2688} - \frac{217135\eta}{672} + \frac{1255\eta^2}{12}\Big)\chi_s^2 \\
& + \frac{730\pi\delta\chi_a}{3} - \Big(\frac{34225}{2688} - \frac{7705\eta}{48} + \frac{1205\eta^2}{3}\Big)\chi_a^2 - \Big(\frac{34225}{1344} - \frac{10385\eta}{24}\Big)\delta\chi_s\chi_a\Big] \\
& + v^7\Big[\frac{77096675\pi}{2032128} + \frac{378515\pi\eta}{12096} - \frac{74045\pi\eta^2}{6048} - \Big(\frac{20373952415}{24385536} + \frac{150935\eta}{1792} - \frac{578695\eta^2}{3456}\Big)\delta\chi_a \\
& - \Big(\frac{20373952415}{24385536} - \frac{4348560355\eta}{6096384} - \frac{11189515\eta^2}{24192} + \frac{71705\eta^3}{864}\Big)\chi_s - \Big(\frac{285\pi}{4} - 5\pi\eta\Big)\chi_s^2 \\
& - \Big(\frac{285\pi}{4} - 280\pi\eta\Big)\chi_a^2 - \frac{285\pi}{2}\delta\chi_s\chi_a + \Big(\frac{16185}{224} - \frac{74645\eta}{1344} + \frac{905\eta^2}{24}\Big)\chi_s^3 \\
& + \Big(\frac{16185}{224} - \frac{437275\eta}{1344} + \frac{85\eta^2}{8}\Big)\delta\chi_a^3 + \Big(\frac{48555}{224} - \frac{198125\eta}{1344} + \frac{255\eta^2}{8}\Big)\delta\chi_s^2\chi_a \\
& + \Big(\frac{48555}{224} - \frac{1337635\eta}{1344} + \frac{8935\eta^2}{24}\Big)\chi_s\chi_a^2\Big]\Big\}.
\end{aligned}
\tag{2.75}
$$

The contribution of higher PN orders becomes more significant in the late inspiral. Of course, it is also more difficult to derive higher PN terms. So far, the latest version available is the expression up to 4 PN orders. Eccentric PN expressions are given in [37]. We can fuse the eccentric PN model with our eccentric late inspiral model to build eccentric waveforms with longer inspiral (see Ref. [37, 38] and section 3).

Collecting the above equations, one can generate waveforms in an individual machine within seconds, making PN a promising method to model GW sources. However, recent studies show that PN approximation diverges in some orders and suffers from boundary conditions at infinity. The solution is to employ numerical approach or perturbation theory depending on mass ratio and distance (see Fig. 2.6).

2.3.2 Numerical relativity

The validity of PN approximation is restricted to weak gravity and small relative velocities. Thus, the PN expansion breaks down when the binary moves faster towards merger. Another way to solve the Einstein's equations is by integrating

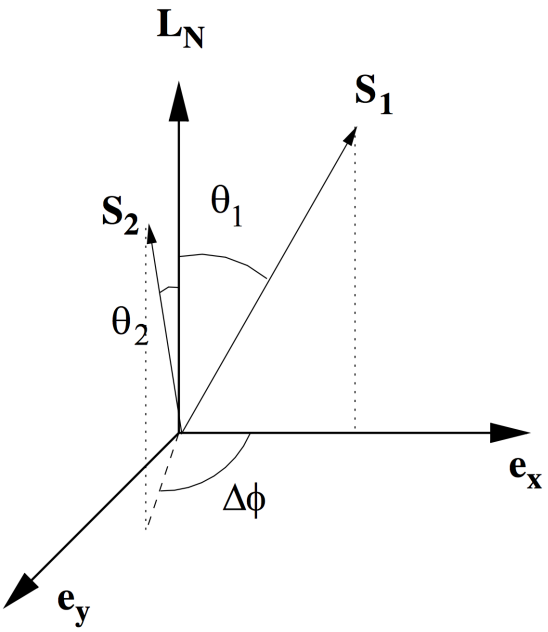

Figure 2.5: Schematic diagram of the align spin BBH systems used in this study (see Ref. [39]). $\vec{S}_1$ and $\vec{S}_2$ are the individual spin of each BH in the Cartesian coordinates e_x, e_y, e_z, where the orbital angular momentum $\vec{L}$ aligns to the total angular momentum $\vec{J} = \vec{L} + \vec{S}_1 + \vec{S}_2$ and the z-axis. (θ_1 and θ_2) are the angles between $\vec{L}$ and ($\vec{S}_1$, $\vec{S}_2$) respectively. $\delta\phi$ is the difference between the projection angle θ_1 and θ_2 along the $x-y$ coordinates.

it numerically. It is not our intention to discuss the development of numerical relativity (NR) extensively in this dissertation. A more detailed overview can be found in [41, 42, 43, 44, 45].

The fundamental principle in NR is that the dynamic evolution of BBH according to the four-dimensional Einstein's equations are reformulated as an initial value problem and the four-dimensional spacetime manifold is split into three-dimensional spatial hypersurfaces that evolve over time. Fig. 2.7 shows a schematic plot of the concept.

The energy-momentum tensor in the Einstein's equations is expressed in the "3+1" form with the following projection,

$$S_{\mu\nu} = P^{\sigma}_{\mu} P^{\rho}_{\nu} T_{\sigma\rho}, \tag{2.76}$$

$$S_{\mu} = -P^{\sigma}_{\mu} n^{\rho} T_{\sigma\rho}, \tag{2.77}$$

$$E = n^{\mu} n^{\nu} T_{\mu\nu}, \tag{2.78}$$

where $S_{\mu\nu}$ is the spatial part of the energy-momentum tensor $T_{\mu\nu}$, P^{μ}_{ν} is the spatial

[t]

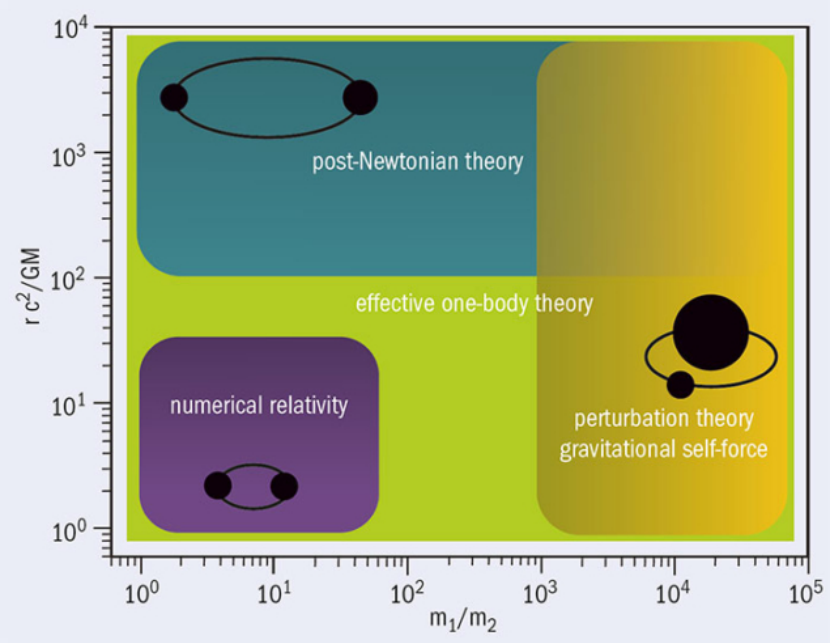

Figure 2.6: Systematic diagram of validity range for different approximations in logarithmic scale [40]. The x-axis is the mass ratio and the y-axis is the distance between two BHs r scaled with total mass M. PN expansion is promising when the separation is relatively large, in the inspiral range. PN breaks down when BBH moves faster towards merger, the peak amplitude in the waveform. The two are connected in the intermediate range, where we will discuss further in the following subsections. We shall use perturbation theory for high mass ratio. We will not discuss this approach because their GW frequency is too low for the ground-based-interferometry. The progenitors are IMRI and EMRI, the main GW sources for the space-based-detector of LISA.

projection operator of the normal vector into the spatial slice. S_μ is the momentum density, and E is the energy density measured by a normal observer with four-velocity n^ν.

Following the derivation in [45], we can obtain two constraint equations that need to be fulfilled for all time slices and two evolution equations. These four equations are the backbone of modern NR simulations, known as the Arnowitt-Deser-Misner (ADM) formulation [46].

Unfortunately, the ADM equations combined with the common slicing conditions are only weakly hyperbolic [47]. Choosing the proper condition in the particular foliation of spacetime is crucial to ensure a successful simulation. Due to these issues, the ADM equations are not numerically stable and cannot fulfill the requirements for long-time numerical simulations.

In 1987, Nakamura, Oohara, and Kojima recast the ADM equations that led

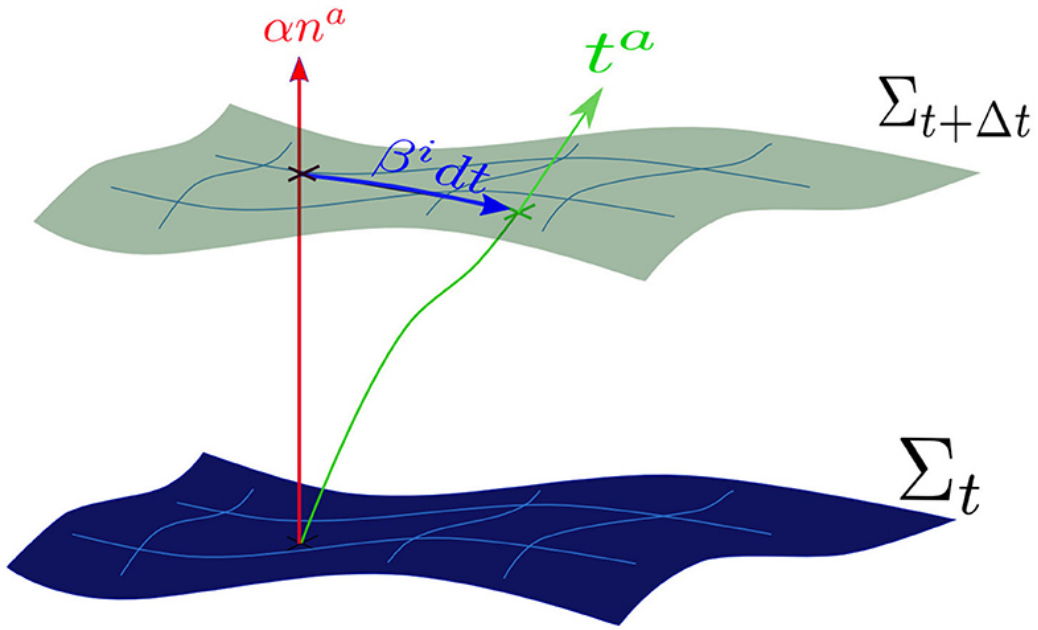

Figure 2.7: Schematic foliation of the spacetime manifold with three-dimensional hypersurfaces Σ [45]. The four-vector t^a shows the direction of evolution with the time coordinate t. The lapse function α measures the proper time from hypersurface Σ_t to $\Sigma_{t+\Delta t}$ along the normal vector n^a. The shift vector β^i measures the displacement between the observer time line t^a and the normal vector n^a.

to a more stable evolution code. This work is followed up by Shibata, Nakamura [48] in 1995, and Baumgarte, Shapiro [49] in 1998, where they successfully improved the formulation yielding a more well-posed, numerically stable evolution scheme. Following Ref. [50], the three-dimensional hypersurface slice is characterized by an induced metric γ_{ij}. Assuming conformal flatness ($\gamma_{ij} = \psi^4\eta_{ij}$) and extrinsic curvature ($K^i_i = 0$). The constraint equation is solved by rescaling the same quantities with a conformal factor ψ to avoid BH singularities,

$$\psi = 1 + \sum_{i=1}^{2} \frac{m_i}{|r - r_i|} + u, \tag{2.79}$$

where m_i and r_i denote the i^{th} BH mass and location respectively, and u is a regular function. This reformulation is known as the Baumgarte-Shapiro-Shibata-Nakamura-Oohara-Kojima (BSSNOK), often called as the Baumgarte-Shapiro-Shibata-Nakamura (BSSN) formulation. The BSSN formulation gains more popularity in the community because it provides a more stable numerical evolution than ADM, especially when applied to practical problems such as merging two BHs.

Initially, each BH slice is represented by a wormhole geometry with the compact structure leading to a single point, called the puncture. There is an issue with the initial data, especially for sufficiently large nonspinning BBH separation. One would expect that the spacetime surrounding each BH would be closed to Schwarzschild or Kerr solution, but this is not the case due to the conformal flatness assumption and the Bowen-York extrinsic curvature. The Cauchy surface[4] of a Kerr solution is not conformally flat. Thus, the Bowen-York initial data contains the *junk radiation*. It leaves the system once the simulation starts to evolve, leaving the wormhole geometry [51] to become a trumpet topology [52] as shown in Fig. 2.8. In NR simulations, the junk radiation manifests as a burst. After the junk radiation have taken place, the punctures move in a grid following the physical motion of the BH. Thus, the approach is widely known as the *moving puncture* gauge.

An alternative method to moving puncture is the generalized gauge decomposition [53]. The essence of this method lies in the ”excision” technique, where one can discard a small fraction inside the event horizon from the computational domain instead of dealing with the choice of gauge to avoid BH singularity.

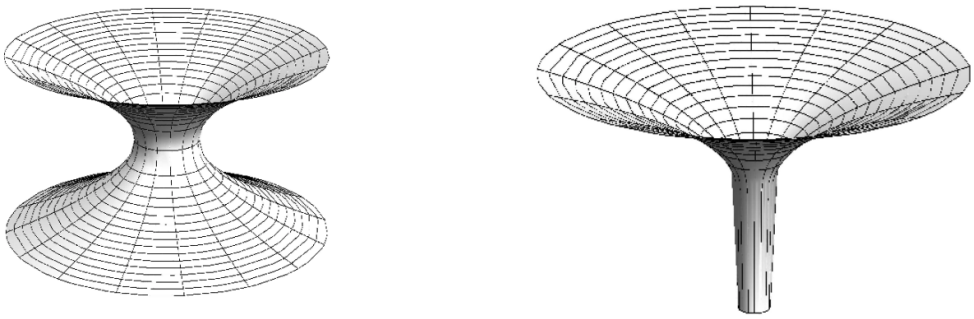

Figure 2.8: Visualization of the moving puncture simulation. The wormhole geometry (left panel) of the initial time slice evolves to the stationary trumpet topology (right panel) [52].

The GW radiation in NR simulations is commonly expressed through the Newman Penrose scalar Ψ_4 [54]. The Ψ_4 measurement is less ambiguous than measuring the small perturbation on a flat background. This quantity is a component of a Weyl tensor in a particular complex tetrad expressed by the second time derivative of the strain,

$$\Psi_4 = \frac{\partial^2 h}{\partial t^2} = \frac{\partial^2}{\partial t^2}(h_+ - ih_\times). \tag{2.80}$$

[4]Cauchy surface is a hypersurface in spacetime, i.e. a 3-dimensional region in the 4-dimensional spacetime that can be defined as all of space at a given time.

h is obtained by performing two numerical integrations of Ψ_4. Although the integration constants can be obtained through the fitting procedure, a small numerical error in Ψ_4 may be enlarged by the integrations. These numerical errors cause nonlinear drifts in the waveform.

To reduce the errors in Ψ_4, one can extract Ψ_4 to spin-weighted spherical harmonics. Following the description in Ref. [55], the strain components are expressed by the following relation,

$$h_+^{\ell m}(t) - i h_\times^{\ell m}(t) = \int^t \Big(\int^{t'} \Psi_4^{\ell m}(t'') dt'' \Big) dt' + A^{\ell m} t + B^{\ell m}, \tag{2.81}$$

where $h_+^{\ell m}$ and $h_\times^{\ell m}$ are the GW polarization in ℓm mode, will be explained later in the text. The constants $A^{\ell m}$ and $B^{\ell m}$ need to be fixed by the positioning in some physical condition. For example, setting the value of the strain to be small enough near zero towards the end of the computation.

Following Eq. (2.81), we decompose the strain in Eq. (2.72) into GW modes h_{lm}, owing to *spin-weighted-spherical harmonics* with spin-weighted $s = 2$. Here we introduce the basis function of the sphere ${}^{-s}Y_{\ell m}(\theta, \phi)$ as a function of sky location defined as:

$${}^{-2}Y_{\ell m}(\theta, \phi) = \sqrt{\frac{2\ell + 1}{4\pi}} d^{\ell}_{ms}(\theta) e^{im\phi}, \tag{2.82}$$

where d^{ℓ}_{ms} is the Wigner matrix defined by:

$$d^{\ell}_{ms} = \sum_{k=k1}^{k_2} \frac{(-1)^k [(\ell + m)!(\ell - m)!(\ell + s)!(\ell - s)!]^{1/2}}{(\ell + m - k)!(\ell - s - k)!k!(k + s - m)!} \Big(\cos \frac{\iota}{2} \Big)^{2\ell + m - s - 2k} \Big(\sin \frac{\iota}{2} \Big)^{2k + s - m}, \tag{2.83}$$

with $k_1 = \max(0, m - s)$ and $k_2 = \min(\ell + m, \ell - s)$.

For convenience, we provide explicit expressions for the leading order terms in Eq. (2.82) [56],

$$\begin{aligned} {}^{-2}Y_{22} &= \sqrt{\frac{5}{64\pi}} (1 + \cos\theta)^2 e^{2i\phi} \\ {}^{-2}Y_{2-2} &= \sqrt{\frac{5}{64\pi}} (1 - \cos\theta)^2 . e^{-2i\phi} \end{aligned} \tag{2.84}$$

This format is commonly used in the numerical community. Let us make a connection with the GW strain $h(t)$ that reads,

$$h(t; \theta, \phi) = \sum_{\ell=2}^{\infty} \sum_{m=-\ell}^{\ell} h_{\ell m}(t) {}^{-2}Y_{\ell m}(\theta, \phi) = A_{\ell m} e^{i\phi_{\ell m}}, \tag{2.85}$$

where $h_{\ell m}$ is solved numerically.

The dominant contribution of GW radiation from binaries ($e \ll 1$) is the quadrupole modes or $\ell = 2, m = \pm 2$. The relation between $\pm m$ can be exchanged through the following relation,

$$h_{\ell -m} = (-1)^{\ell} h_{\ell m}. \tag{2.86}$$

This decomposition helps our analysis because we need obtain only the $+m$ mode and apply this transformation for the $-m$.

Although NR is a promising technique to solve Einstein's equations, it is computationally expensive and time-consuming. For a comparison, PN expansion generates the waveforms within miliseconds for single waveforms, while NR may need several weeks or months. Higher resolution, longer waveforms, the choice of method, and the initial parameter may affect the timescale. Hence, only hundreds of NR data are available.

NR catalogs that are known to provide publicly open BBH simulations are

1. SXS Gravitational Waveform Database [57], contains SpEC waveforms for BBH simulations varying in mass ratios, spins, and low-eccentricities,

2. Georgia catalog [58], contains BBH simulations with different mass ratios and spins, and

3. RIT catalog of numerical simulations [59], contains waveforms with moving puncture approach for BBH simulations varying in mass ratios and spins.

In publication III [60], we select 20 NR simulations from the SXS catalog with different mass ratios and eccentricities to develop an eccentric model.

2.3.3 Inspiral-merger-ringdown model

In the previous sections, we described that the PN approximation breaks down when the binary moves towards merger. Although NR overcomes this issue, the method is computationally expensive and time-consuming. Besides, one needs to inspect the ongoing simulation repeatedly. In the late 1990s, strategies to build a complete inspiral-merger-ringdown (IMR) model by hybridizing PN approximation and NR was initially developed [61, 62] and improved over the years (see Fig. 2.9).

Two broad classes of IMR waveforms have been used widely, namely the effective one-body (EOB) formalism [62, 64, 65, 66, 67, 68, 69] and the *phenomenological* method [63, 70, 71, 72, 73, 74, 75, 76, 76, 77, 78]. Additionally,

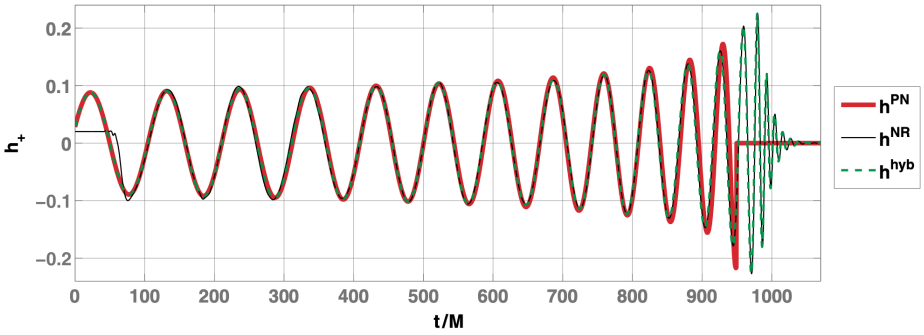

Figure 2.9: Systematic plot of a hybrid model [63]. NR simulation from an equal mass BBH system (black), 3.5 PN approximation (red), and hybrid model (dashed green).

there have been an intensive development of a new model trained from NR simulations, namely NRSurrogate [79, 80, 81, 82, 83, 84]. We explain NRSurrogate in more detail in section 2.3.4. These models have been applied in the analysis of GW data.

An essential input of the EOB formalism is the higher-order PN expansion. Instead of using the 'Taylor-expanded' form [5] of the PN results, it uses resummed form. This way, some polynomial function of v is defined to incorporate some of the unknown non-perturbative features of the PN results [85]. In the late 1990s, this method predicted GW radiation from coalescing BBH and modeled waveforms with a sharp transition from inspiral to the merger. It provided an estimate of the spin and the radiated energy of the final BH [61, 62]. Later, this waveform family has been gradually developed and calibrated to NR. We highlight BBH models for the aligned-spin (`SEOBNRv4`), precessing (`SEOBNRv3`), and the inclusion of higher-order modes (`SEOBNR_HM`). The waveforms are obtained through integration of ordinary differential equations. Thus, EOB approach is relatively slow for the direct analysis of GW data. For further details see [62, 64, 65, 66, 67, 68, 69] and references therein. We add eccentricity on the nonspinning quasicircular model (`SEOBNRv4`) in publication III.

The phenomenological family offers an alternative approach with an explicit expression in the frequency domain. The algorithm allows to simplify and speed up waveform generation from the fitting and interpolation procedure. `IMRPhenomD` [73, 74] is an aligned-spin BBH model that surpass the previous phenom models, `IMRPhenomB` [63, 70, 71] and `IMRPhenomC` [72] in 2016. This model has been used in the analysis of the first GW detection, GW150914. `IMRPhenomD` has been calibrated to 19 NR waveforms with $q \leq 18$ and spin components $\hat{\chi}\{-0.95, 0.98\}$. Essentially, each waveform in the training set is split into three regions, inspi-

[5] i.e. $c_0 + c_1 v + c_2 v^2 + \cdots + c_n v^n$

ral ($Mf \leq 0.018$), intermediate ($0.018 \leq Mf \leq f_{\rm RD}$), and the merger-ringdown ($0.5 f_{\rm RD} \leq Mf \leq 1.15 f_{\rm RD}$) area, where $f_{\rm RD}$ follows the values in Table 1 in Ref. [74]. To summarize, `IMRPhenomD` is a three-dimensional waveform model (q, χ_{1z}, χ_{2z}) and `IMRPhenomB` is a two-dimensional model ($\chi_{1z} = \chi_{2z} = \chi_{\rm eff}$) We utilize `IMRPhenomB` and `IMRPhenomD` in the enriched basis study [86].

`IMRPhenomPv2` is the precessing model that has been incorporated in the standard analysis of GW events [34]. When generating an aligned-spin case, the model reduces to `IMRPhenomD`. Ref. [77] modifies the waveform by adding a tidal parameter for BNS signal, known as the `IMRPPhenomPv2_NRTidal` model. Later, phenomenological family is developed further with the inclusion of higher order multiple moments [87].

Further development in the calibration and speed occurs in 2020 with a set of new waveform models, `IMRPhenomX` [75, 76, 76]. `IMRPhenomXPHM`, a recent phenom model that includes higher order multiple moments has been used in the recent analysis of GWs detection [10].

Strategies to include eccentricity in both families are currently being developed. The development of an eccentric model from any nonspinning circular analytical model was an important part of my work (see [60]).

2.3.4 Reduced order modeling

The reduced order technique was originally developed as a solution to speed up `SEOBNRv2` model without losing notable accuracy [88, 89, 90]. Similar methods have been proposed to interpolate inspiral part of the time-domain waveforms through singular value decomposition (SVD) [91, 92, 93, 94], a matrix factorization method that has been widely used in many numerical applications of linear algebra such as principal component analysis. The reduced-order model (ROM) approach utilizes SVD to speed up the waveform generation by a factor of thousands. Thus, parameter estimation (PE) studies can be carried out within days instead of months.

Following the description in Ref. [89], a set of n input model is generated within the parameter space of interest and frequency range as densely as desired. The input set is decomposed into amplitude and phase, where each component is packed in a regular grid in the parameter space. In later studies, different placing strategy can also be applied. The frequency grids for amplitudes and phases are defined separately. Similarly, one needs to generate a set of sparse waveforms within the parameter boundaries and the frequency grids of the input step above.

The amplitudes and phases of the input set is packed into an $n \times m$ matrix form, where n is the number of waveforms, and m is the number of frequency samples. For each matrix, one needs to compute the reduced basis via SVD to obtain two orthonormal matrices, and a decreasing list of singular values that indicates im-

portant contribution of the projection. We explain the theoretical background of SVD more detail in publication I [86]. One takes the k dominant contributions of the left singular vectors to calculate the reduced basis amplitude $\mathcal{B}_{\mathcal{A}}$ and phase $\mathcal{B}_{\Phi}$.

The projection coefficients are calculated using matrix multiplication between the transpose of the reduced basis and the sparse waveform set. To generate waveforms with a desired set of parameters, one needs to interpolate the projection coefficients in the parameter of interest and transform it back using matrix multiplication with the reduced basis. The amplitude and phase are combined back to build a full waveform model.

The ROM method has been adopted in the development of `NRSur7dq4`, a precessing model trained from 1528 NR simulations. `NRSur7dq4` has relatively narrow parameter boundaries ($q \leq 4, \chi_1, \chi_2 \leq 0.8$) and claimed to have an accuracy of above 0.99 against NR computed with the Advanced LIGO design sensitivity noise curve [82].

We modify the ROM method in our study in [86] using two different models and iterative technique. Furthermore, we explore the dimensionality reduction from a set of waveforms with higher dimensional parameters onto the lower ones. The accuracy declines as we involve broader parameters. This issue is highlighted in this study, where we propose a new method and analysis the solution to tackle the higher-dimensional problems [95]. We explain in more detail in chapter 3 and publications I, II.

In a similar spirit, a modification of the ROM technique has been used in the PE studies [96, 97]. These studies adopt the reduced basis and interpolation in the ROM techniques to approximate Bayesian probability density functions and accelerate the analysis of the signals. Two packages are widely used in the development of the reduced-order quadrature (ROQ) model, namely greedycpp [98, 99], and PyROQ [100, 101]. These packages provide a framework to speed up the source parameter analysis.

3
This dissertation

"Everything should be made as simple as possible, but not simpler."

Albert Einstein

This dissertation examines mathematical and computational techniques to improve waveform models to analyze GW signals from BBH coalescences. We propose methods and analyses that lie between analytical and numerical relativity. The main aim of these studies is to develop with as simple as possible method yet a faster and reliable waveform model. The results have been published in three peer-reviewed papers [86, 95, 60]. Those articles are included unmodified (formatting aside) in chapters publication I, II, and III. This chapter summarizes our studies.

Publication I [86] investigates mathematical methods to tune waveform models dynamically. Analytical models such as PN or untuned EOB families are fast to generate, but their their accuracy declines towards merger. Conversely, numerical simulations are computationally expensive but known to have better accuracy. Calibration is needed to increase the accuracy of the analytical models without losing the speed to build the waveform. However, manual calibration often demands excessive human resources. Our research question was motivated by the need to calibrate analytical waveform models with NR automatically. We divide this study into two parts.

In the first part, we develop a strategy for two models with the same dimensional parameter. We project a set of a more accurate (but higher computational cost) model onto the basis of a less accurate (but lower computational cost) model.

The basis was built by decomposing a set of fast-less accurate waveforms through SVD, a standard mathematical technique for data reduction. Technical details about SVD are explained further in the introduction section of chapter publication I. We then interpolate the projection coefficients for the desired parameters and iterate the process to build a new model. The resulting waveforms are computationally cheap, with an accuracy of up to 0.999 against all test datasets. For comparison, the basis waveforms have an accuracy between 0.38 and 0.99 (see Fig. I.3 and I.4 of chapter publication I). We conclude that our method is suitable for developing a faster and reliable waveform model that spans a broad parameter range. The primary source of error lies in the interpolation in higher dimensions, leading us to the main research question in chapter publication II.

We explored a method to build a new set of waveforms coming from two models with different parameter-space dimensions in the second part. Our study was inspired by the efforts to update an aligned-spin model (three dimensions) with the precessing model (seven dimensions). The new waveforms are expected to have seven dimensions precessing model. Besides, they can quickly build a precessing model and avoid complex calculations. We investigate a proof of concept by projecting a set of three-dimensional models onto the basis of two-dimensional model. We conclude that the resulting waveforms reach our expected accuracy. The speed to build the waveforms is affected by the three-dimensional interpolation and the placing of the training dataset.

When including more binary parameters, we face *the curse of dimensionality*, a term used to express that everything becomes more complicated, lengthy, and requires more computational power with higher dimensions. Implementing a precessing model that includes seven-dimensional parameters ($q, \vec{\chi}_1, \vec{\chi}_2$) would require a larger training dataset and complexity than the aligned-spin case (q, χ_{1z}, χ_{2z}). We investigate various regression methods to tackle regression problems in waveform modeling in chapter publication II [95]. This study was initiated to answer the problem we had in the first publication and the issues highlighted by the ROM community during a workshop in 2018 [102]. We highlight that various waveform families employ regression, interpolation, or fitting techniques in their pipeline. Thus, understanding regression techniques is essential in the development of waveform modeling.

Furthermore, an ever-increasing machine-learning (ML) use in GW science motivated us to answer whether such computational complexity is necessary. In this study, we explore regression methods that are categorized into traditional and ML methods. We provide the mathematical and computational background for the traditional methods such as linear interpolation, polynomial interpolation, tensor-product-interpolation (TPI), radial basis functions (RBF), and greedy multivariate polynomial fits (GMVP). Similarly, we also explore ML techniques such as Gaussian process regression (GPR) and simple artificial-neural-networks (ANN).

Publication II [95] presents the theoretical background and our setup for each regression method, including ML. We also compare the performance of these methods, namely the maximized overlap and the time required to produce the waveform data at a point in time for the aligned-spin and precessing model. Our results show that the difference between traditional and ML is negligible. Thus, we suggest that ML for building waveform models is less important, at least up to seven dimensions. A well-known method such as polynomial interpolation may provide reliable results with a shorter computational time. However, when we include more parameters, such as the combination of mass, spins, and eccentricity, machine learning may be faster and more accurate than other methods.

Publication III [60] provides a concrete implementation to develop a faithful and straightforward model for an eccentric BBH system. The detection of such a system would significantly help our understanding of binary evolution and population synthesis. At the time of this writing, no GWs from an eccentric BBH merger have been detected. However, recent studies suggest signals from a detection event namely GW190521, is originated from an eccentric BBH [103, 104]. Eccentric models are crucial in the analysis, especially since future GW detectors will observe binaries with higher SNR, making it possible to see more BBH collisions. The study of eccentric orbits has become more demanding, especially after the observation of GW190521, a BBH collision with high component masses [103]. Ref [104] discusses the properties and astrophysical implications of such a system. Possible sources of this event may include a highly eccentric binary with $e > 0.1$. However, the development of an eccentric model is relatively slow compared to the aligned-spin, precessing, and higher-order-modes systems. It may be due to relatively low numbers of eccentric NR simulations available and our knowledge of the system's dynamical evolution.

We develop an algorithm to turn any analytical nonspinning circular model into an eccentric one focusing on the late inspiral to the ringdown regime. We start with 20 nonspinning, low-eccentric NR simulations from the publicly open SXS catalog. We split these simulations into 12 training and 8 test dataset. The amplitude and frequency of these waveforms show characteristic oscillatory behavior for different eccentricities and mass ratios. Our strategy is to model the residual oscillation known as the *eccentricity estimators* with four fitting coefficients. These coefficients are strongly related to mass ratios and eccentricities. We interpolate these coefficients to reconstruct the new eccentricity estimators with the desired parameters. We then apply the new eccentricity estimators on an analytical quasicircular model to add eccentricities. This way, we turn nonspinning quasicircular models, `IMRPhenomD` and `SEOBNRv4` into eccentric models. Our results show that the maximized overlap of the *quasicircular turned eccentric* model against eccentric NR is at least 0.98 in all test datasets. As a concrete implementation, we create a publicly open Python package `pyrex` [105] to carry out

the computation. Furthermore, we examine the prospect of observing eccentric binaries with third-generation detectors.

We plan to develop further studies on building a complete IMR eccentric model. The late inspiral results from our computation are hybridized with the early inspiral regime from PN expansion [38].

Publications

I

Enhancing gravitational waveform models through dynamic calibration

Yoshinta Setyawati[1,2], Frank Ohme[1,2], Sebastian Khan[1,2]

[1]Max Planck Institute for Gravitational Physics (Albert Einstein Institute), Callinstr. 38, 30167 Hannover, Germany
[2]Leibniz Universität Hannover, 30167 Hannover, Germany

Abstract

Current gravitational wave observations made by Advanced LIGO and Advanced Virgo use theoretical models that predict the signals generated by the coalescence of compact binaries. Detections to date have been in regions of the parameter space where systematic modeling biases have been shown to be small. However, we must now prepare for a future with observations covering a wider range of binary configurations, and ever increasing detector sensitivities placing higher accuracy demands on theoretical models. Strategies to model the inspiral, merger and ringdown of coalescing binaries are restricted in parameter space by the coverage of available numerical-relativity simulations, and when more numerical waveforms become available, substantial efforts to manually (re-)calibrate models are required. The aim of this study is to overcome these limitations. We explore a method to combine the information of two waveform models: an accurate, but computationally expensive *target* model, and a fast but less accurate *approximate*

model. In an automatic process we systematically update the basis representation of the approximate model using information from the target model. The result of this process is a new model which we call the *enriched basis*. This new model can be evaluated anywhere in the parameter space jointly covered by either the approximate or target model, and the enriched basis model is considerably more accurate in regions where the sparse target signals were available. Here we show a proof-of-concept construction of signals from nonprecessing, spinning black-hole binaries based on the phenomenological waveform family. We show that obvious shortcomings of the previous `PhenomB` being the approximate model in the region of unequal masses and unequal spins can be corrected by combining its basis with interpolated projection coefficients derived from the more recent and accurate `IMRPhenomD` as the target model. Our success in building such a model constitutes an major step towards dynamically combining numerical relativity data and analytical waveform models in the computationally demanding analysis of LIGO and Virgo data.

Author's contribution

YS contributed to the development of the theory and performed the computations. SK and FO verified the analytical method and manuscript. FO presented the idea and supervised this work. Furthermore, YS wrote most of the manuscript.

Copyright Notice

I.1 Introduction

The dawn of the GW era began with the first detection of a BBH merger on September 14, 2015 [1] by the aLIGO [2]. More BBHs [3, 4, 5, 6] and one BNS merger on August 17, 2017 [7] have been observed by aLIGO and Virgo [8] during their first two observing runs.

The search for GWs requires coincident signals in at least two instruments. In order to uncover signals of astrophysical origin hidden behind the instruments' noise, their data are filtered with a large number of waveform templates [9]. More than one hundred thousand templates of coalescing compact binaries were employed in aLIGO GW searches during each of the first two observing runs. An order of magnitude more modelled waveforms are then used to estimate the source parameters and their uncertainties. More accurate and efficient follow ups of GW detections and their parameters will be needed for the following aLIGO observing runs. This implies the need for waveform models covering a wide range of parameter space that can be generated quickly.

The GW signal emitted by coalescing binaries depends upon many different parameters that are often grouped into intrinsic and extrinsic parameters. Intrinsic parameters are astrophysical parameters of the binary. These are two mass parameters: the chirp mass ($\mathcal{M}_c$) and the symmetric mass ratio η; eccentricity; tidal parameters for neutron stars; and the spin components of the two objects ($\vec{\chi}_1, \vec{\chi}_2$) that are often represented by the dominant, effective spin parameter ($\chi_{\rm eff}$) in the case of non-precessing binaries. The exact definition of these parameters will be introduced in section I.

In this study we focus on non-precessing BBHs for which the spins are (anti-)aligned with the binary's orbital angular momentum. The dimensionless tidal parameters are set to zero. Eccentricity has also been neglected in all aLIGO GW searches that employ modelled templates so far, mainly because for most plausible astrophysical formation scenarios, the binary is expected to have circularized by the time its GW signal enters the aLIGO frequency range. However, future waveform developments might include the eccentricity of the binary.

In addition to these properties, extrinsic parameters define the location and orientation of the source relative to the observer, such as the luminosity distance (D_L), inclination angle (ι), sky position (RA, Dec), polarization angle (Ψ), time of coalescence (t_c), and phase of coalescence (ϕ_c) [10]. For non-precessing systems, modifications in these parameters simply shift the waveform in time, phase or amplitude, and they are much simpler to model than changes in intrinsic parameters.

In order to predict GW signals from binaries, one needs to solve the Einstein equation in GR. Analytical approximations have been established in form of PN expansions. These are asymptotic expansions in a small parameter such as the

ratio of the characteristic velocity of the binary to the speed of light [11, 12]. By the nature of the approximation, PN expansions become increasingly inaccurate as the two bodies move closer to each other and faster, entering the strong gravity regime. At this stage, NR simulations provide the only viable approach to solve the Einstein equation [13]. In general, NR waveforms can in principle be very accurate and the accuracy can be tested through different types of convergence tests, but they are computationally extremely expensive [14, 15, 16, 17].

Hence, many efforts in the past focused on bridging PN and NR [18, 19], leading to a variety of EOB and phenomenological waveform models that are used in aLIGO's analyses. EOB is an analytical method proposed by Buonanno and Damour [20, 21, 22, 23, 24, 25, 26, 27] which substantially reformulates PN results into a new description of the binary coalescence beyond the inspiral phase. A different approach was developed to build phenomenological models (see I) that essentially model coalescing binaries using analytical fits of PN-NR hybrids.

However, both approaches depend on a number of tunable parameters and fits whose optimal form and values are determined through complex procedures that typically require a fair amount of human input. Therefore, updated models that incorporate new NR data and improved analytical descriptions typically take years to develop.

A different method to generate an accurate waveform model is based on sophisticated interpolation methods to create a *surrogate* model [28, 29, 30] of NR waveforms. These surrogate models have a high accuracy to the original NR waveforms, however, they are limited to the parameter space covered by the original simulations. Although boundaries are constantly being expanded in parameter space, this modeling strategy relies on large amounts of computational power. At the time of writing this article, the latest precessing surrogate model [28] is limited in mass ratio and dimensionless spin magnitude to $q \leq 2$ and $|\chi| \leq 0.8$, respectively.

Here we explore a complementary method of constructing a waveform model that combines the information of an existing (computationally efficient) model with more accurate waveforms that are only available in a limited set of points in the parameter space. A future application of our method would be a dynamical (i.e., fully automized) update of an analytical model with NR waveforms to produce a new waveform model that can be evaluated continuously and has a better accuracy than the original model.

To develop our method, here we employ two analytic phenomenological models: PhenomB [31] being the *approximate, less accurate* model and PhenomD [32, 33] being the *target, more accurate* model.

We use SVD to decompose the approximate model into an orthogonal basis and update the basis coefficients using information from the more accurate model. Similar ideas of using SVD to improve waveform models have been presented by

Cannon et al [34, 35, 36] and Pürrer [37, 38].

Cannon et al explore the use of reduced-order SVD in time domain. However, they only use one-dimensional interpolation in mass components and consider a restricted parameter space with no spin. We use a similar technique, but consider frequency-domain waveforms, and we extend the method to a much greater parameter space including spin.

Pürrer discusses the use of SVD to build computationally more efficient ROMs of existing spinning, non-precessing EOB models. ROMs are now a standard tool to reduce the time taken to generate a waveform, but the resulting accuracy is that of the original model, or slightly less in challenging points of the parameter space.

Throughout this article geometric units are used by setting $G = c = 1$.

I.2 Methodology

I.2.1 Waveform models

The constantly increasing sensitivity of GW interferometers demands ever more accurate models. Updating and improving models is a major tasks entering the era of GW astronomy, and we present a first end-to-end test of a fully automatic tuning that in future will use NR simulations to improve analytical models. Here, however, we start with a proof-of-concept using two phenomenological waveform models.

The phenomenological family is a set of approximate waveform models, written as closed-form analytical expressions in the frequency domain [39, 40, 31, 41, 42, 33]. These models have been calibrated to NR waveforms that naturally cover a limited region of the intrinsic parameter space. However, the most recent models [42, 33] have been shown to be perfectly suited for current BBH observations with mass ratios close to unity.

As explained in section I, we use PhenomB as the *approximate, less accurate model* that we aim to update with information from PhenomD as the *accurate target model*. PhenomB [31] was the first (anti)-aligned spin model of this family, released almost simultaneously with an alternative description of the same parameter space, called PhenomC [41]. Both models were calibrated up to mass ratios of 4 and BH spins up to 0.75. They have known shortcomings when extrapolating beyond the region of calibration, especially towards more extreme mass ratios. PhenomD is the most recent and most sophisticated version of aligned-spin phenomenological models. It has been calibrated to 19 NR waveforms from the SXS collaboration [43] and the BAM code [44, 45] that span mass ratios from unity up to 18 and dimensionless spin magnitudes up to 0.85 (0.98 for equal-mass systems) [32, 33].

The intrinsic parameters of relevance in the non-precessing case are the mass ratio q, or equivalently the symmetric mass ratio η,

$$q = \frac{m_1}{m_2} \geq 1, \qquad \eta = \frac{m_1\, m_2}{(m_1 + m_2)^2}, \tag{I.1}$$

as well as the dimensionless spin projections along the orbital angular momentum χ_{1z}, χ_{2z} (non-vanishing spin components perpendicular to the orbital angular momentum cause precession effects that we leave for future work). For vacuum solutions of Einstein's Equation, the total mass $M = m_1 + m_2$ is a simple scaling factor.

We emphasize that the spin degrees of freedom in a binary are commonly reduced in phenomenological models to the observationally relevant dominant parameter combinations. Following the analysis in [31, 41] for aligned-spin binaries, the dominant spin effect in GW phase can be expressed as the weighted combination of individual BH spins,

$$\chi_{\rm eff} = \frac{m_1 \chi_{1z} + m_2 \chi_{2z}}{m_1 + m_2}. \tag{I.2}$$

Apart from an overall time and phase, PhenomB exclusively depends on $\chi_{\rm eff}$ and η. PhenomD uses $\chi_{\rm eff}$ for the coefficients that were tuned to NR simulations, however, through the inspiral and the final state portion of PhenomD inherits two-spin dynamics. In section I we will apply our method to the 3D problem (η, χ_1, χ_2) and express our results in terms of the symmetric $(\chi_{\rm eff})$ and anti-symmetric (χ_a) spin parameters where (χ_a) is defined as

$$\chi_a = \frac{\chi_{1z} - \chi_{2z}}{2}. \tag{I.3}$$

In the following sections, we present the details of how to update PhenomB with the more accurate PhenomD waveforms in frequency domain for a given range of $\eta, \chi_{\rm eff}$ and scaled by the total mass M. The end result of this computation is a new waveform model that is closer to its target waveforms. We call this new family as the *enriched basis (EB)* waveforms.

I.2.2 Parameter ranges

This exploratory study is designed to test our method across a wide range in parameter space. Here, we essentially consider the range in mass ratio and spins where PhenomD has been calibrated to NR waveforms (see section I),

$$\eta \in [0.05, 0.25], \qquad \chi_{\rm eff} \in [-1, 1]. \tag{I.4}$$

We stress that this region in the parameter space includes a considerable part where PhenomB has not been calibrated, e.g., mass ratios above 4 ($\eta < 0.16$). What we are going to show is that despite the fact that the underlying approximate model does not accurately describe signals in certain regions, using accurate signals to update the approximate basis representation can entirely fix that problem.

In order to fully determine the signals for our test case, we fix the following additional parameters,

$$\begin{aligned} M &= 50M_\odot, & f_{\rm low} &= 30\,{\rm Hz}, \\ \Delta f &= 0.1\,{\rm Hz}, & Mf_{\rm high} &= 0.2, \end{aligned} \tag{I.5}$$

where $f_{\rm low}$ and $f_{\rm high}$ are the values of the lowest and the highest frequency we consider, respectively, and Δf defines the numerical discretization of the signal. $Mf_{\rm high} = 0.2$ is chosen to be slightly higher than the signal with the largest ringdown frequency in our dense grid[1]. For $M = 50M_\odot$, $f_{\rm high}$ corresponds to 812 Hz.

Following the above choice of parameter ranges, we create two two-dimensional (2D) uniform grids in η and $\chi_{\rm eff}$. We build a *dense grid* of approximate PhenomB waveforms, and a *sparse grid* of accurate PhenomD waveforms (see Fig. I.1 for visual representation). Our dense grid contains $N = 65 \times 65 = 4225$ signals, and the sparse grid has $S = 33 \times 33 = 1089$ signals. Thus, about 25% of the approximate waveforms have the same η and $\chi_{\rm eff}$ as the target waveforms.

On each point of each grid, we generate the GW polarizations, $h_{+/\times}$. In this work, we only consider non-precessing signals and their $(\ell, |m|) = (2, 2)$ multipoles which means that the extrinsic parameters, such as the orientation and location of the binary, simply scale the amplitude of the signal and introduce a constant phase shift. We can treat these trivial dependencies independently and, at this stage, normalize all waveforms to have the same extrinsic parameters. We then use the software library `LALSuite` [46] to generate the GW polarizations.

In this study, both approximate and target models are inexpensive to compute, so we can test our method for large numbers of target-model waveforms. In the future, we will use target waveforms that come from computationally expensive methods such as NR simulations. In that situation we may not have access to signals at arbitrary points in parameter space and we will have fewer waveforms. Here we first choose a reasonably high number of target waveforms, and later discuss how low this number can become to still produce satisfactory results.

[1]The system with the highest ringdown frequency will be the equal-mass, maximally spinning case ($\chi_{\rm eff} = 1$) which has dimensionless ringdown frequency of ~ 0.13.

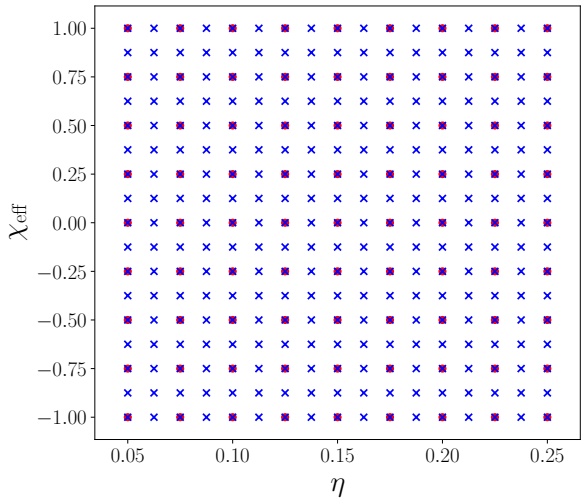

Figure I.1: Illustration of the two uniform grids we consider in η-χ_{eff} parameter space. The blue crosses illustrate the dense grid *of approximate signals that we use to build an SVD basis, and the red circles are the* sparse grid *of accurate signals we use to update the model.*

I.2.3 Waveform matrices

In our method we will represent the waveform manifold of the *approximate* model with a set of orthogonal basis functions computed using SVD. First, we prepare our dataset in appropriate matrix form which we can factorize subsequently. The procedure is explained by the following steps.

I.2.3.1 Waveform decomposition

The frequency-domain strain $\tilde{h}(f)$ is the combination of both GW polarizations , where f is defined for positive frequencies. Here we assume the circular polarizations of GW and describe $\tilde{h}(f)$ as follows: [2]

$$\tilde{h}(f) = \tilde{h}_{+}(f) + i\,\tilde{h}_{\times}(f)\,. \tag{I.6}$$

We note that if we express $\tilde{h}_{+/\times}(f)$ in terms of their amplitudes, $\mathcal{A}_{+,\times}$, and phases, $\Psi_{+,\times}$, factoring out the dependency on the inclination angle, ι, we obtain

[2] In other literature, the strain is sometimes defined as $h_{+} - ih_{\times}$, owing to a different convention of the Fourier transform. Here we adopt the definition used in LIGO algorithm library (LAL), $\tilde{h}(f) = \int h(t)\, \exp(-i2\pi f t)\, dt$

the following expressions [10]:

$$\tilde{h}_+(f) = \mathcal{A}_+(f)\, e^{i\Psi_+(f)}\Big(\frac{1+\cos^2\iota}{2}\Big), \tag{I.7}$$

$$\tilde{h}_\times(f) = \mathcal{A}_\times(f)\, e^{i\Psi_\times(f)}\cos\iota\,. \tag{I.8}$$

The non-precessing signals we consider further satisfy a simple relation between the polarizations,

$$\mathcal{A}_+ = \mathcal{A}_\times, \qquad \Psi_\times = \Psi_+ - \frac{\pi}{2}. \tag{I.9}$$

While (I.9) is exactly valid only in the limit of large separations, assuming it through merger and ringdown is a commonly made approximation that does not introduce inaccuracies relevant to today's analyses.

By computing $\tilde{h}_+$ and $\tilde{h}_\times$ for $\iota = 0$, we can now decompose $\tilde{h}(f)$ into amplitude and phase components,

$$\tilde{h}(f) = 2\mathcal{A}_+(f)\; e^{i\Psi_+(f)}\,. \tag{I.10}$$

In this form, we can focus on two real-valued functions: the strain's amplitude and phase (we drop the '+' subscript henceforth). This decomposition is convenient because amplitude and phase are simpler, real-valued, non-oscillatory functions which are better suited to perform SVD than the oscillating strain.

Once we have constructed the improved EB amplitude $\mathcal{A}_{\rm EB}(f)$ and phase $\Psi_{\rm EB}(f)$, we can combine them again into the EB strain $\tilde{h}^{\rm EB}(f)$, as well as individual polarizations, using Eqn. (I.7)-(I.10).

I.2.3.2 Phase alignment

Time and phase shifts enter the frequency-domain waveform through the GW phase $\Psi(f)$ according to

$$\Psi'(f) = \Psi(f) + 2\pi f t + \psi, \tag{I.11}$$

where t is the amount of time shifted and ψ is the phase shift.

We use (I.11) to align the phases in our approximate waveform grid by determining the time and phase shift individually for each configuration such that the square phase difference with one fiducial case is minimized. Specifically, we align the phases against the first case in our grid ($\eta = 0.05, \chi_{\rm eff} = -1$), although any other choice yields comparable results. By aligning the phases before performing the SVD we remove variations between the phases that are purely due to time and phase shifts. These variations can always be re-introduced analytically via (I.11). The shifted phase is denoted by $\Psi_B(f)$.

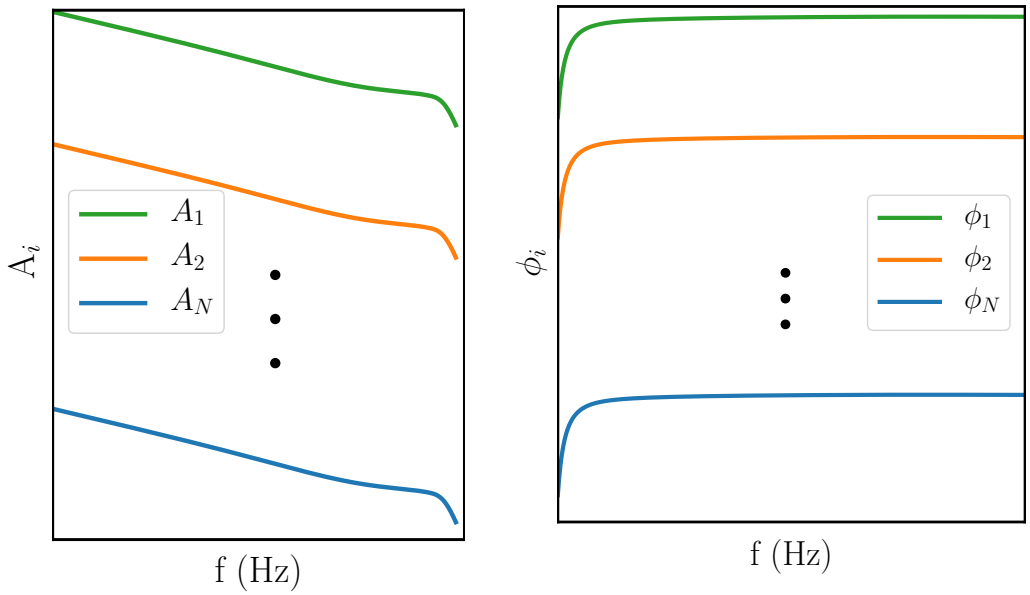

Figure I.2: Illustration of N signals, each of length L, decomposed into amplitudes (left) and phases (right) packed into two matrices.

I.2.3.3 Matrix form

We generate N signals from the approximate model PhenomB, each discretized at $L > N$ points in frequency domain between f_{low} and f_{high}. After computing the strain $\tilde{h}(f)$ from the two polarizations as explained in the previous section, we decompose them into amplitude and phase then align the phases. We then pack all amplitude and phase arrays into a matrix, respectively (see Fig I.2) Specifically, the rows of the matrices are arranged from the lowest (η, χ_{eff}) to the highest (η, χ_{eff}).

We repeat the above procedure and generate S target waveforms, using PhenomD, on the sparse grid, where $S < N < L$. At this point, we have four matrices: two amplitude matrices and two phase matrices; one of each type for each approximant. The matrices of the approximate model PhenomB have the dimensions $\mathbb{R}^{N\times L}$ while the target PhenomD model matrices are $\in \mathbb{R}^{S\times L}$. With this prepared, we perform an SVD as discussed in subsection I.

I.2.4 The Singular Value Decomposition

Our goal is to generate a new waveform family that can be evaluated for arbitrary parameters from interpolating a set of sparse target waveforms. To do this, we project our target model onto a basis of the approximate model, generated from

a grid that is as dense as possible and computationally feasible. As a first step, the basis is built by an appropriate factorization of the grid of the approximate waveforms.

There are two main strategies to factorize sets of waveforms. One uses a Gram-Schmidt orthogonalization to obtain the basis from a first set of approximate waveforms followed by a greedy algorithm to extend the basis until an acceptable error limit is reached [28, 47, 48]. The second strategy uses the SVD as in Cannon et al [34, 36, 35] and Pürrer [37, 38, 49] to factorize each matrix into two unitary matrices and one diagonal matrix with elements sorted in descending order. The comparison between the two strategies has been discussed in [28]. Here we use the SVD because it produces smoother result, and because it is elegant and convenient given that it sorts the contribution from the dominant basis vector to the least important ones. This ensures that the error caused by SVD truncation is generally small.

We adopt SVD to individually factorize amplitude and phase matrices ($\boldsymbol{P}$) of PhenomB into two unitary matrices ($\boldsymbol{U}$ and $\boldsymbol{V}$) and one diagonal matrix $\boldsymbol{\Sigma}$ [50],

$$\boldsymbol{P} = \boldsymbol{U}\boldsymbol{\Sigma}\boldsymbol{V}^T. \tag{I.12}$$

Here, $\boldsymbol{U} = [u_1|\ldots|u_p] \in \mathbb{R}^{N\times p}$ and $\boldsymbol{V} = [v_1|\ldots|v_p] \in \mathbb{R}^{L\times p}$ are orthogonal matrices and the superscript T denotes the transpose of the corresponding matrix. The vectors u_i and and v_i are left and right singular vectors of $\boldsymbol{P}$ respectively. The singular values $\boldsymbol{\Sigma} = \mathrm{diag}(\sigma_1, \ldots, \sigma_p) \in \mathbb{R}^{p\times p}$ is a diagonal matrix sorted in descending order, where $p = \min(N, L)$, which in our setup yields $p = N$. The diagonal elements σ_i^2 are the eigenvalues of $\boldsymbol{P}^T\boldsymbol{P}$.

SVD can be interpreted as matrix decomposition into a weighted sum of separable matrices, meaning that a matrix $\boldsymbol{P}$ can be written as an outer product of two vectors $\boldsymbol{P} = \bar{\boldsymbol{u}} \otimes \boldsymbol{v}^T$ ($\bar{\boldsymbol{u}}$ denote the u vectors weighted by the singular values). The rank of this outer product depends on how many singular values are involved in the sum. The index notation of the above reads

$$P_{ij} = \sum_{k=1}^{p} u_{ik}\ \sigma_k\ v_{kj}^T. \tag{I.13}$$

I.2.5 Projection coefficients and reduced order

In our study, we use Eq. (I.13) in the following way. Every row of the matrix P_{ij} represents a Fourier-domain series of either amplitude or phase; the index j represents individual frequency samples. Every one of those Fourier-domain series is expressed on the right-hand side as a linear combination of orthogonal basis vectors $(V^T)_{kj}$ (k is the index of the basis, j specifies the frequency) multiplied

with coefficients $c_{ik} = u_{ik}\ \sigma_k$ (k corresponds to the associated basis, i specifies the frequency series that is reconstructed in this way). We call c_{ik} the projection coefficients. The projection coefficients can be interpreted as updating the left singular vectors u_{ik} weighted by the rank of singular value σ_k.

In order to build an analytical model that can be evaluated continuously across the parameter space, the projection coefficients need to become functions that interpolate in the parameter space between the discrete points given in the rows of P_{ij}. We emphasize this below by replacing the index i with the explicit functional dependency on η and $\chi_{\rm eff}$, leading to

$$c_k(\eta, \chi_{\rm eff}) = \sum_{j=1}^{L} P_j(\eta, \chi_{\rm eff})\ V_{jk}. \tag{I.14}$$

The sum now describes a discretized inner product $\langle \cdot, \cdot \rangle$, so that (I.14) becomes

$$c_k(\eta, \chi_{\rm eff}) = \langle P(\eta, \chi_{\rm eff}), v_k \rangle\,. \tag{I.15}$$

Again, P in this expression represents either the amplitude or phase for the parameters $(\eta, \chi_{\rm eff})$, v_k are the basis vectors calculated via SVD.

Different from standard practise in SVD and ROM, we now proceed by calculating coefficients from projecting the *target* waveforms' amplitude and phase onto the basis representation of the *approximate* waveform, respectively. In addition, we study a reduction of the basis size that is achieved by only considering the first K coefficients. K then reduces the rank of the singular values matrices [35], and it enters (I.13) as the upper limit of the sum instead of p. This reduced order is introduced to increase computational efficiency and to decrease memory requirements when building the EB in comparison to the full basis $k = N$.

By updating the approximate (less accurate) waveforms basis coefficients with information from the (more accurate) target waveforms we have manipulated the basis representation of approximate waveforms to be closer to target waveforms. Hence, we name this process *enriching the basis*.

I.2.6 Interpolation

To construct our enriched basis model, we calculate the approximate SVD basis and project the target amplitude and phase onto the respective basis vectors, giving us projection coefficients according to (I.14) on the sparse grid in parameter space (recall, the sparse grid is where we have access to accurate target signal). We then interpolate the projection coefficients and calculate their values on all points on the dense grid, so that we can compare with all approximate signals that we needed to start this process.

We stress that the dimensionality of the interpolation depends on the target model. For equal-spin case, we use two-dimensional interpolation $(\eta, \chi_{\rm eff})$ in parameter space, and later we consider two independent spins, where we need three-dimensional interpolation. Here we employ cubic spline interpolation as the most efficient and easy method for this project. However, different interpolation methods such as Chebyshev polynomials [35], tensor product interpolation [23], Gaussian interpolation [51] and empirical interpolation [29] have been used in different studies. For the future, it will be beneficial to compare all these methods systematically, evaluating computational efficiency, accuracy and generalisability to higher dimensions.

Once the target waveform's coefficients, that we denote by $c'(\eta, \chi_{\rm eff})$, have been obtained, we combine them with the basis vectors to calculate the EB's amplitude and phase,

$$P_j^{\rm EB}(\eta, \chi_{\rm eff}) = \sum_{k=1}^{K} c'_k(\eta, \chi_{\rm eff}) v_{kj}^T. \tag{I.16}$$

Having amplitude and phase, we can build $\tilde{h}^{\rm EB}(\eta, \chi_{\rm eff})$ using Eq. (I.10).

I.2.7 Match and improvement evaluation

Once the EB strains $\tilde{h}^{\rm EB}$ have been calculated, we evaluate their accuracy and improvement of EB model relative to its approximate and target models. We then test the accuracy of EB model both at points where the target model was used to update the projection coefficients, as well as at points where no target signals were available and we use the interpolated projection coefficients. To perform the evaluation, we compute *matches* between PhenomB and PhenomD and compare them to the matches between EB and PhenomD.

The match is defined as the normalized, noise-weighted inner product between two waveforms h_1 and h_2 [10], maximised over relative time and phase shifts between them,

$$O = \frac{\langle h_1, h_2 \rangle}{||h_1|| ||h_2||} = \max_{\phi_0, t_0} \left[4\,{\rm Re} \int_{f_1}^{f_2} \frac{\tilde{h}_1(f)\, \tilde{h}_2^*(f)}{S_n(f)} \frac{df}{||h_1|| ||h_2||} \right]. \tag{I.17}$$

Here, ϕ_0 and t_0 are relative phase and time shifts between the waveforms, respectively, and $||h||^2 = \langle h, h \rangle$. $S_n(f)$ is the noise spectral density of the detector, $\tilde{h}^*$ denotes the complex conjugation of $\tilde{h}$, and (f_1, f_2) is a suitable integration range which corresponds to $f_{\rm low}$ and $f_{\rm high}$ respectively. We use two noise spectra in our analysis, flat noise ($S_n \equiv 1$) and the aLIGO zero detuned high power density (AZDHP) which is the anticipated design sensitivity of aLIGO in 2020 or later [52]. The motivation behind using a flat power spectral density (PSD) is to

evaluate the signal agreement with equal weight on all frequencies independent of an assumed instrument, whereas using AZDHP allows us to relate our results to GW analysis applications.

Matches are close to unity where waveforms agree (see section I), so it is easier to compare the difference between two models by quoting the mismatch, defined as

$$\mathcal{M}(h_1, h_2) = 1 - \mathcal{O}(h_1, h_2). \tag{I.18}$$

Finally, to quantify the accuracy improvement of the EB model over the approximate model PhenomB, we define improvement, $\mathcal{I}$, as the mismatch of the approximate waveform with the target model divided by the mismatch of EB model with the target,

$$\mathcal{I}(h_1, h_2) = \frac{\mathcal{M}(h_1, h_3)}{\mathcal{M}(h_2, h_3)}, \tag{I.19}$$

where in this study, h_1, h_2 and h_3 correspond to PhenomB, EB, and PhenomD respectively.

I.3 Results

We have outlined a technique to build a more accurate waveform model in the above section. Here we present results and analyses based on two different assumptions about the spins in the target parameter space, *equal-spin* ($\chi_{\rm eff}$=χ_1=χ_2) and *double-spin*, where χ_1 and χ_2 are varied independently (i.e., χ_a does not necessary vanish).

I.3.1 Two dimensions: equal-spin systems

Following the above procedure, we evaluate the match between the EB model and the target model under flat noise and AZDHP. We also compare the mismatch between the approximate model against the target model to calculate the improvement we gain.

Fig. I.3 shows the original match of PhenomB against PhenomD. It is evident that PhenomB has not been calibrated to mass ratios above 4, and the agreement between the two models deteriorates quickly, especially for high spins.

Fig. I.4 presents the matches of EB against PhenomD without invoking any interpolation. Recall, EB here is based on basis vectors derived from PhenomB that do not accurately represent high-mass ratio systems. However, by projecting $N = 65\times65$ PhenomD waveforms onto the basis derived from N PhenomB signals on the same points in parameter space, we see that there is enough extra freedom in the basis such that updated projection coefficients can correct for the inaccuracies

of the approximate model. Put differently, the space spanned by the approximate PhenomB basis vectors does contain more accurate signals, also for higher mass ratios, if the coefficients in front of the basis vectors are adapted appropriately. This might not be a surprising result, given the fairly large number of basis vectors we use; it is not a trivial result either.

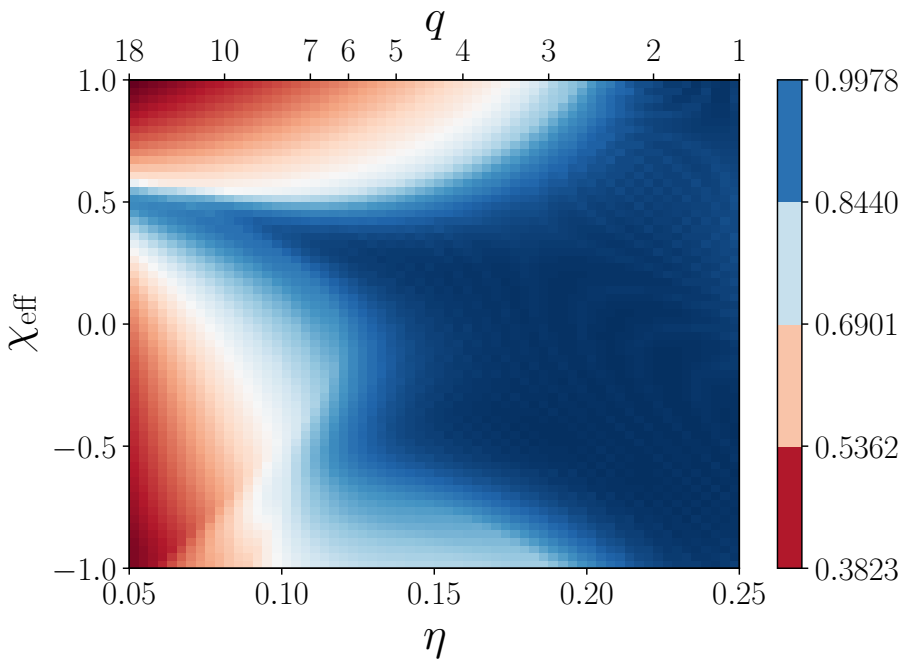

Figure I.3: Matches of PhenomB against PhenomD under flat PSD.

Of course, this is not a useful application of the method we develop. If one has access to N accurate waveforms, there is no need build an approximate basis first. Now we reduce the number of accurate waveforms to $S \approx N/4$, and interpolate the projection coefficients to calculate EB signals on all N grid points. The mismatch result is shown in Fig. I.5. In most parts of the parameter space, the accuracy of EB is only very slightly lower than what was achieved in the ideal scenario shown in Fig. I.4. Interpolation therefore does not introduce significant errors for the grids chosen here. Only at the boundaries of the parameter space we find higher mismatches in Fig. I.5.

We note that interpolation will likely become a major source of error when the number of available target waveforms is decreased significantly and when the dimensionality of the parameter space increases. We shall return to discussing both issues later in this paper.

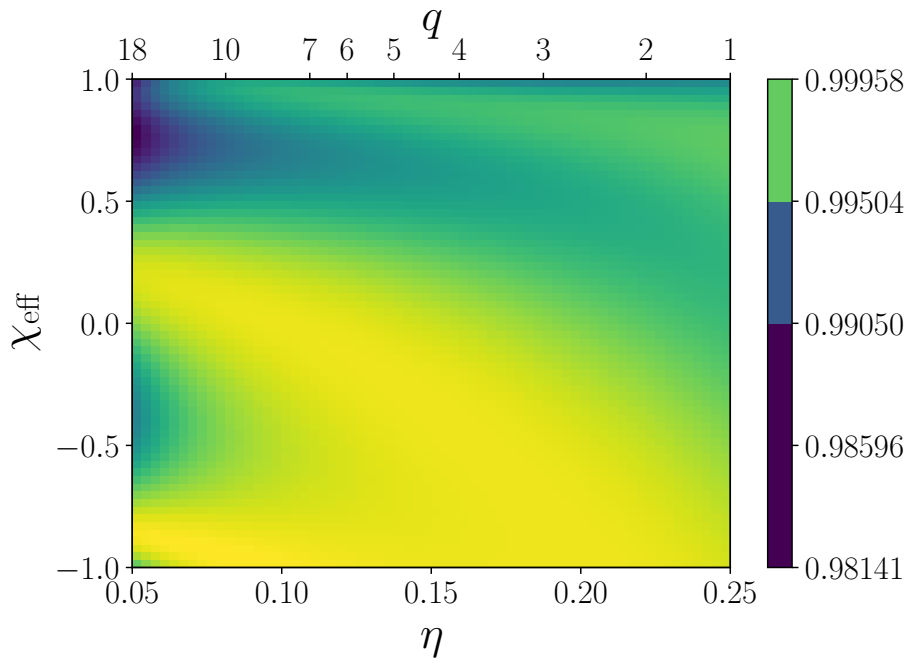

Figure I.4: Matches of EB against PhenomD without interpolation and under flat PSD. In this figure, we generated target model in the same grid as the approximate model, and run our method in full bases (without reduced order). This plot is used as comparison to interpolation and reduced order result as explained in the text.

We have repeated the study with the AZDHP noise curve and find qualitatively the same behaviour. A summary of mismatches (in $\log_{10}$ scale) and improvements are given in Table I.1. We present the minimum, maximum and median mismatches across the dense grid, as well as the improvements defined by (I.19).

Table I.1 shows that overall the difference of mismatches using one or the other noise spectrum is relatively small. Full histograms are shown in Fig. I.6. Because results are so similar, we only show the figures for the flat PSD.

So far, we have generated our target model, PhenomD, on a regular grid in the parameter space as illustrated in Fig. I.1. We also investigate how the choice of positions of target signals affect our result. For that reason, we distribute the same number of PhenomD waveforms randomly, drawn uniformly from the parameter space of η and $\chi_{\rm eff}$. These target waveforms are then projected onto basis vectors coming from the dense regular grid of PhenomB signals. We follow the above procedure to build the EB coefficients and interpolate them onto the dense regular grid to evaluate mismatches between EB and PhenomD waveforms with the same parameters. Since the results for flat and AZDHP PSDs are relatively close, we

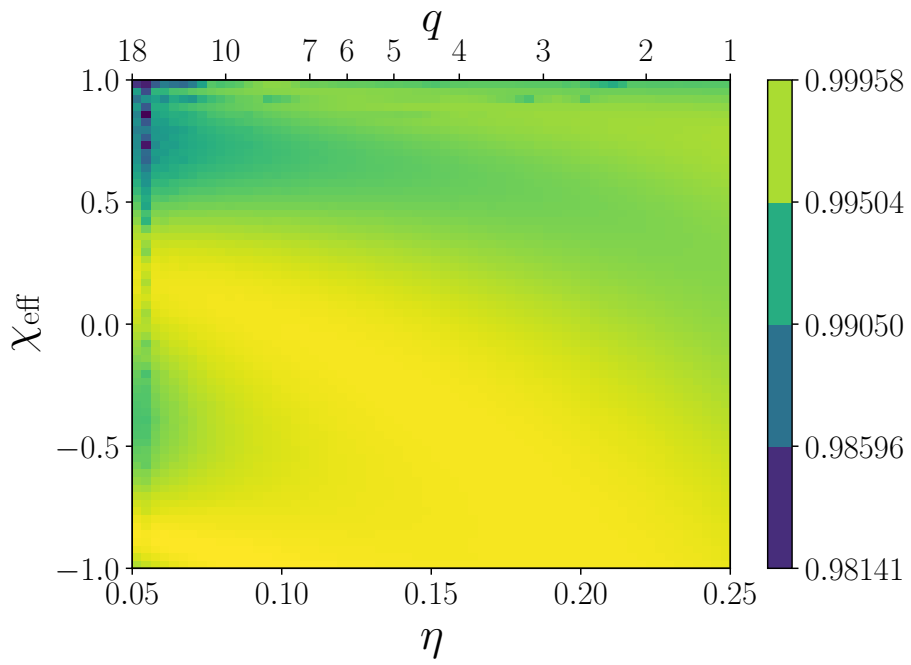

Figure I.5: Matches between EB against PhenomD with interpolation and under flat PSD. In this figure, we generated both target and approximate models in regular grid . The number of target model is about 25% of the approximate model as explained in subsection I. We perform two dimensional interpolation (see subsection I) over the projection coefficients. To make the comparison easier, we set the range of match equal as that on Fig. I.4.

Table I.1: Mismatches between PhenomB and PhenomD as well as mismatches between EB and PhenomD in $\log_{10}$ *scale. The improvement,* $\mathcal{I}$*, is defined by (I.19). Here we compare the results using two different PSDs, flat PSD (*$S_n = 1$*) and AZDHP. We also compare results that interpolate from the sparse to the dense grid with calculations entirely carried out on the dense grid (no interpolation).*

PSD		no interpolation			interpolation		
		min	max	med	min	max	med
Flat	PhenomB	-2.67	-0.001	-0.03			
	EB	-3.37	-1.99	-2.69	-3.38	-1.73	-2.68
	$\mathcal{I}$	1.42	1201	40	1.42	1195	39
AZDHP	PhenomB	-2.50	-0.10	-1.14			
	EB	-3.23	-1.95	-2.71	-3.23	-1.68	-2.71
	$\mathcal{I}$	1.17	1082	39	1.20	1082	39

evaluate the mismatch assuming a flat PSD. We find that $\log_{10}\mathcal{M}$ of random uniform grid ranges between -1.39 and -3.39. For direct comparison, the mismatch of the regular grid of target waveforms is between -1.73 and -3.38 as presented in Table. I.1. From this simple study, we argue that different positions will not affect the result significantly, so long as the number and distribution of parameters are similar.

I.3.1.1 Accuracy of the reduced basis

Here we examine the accuracy of EB when restricting ourselves to the first K bases. The advantage of a reduced basis is mainly to optimize computational power.

Fig. I.7 shows the mismatches and improvements as a function of the number of bases that are kept from the SVD of PhenomB. To obtain the result, we projected $S \approx N/4$ PhenomD signals onto the PhenomB basis and performed interpolation as explained in previous section. For very small numbers of bases we observe a rapid drop in mismatches. After the first 25 bases are included, however, the improvement of EB is much more gradual when more bases are used. We speculate that the most important variations in PhenomB signals are already well described with 25 basis vectors, but we do need a lot more basis vectors to accommodate additional features present in PhenomD that are not captured accurately by PhenomB (most notably, the high mass ratio, high spin regime).

If our goal is that the EB signals are at least as accurate as the approximate model, and in most points of parameter space significantly more accurate, then we find that 3375 of 4225 bases are needed to guarantee that the improvement $\mathcal{I} \geq 1$.

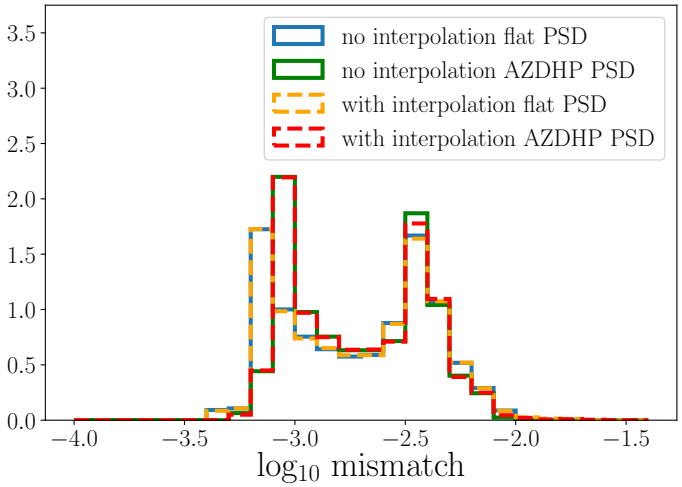

Figure I.6: Mismatches between EB and PhenomD target signals for different configurations and PSDs. The histograms are normalized so that the sum of area under each line are set equal to unity. The dashed lines represent the result using fewer target signals and interpolation, whereas the respective solid lines show results using more target signals and no interpolation (see text).

We might expect that higher parameter-space dimension ($\mathcal{D}$ + 1) require a larger number of bases to obtain at least the same mismatch as lower dimension ($\mathcal{D}$). Naïve intuition would be that the increase of dimensionality in parameter space requires an exponential growth of the basis size. This is called "curse of dimensionality". However, a study by Field et al 2012 [53] shows that one may only need a small number of additional bases in higher dimension to obtain comparable result as in lower dimension. Therefore, the number of reduced bases is not exponentially proportional to the number of dimensions in parameter space. Higher parameter-space dimensions, however, affect computational time as we generate more waveforms covering a greater space.

I.3.1.2 Minimum target waveforms

In the analysis above, we used a uniform grid for target and approximate waveforms with the ratio of PhenomD to PhenomB signals of about $1/4$. In this section, we explore the minimum number of target waveforms needed to obtain a computational efficient EB model that improves the approximate model significantly.

We projected various numbers of target signals given on a sparse, uniform grid with $S = r \times r$ points onto the basis derived from the full N approximate waveforms. We evaluate the improvement $\mathcal{I}$ on the dense grid (after interpolating the

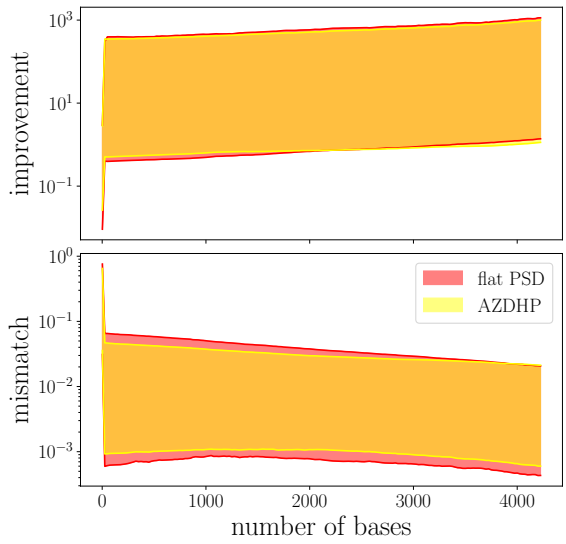

Figure I.7: The accuracy of a reduced-order model. The top plot is the mismatch between EB and PhenomD waveforms as a function of the number of reduced bases. The bottom plot shows the improvement, cf. (I.19). The shaded areas are bounded by the minimum and maximum mismatches. The red area is obtained with a flat PSD while the yellow area uses AZDHP. Results with different PSDs overlap well. From this plot, using the minimum of 3375 bases, we can guarantee that all the EB waveforms are more accurate than their approximate waveforms.

projection coefficients from the sparse onto the dense grid) and show the minimum in Fig. I.8. We find that $12 \times 12 = 144$ target waveforms guarantee that all EB results are better than PhenomB. This number is almost 30 times smaller than the number of PhenomB signals we use, and more than 95% of the signals generated on the dense grid to compute mismatches are now interpolated and have not been used as target waveforms in the construction of EB.

In fact, we find that the EB model built with $S = 144$ accurate PhenomD signals performs in large parts of the parameter space comparable to the previous case of 33×33 target signals. Only the problematic boundary regions that were visible already in Fig. I.5 become more pronounced, both in size and mismatch. Better results, even with this relatively small number of target signals, can be achieved by the iteration procedure we will introduce below.

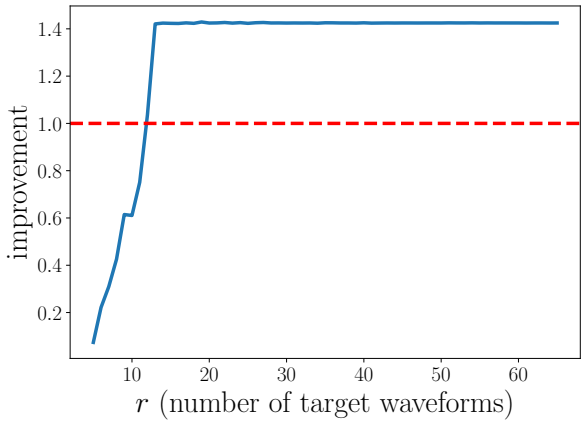

Figure I.8: Only 144 (12 × 12) PhenomD signals on a uniform grid are needed to guarantee that all EB waveforms perform better than PhenomB (assuming flat noise). The blue line is the value of the minimal improvement using r × r target waveforms.

I.3.1.3 Phase and amplitude contributions

In order to identify the dominant contribution to the inaccuracies that we reported for our EB model, we now evaluate mismatches for individual components. In particular, we can apply the definition of the overlap (I.17) and mismatch (I.18) to the amplitude alone, without maximizing over time and phase shifts.

We find that the PhenomB amplitude has relatively high overlap against PhenomD that ranges from 90.78% to 99.98%. As we show in Fig. I.9, the EB amplitude also has extremely small mismatches with the target signal PhenomD. Because the strain mismatches, also included in the figure, are orders of magnitude higher, we conclude that they are dominated by modelling inaccuracies in the phase.

We note that one could in principle calculate mismatches of the pure phase functions as well, but these numbers are less meaningful because they are not invariant under the physical degrees of freedom: phase and time shifts applied to both functions simultaneously. A geometric interpretation relates the overlap to 'the angle' between two functions, but because the phases appear in the complex exponential of the strain, the relevant measure is the phase difference instead of their angle.

I.3.1.4 Mass scaling

So far, we have fixed the total mass of the systems in consideration to $M = 50M_\odot$. This choice is almost irrelevant for the actual waveform construction as vacuum

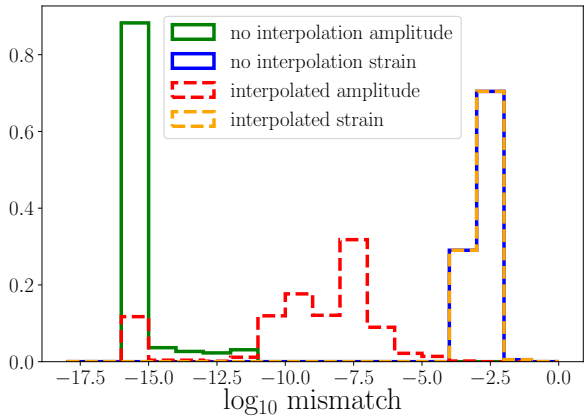

Figure I.9: Normalized histogram of EB amplitude and strain mismatches against PhenomD in flat noise spectrum. The dashed curves are the result from interpolating fewer target signals; the solid line did not employ interpolation (cf. Fig. I.6).

spacetimes include the system's total mass as a simple scaling factor. As a result, the signal models are actually a function of the dimensionless product Mf. This degeneracy between total mass and frequency is broken when we need to consider physical, full-dimension frequencies that enter the AZDHP noise curve. We also specified our lower cutoff frequency as 30 Hz. Hence, scaling the total mass means appropriately setting $f_{\rm low}$ and $f_{\rm high}$.

Binaries with higher total mass merge at lower frequencies. Therefore, as we have constructed a signal model for $M = 50M_\odot$ starting at 30 Hz, we can use the same model also for more massive systems with the same $f_{\rm low}$. The higher mass system then has a shorter frequency range.

Assuming we have carried out the model construction for a total mass M_1, we can scale the frequency of a system with a different total mass M_2, but otherwise the same intrinsic parameters, as follows

$$f_2 = f_1 \left(\frac{M_1}{M_2} \right). \tag{I.20}$$

As a consequence of the Fourier transform, the strain $\tilde{h}(f)$ also needs to be scaled by the total mass. Putting it all together, the strain for M_2 can be obtained through the following relation,

$$\tilde{h}(f; M_2, \eta, \chi_{\rm eff}) = \left(\frac{M_2}{M_1} \right)^2 \tilde{h} \left(\frac{M_2 f}{M_1}; M_1, \eta, \chi_{\rm eff} \right). \tag{I.21}$$

Without reconstructing the EB model, we can evaluate the mismatch between EB and the target model PhenomD in frequency range between $f_{\rm low}$ and $f_{\rm high}$ for

total masses between 50 to 200 $M_\odot$. We assume the AZDHP PSD. The results are shown in Fig I.10. In this plot, we show that the change of mismatches are relatively small for different total masses under the AZDHP noise spectrum. With the same $f_{\rm low}$ (30 Hz) and $f_{\rm high}$ scaled by the total mass as explained above, higher total mass systems produce shorter waveforms. Since the AZDHP noise spectrum is most sensitive in range of early hundred Hz and begin to drop gradually, the agreement between different parts of the waveforms are affected by different sensitivity ranges. Hence the matches are not perfectly uniform for various total masses.

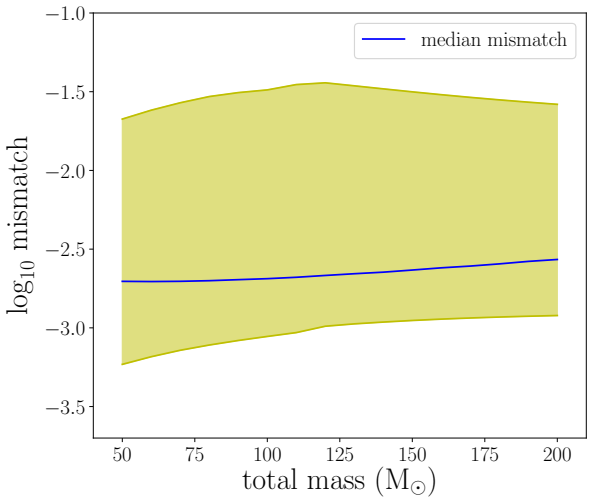

Figure I.10: Mismatches of EB against PhenomD for various total masses as explained in the text. The shaded area is the range of log_{10} mismatch of the respective total masses, and the blue line is its median. This figure compares mass scaling using AZDHP PSD from 30 Hz to f_{high} of the corresponding total mass.

I.3.1.5 SVD iteration

In the previous sections, we found that our method is effective in producing a more accurate waveform model compared to the approximate model we started with, PhenomB. The mismatches of the resulting EB family are better than PhenomB's mismatches against the target model, PhenomD. This section explores a method to iterate the above steps to produce an even more accurate version of EB, using the same number of approximate and target waveforms.

The basic idea is that we can employ the EB model as the *approximate waveform* of the subsequent iteration and derive a basis from N EB signals interpolated

on the dense grid. We then project the same PhenomD signals onto the new basis. We repeat this iterative procedure until the median does not improve significantly.

We first use the minimum number of target waveforms discussed in Sec. I and later compare the results obtained with more target waveforms. We run the SVD iteration using 12×12 PhenomD signals projected onto 65×65 approximate models without reducing the basis. The reported mismatches employ a flat noise spectrum.

The first EB improves upon PhenomB in mismatch between 1.04 and 860 with median of 23.5. This corresponds to $\log_{10}$ mismatches between -3.36 to -3.57. We then use the EB signals to construct a new SVD basis and run the same process iteratively. After 35 iteration the median $\log_{10}$ mismatch of EB decreases to -4.463 while the median improvement raises to 1254. The mismatch and improvement results are shown in Fig. I.11. On a standard laptop, one iteration of this process took about 10 minutes using a single node (no parallelization).

For comparison, we also used PhenomD signals on a 33×33 grid and ran the same iterative process. Using more target waveforms, we achieved a median mismatches below 10^{-6} and an improvement of more than 1750 over PhenomB.

In conclusion, we can reduce the mismatch of EB using an iterative process, but of course this will not be as effective as using more target waveforms.

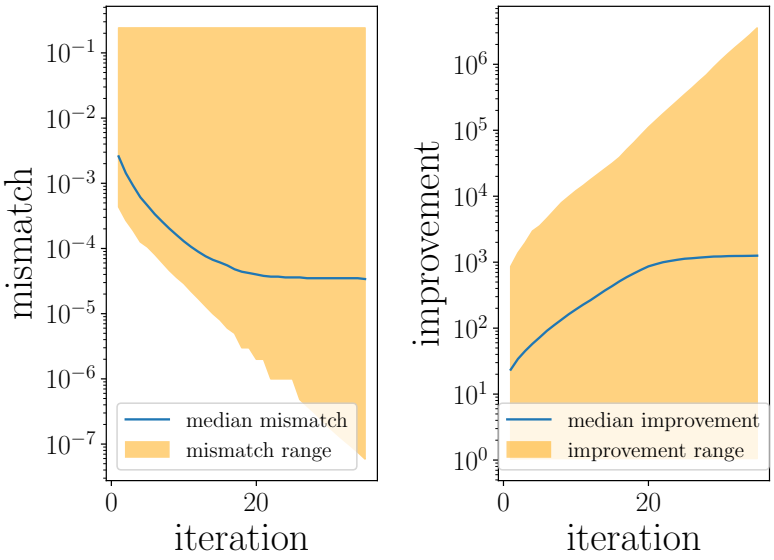

Figure I.11: Mismatches and improvement between EB and PhenomD after iterations. Left: mismatch range over iteration number shown in shaded area with median indicated by the blue curve. Right: improvement range that corresponds to the same iteration is shown in shaded area, where the blue curve shows the median improvement.

I.3.2 Increased dimensionality: two spins

We have shown that our method can successfully be applied to the aligned equal-spin case, in which both the approximate and target waveforms were varied across an effectively two-dimensional space of intrinsic parameters. Here we expand the dimensionality such that the new EB waveforms are built from a *higher-dimensional* target model projected onto a *lower-dimensional* approximate model. We therefore investigate to what extent the basis can represent a greater parameter space than what it originated from.

Although the case we study here is not yet a practical scenario for actual applications, we argue that in principle one should be able to apply this method for future projections of higher dimensional target models onto lower dimensional basis models.

Specifically, here we consider the case where the target waveforms PhenomD vary in η, χ_{1z} and χ_{2z} individually, so that χ_a [see Eq. (I.3) for its definition] does not necessarily vanish. We remind the reader that PhenomD is indeed sensitive to these changes, both in the inspiral and in predicting the ringdown signal of the remnant. In contrast, the approximate model PhenomB only depends on $\chi_{\rm eff}$ and not χ_a, hence we keep generating those signals choosing $\chi_{\rm eff} = \chi_{1z} = \chi_{2z}$. Below we discuss results and challenges of this method.

First, we generate the approximate PhenomB waveforms on the same grid of $N = 65 \times 65$ points in the η-$\chi_{\rm eff}$ parameter space that we used before. See Sec. I for details. Second, we give ourselves $S = 33 \times 33 \times 33 = 35937$ target waveforms on regular grid η, χ_{1z} and χ_{2z}. The parameter ranges are the same as for the approximate signals, except that here $\chi_{1z}, \chi_{2z} \in [-1, 1]$ individually. The procedure we then follow is the same as before. The SVD basis is in fact unchanged compared to what we have used in previous sections, but we now project a much larger number of target signals onto that basis to see if we can accurately represent variations in a parameter that was of no relevance in the approximate model.

Let us emphasize that in this study, we only analyze the errors caused by the projection onto a (lower-dimensional) approximate SVD basis. Therefore, our comparison does not include any interpolation. Instead, we calculate mismatches between PhenomD and either PhenomB or EB on all S points of the parameter space. The results are shown as histograms in Fig. I.12. The $\log_{10}$ mismatches of the EB model range from -1.89 to -3.34 (which corresponds to matches between 0.987 to 0.999). Compared to the two-dimensional, equal-spin case of Sec. I, the matches we find here are slightly lower. This is not surprising, as here we have introduced many more PhenomD waveforms that we know are not accurately captured by PhenomB.

For comparison, we also show the histogram of mismatches between PhenomB and PhenomD in the same Fig. I.12. Evidently, EB achieves a much better

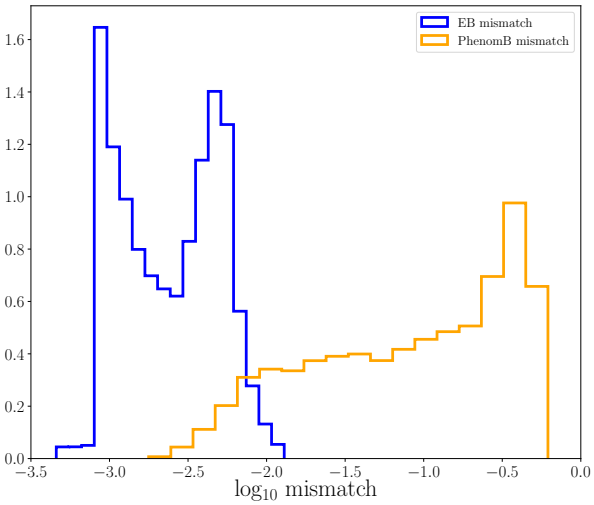

Figure I.12: Normalized histograms of double-spin EB against PhenomD without interpolation, i.e., the EB model was built from $33 \times 33 \times 33$ *PhenomD waveforms projected onto an SVD basis of* 65×65 *PhenomB signals. For comparison, the disagreement between PhenomB and PhenomD is also included.*

accuracy than PhenomB, for which the $\log_{10}$ mismatches range between -2.75 to -0.2 (matches between 0.380 to 0.998). We note that this range is similar to Fig. I.3 that is restricted to the equal-spin case.

For completeness, Fig. I.13 also illustrates the location of the highest mismatches of between PhenomB and PhenomD in the parameter space. In this plot, we show the location of the 50 lowest and 50 highest mismatches. The largest disagreement indeed occurs for high mass ratios and asymmetric spins.

From this study, we conclude that one can in principle project a set of higher-dimensional signals onto a basis derived from a lower-dimensional model. However, interpolating across a high-dimensional parameter space becomes much more challenging, especially if a large number of bases has to be included in the EB model. We leave a detailed analysis and discussion of this problem to future work.

I.4 Conclusions and future perspectives

The development of accurate GW models is a crucial task to support future detections and the correct interpretation of GWs from merging compact objects. With higher detector sensitivity in the upcoming science runs of LIGO and Virgo, more detections are expected, increasing the chance for an unusually loud, or in other ways special, observation that will require more accurate models than ever before.

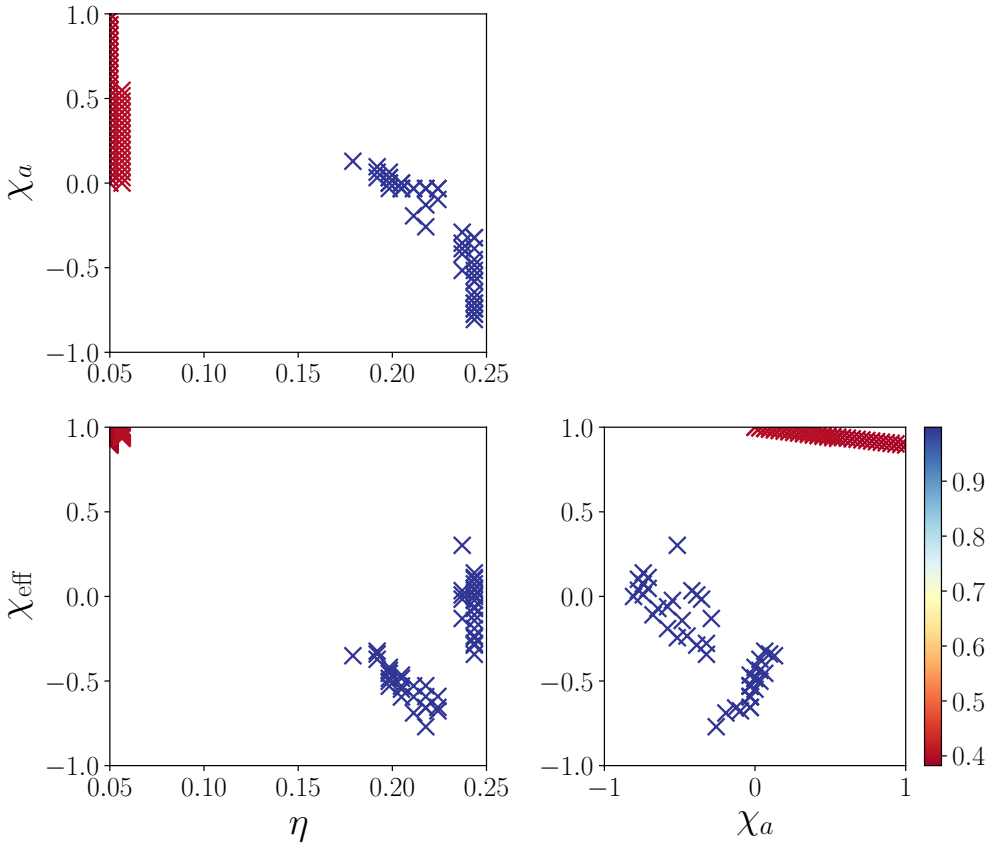

Figure I.13: The location of 50 lowest matches and 50 highest matches of PhenomB against PhenomD. The colorbar shows the match. The matches between the worst and the best waves are coloured white.

Previous work on the development of GW models either targeted a fairly restricted part of the parameter space or required substantial computational as well as human resources. Here we have developed a method to dynamically update an approximate waveform model in a given parameter range. We accomplished this by projecting a set of a more accurate signals onto a larger set of a less accurate waveforms that can be evaluated efficiently and continuously across the parameter space.

We worked in frequency domain and decomposed both waveform models into amplitude and phase that are updated separately. Following earlier studies with a similar goal [35], we employed SVD matrix factorization to split the approximate model's data into two unitary matrices and one diagonal matrix. We used the appropriate unitary matrix as a basis representation of the approximate model, the other two matrices are updated by projecting the accurate model onto that basis. We then interpolated the projection coefficients and combined them with the approximate basis to obtain a new waveform family that we call enriched basis. This model has a higher accuracy than the approximate model and can be evaluated continuously in parameter space.

In this first exploratory study, we restricted ourselves to the non-precessing parameter space of BBHs. We showed that the EB model is considerably more faithful to its target model (PhenomD) than the approximate model (PhenomB) that we employed. This is true both for flat and AZDHP noise spectra. Let us highlight that especially in regions of the parameter space that were not accurately described by the approximate model because it had not been calibrated there, the improvement of EB can be dramatic. This also holds if an extra physical dependence is introduced by the target model that was not present in the approximate model.

There are a number of procedural parameters that can be tuned in this approach to achieve optimal results. Among those, we tested the following.

(A) How many basis vectors need to be kept in the EB model? As expected, we found that very few SVD basis vectors are needed to describe the basic parameter dependence of the approximate model. However, as the success of our updating method relies on accurately representing effects beyond what was included in the approximate model, we also found that a wide parameter space such as the one tested here may require a basis of several thousand vectors. We expect this number to sensitively depend on the size of the parameter space and the accuracy of the approximate model.

(B) How many target signals are required?
In the study presented here, we often used a large number of target signal to first test the efficacy of the basic principle. In Sec. I, we reduced that number systematically and analyzed the result. While the edges of the pa-

rameter space suffer increasingly from interpolation issues when number of target signals was reduced, we found that even a regular grid of 12×12 target signals showed overall satisfactory improvement. We note that this number is larger than the number of NR waveforms that were used to calibrate PhenomD [32, 33] which is not surprising given that more physical insight and intuition went into the original construction while here we test an agnostic, fully automatic approach. We also note that we successfully tested uniform random placement of target waveforms instead of a regular grid, but designing more refined methods of placing target waveforms is an active research topic that can lead to a further reduction of the number of signals required to build an EB model.

(C) Can the process be iterated to achieve better results?
Once a fast and efficient EB model has been built, it can and should be used as an approximate model for the next refinement. While this approach is obvious when more (or different) target waveforms become available, we also showed in Sec. I that such an iterative procedure can further improve the EB when using the same set of target signals again. This might be counter-intuitive as the same target waveforms seem to be projected onto the same N-dimensional space of amplitude and phase functions in each iterative step. However, it turns out that performing a second SVD on EB data re-structures the basis vectors such that the number of irrelevant vectors with vanishingly small σ values increases (i.e., the EB is represented with fewer bases). It is these basis vectors that are not needed to represent the approximate model, but there are useful in each iterative step to slightly change the vector space toward a more faithful representation of the target. Further studies need to show whether such a procedure also introduces more irregularities and interpolation issues that might counter the gain we report here.

Overall, the results we present here are very promising. One important application that we work toward is actually using the best available analytical models as approximate signals and NR data as the target model. In oder for this to be feasible, however, we need to develop additional methods in the immediate future. In particular, the parameter space of most interest include precessing systems, and for those, we eventually need to deal with interpolating over a possibly seven-dimensional parameter space (given by two three-dimensional BH spin vectors and the mass ratio). Interpolating a sparse set of projection coefficients (given by the available NR simulations) may require much more sophisticated interpolation techniques than the ones we have employed here. In fact, we expect interpolation to be the most challenging step in more realistic applications of our procedure.

In addition, a likely scenario where our method could be extremely useful

is when a large parameter space needs to be accessible for a signal model to be useful, but targeted NR simulations only cover a reasonable small portion of that space. In that case, our EB model could be updated only where new information is available. This can be achieved by implementing a more flexible interpolation approach that smoothly bridges coefficients based on the approximate model with information from a targeted and localized set of NR data. Such a "hybrid"[3] approach would allow updating established models locally, and it would complement, for instance, parameter estimation methods that take advantage of models that can be generated for arbitrary sets of parameters [54] and alternative methods that use discrete NR data sets [55, 56].

We intend to develop solutions for the above-described use cases of EB in the near future. Codes will then be fully integrated in existing analysis suites [46] to guarantee direct impact on the analysis of GW observations. We view this as an important step toward further fostering the integration of numerical and analytical modeling techniques in an era of frequent GW observations.

Acknowledgments

The authors would like to thank to Sascha Husa, Lionel London, Harald Pfeiffer, and Mark Hannam for useful discussions related to this work. This work was supported by the Max Planck Society's Independent Research Group Grant. Computations were carried out on the Holodeck cluster of the Max Planck Independent Research Group "Binary Merger Observations and Numerical Relativity."

[3] We emphasize that "hybrids" in GW modeling commonly refer to the combination of analytical inspiral signals with numerical merger data. Here, however, we mean it in the sense that parameter space portions where only an approximate model is available could be smoothly combined with new information localized in certain regions of the parameter space.

Bibliography

[1] Abbott BP, et al. Observation of Gravitational Waves from a Binary Black Hole Merger. Phys Rev Lett. 2016 Feb;116:061102. Available from: https://link.aps.org/doi/10.1103/PhysRevLett.116.061102.

[2] Aasi J, et al. Advanced LIGO. Classical and Quantum Gravity. 2015 March;32:074001. Available from: http://stacks.iop.org/0264-9381/32/i=7/a=074001.

[3] Abbott BP, et al. GW151226: Observation of Gravitational Waves from a 22-Solar-Mass Binary Black Hole Coalescence. Phys Rev Lett. 2016 Jun;116:241103. Available from: https://link.aps.org/doi/10.1103/PhysRevLett.116.241103.

[4] Abbott BP, et al. GW170104: Observation of a 50-Solar-Mass Binary Black Hole Coalescence at Redshift 0.2. Phys Rev Lett. 2017 Jun;118:221101. Available from: https://link.aps.org/doi/10.1103/PhysRevLett.118.221101.

[5] Abbott BP, et al. GW170608: Observation of a 19 Solar-mass Binary Black Hole Coalescence. The Astrophysical Journal Letters. 2017 December;851:L35. Available from: http://stacks.iop.org/2041-8205/851/i=2/a=L35.

[6] Abbott BP, et al. GW170814: A Three-Detector Observation of Gravitational Waves from a Binary Black Hole Coalescence. Phys Rev Lett. 2017 Oct;119:141101. Available from: https://link.aps.org/doi/10.1103/PhysRevLett.119.141101.

[7] Abbott BP, et al. GW170817: Observation of Gravitational Waves from a Binary Neutron Star Inspiral. Phys Rev Lett. 2017;119(16):161101.

[8] Acernese F, et al. Advanced Virgo: a second-generation interferometric gravitational wave detector. Classical and Quantum Gravity. 2014 December;32:024001. Available from: http://stacks.iop.org/0264-9381/32/i=2/a=024001.

[9] Abbott BP, et al. GW150914: First results from the search for binary black hole coalescence with Advanced LIGO. Phys Rev D. 2016 Jun;93:122003. Available from: https://link.aps.org/doi/10.1103/PhysRevD.93.122003.

[10] Finn LS, Chernoff DF. Observing binary inspiral in gravitational radiation: One interferometer. Phys Rev D. 1993 Mar;47:2198–2219. Available from: https://link.aps.org/doi/10.1103/PhysRevD.47.2198.

[11] Blanchet L, Detweiler S, Le Tiec A, Whiting BF. Post-Newtonian and numerical calculations of the gravitational self-force for circular orbits in the Schwarzschild geometry. Phys Rev D. 2010 Mar;81:064004. Available from: https://link.aps.org/doi/10.1103/PhysRevD.81.064004.

[12] Blanchet L. Gravitational Radiation from Post-Newtonian Sources and Inspiralling Compact Binaries. Living Reviews in Relativity. 2014 Feb;17:2. Available from: https://doi.org/10.12942/lrr-2014-2.

[13] Baumgarte T, Shapiro S. Numerical Relativity: Solving Einstein's Equations on the Computer. vol. 1 of 10. 3rd ed. The Edinburgh Building, Cambridge CB2 8RU, UK: Cambridge University Press; 2010.

[14] Mroué AH, et al. Catalog of 174 Binary Black Hole Simulations for Gravitational Wave Astronomy. Phys Rev Lett. 2013 Dec;111:241104. Available from: https://link.aps.org/doi/10.1103/PhysRevLett.111.241104.

[15] Ajith P, Buchman LT, Chu T, Reisswig C, Santamaría L, Scheel MA, et al. The NINJA-2 catalog of hybrid post-Newtonian/numerical-relativity waveforms for non-precessing black-hole binaries. Class Quant Grav. 2012;29:124001. [Erratum: Class. Quant. Grav.30,199401(2013)].

[16] Pekowsky L, O'Shaughnessy R, Healy J, Shoemaker D. Comparing gravitational waves from nonprecessing and precessing black hole binaries in the corotating frame. Phys Rev D. 2013 Jul;88:024040. Available from: https://link.aps.org/doi/10.1103/PhysRevD.88.024040.

[17] Hinder I, et al. Error-analysis and comparison to analytical models of numerical waveforms produced by the NRAR Collaboration. Classical and Quantum Gravity. 2013;31(2):025012. Available from: http://stacks.iop.org/0264-9381/31/i=2/a=025012.

[18] Hannam M, Husa S, González JA, Sperhake U, Brügmann B. Where post-Newtonian and numerical-relativity waveforms meet. Phys Rev D. 2008 Feb;77:044020. Available from: https://link.aps.org/doi/10.1103/PhysRevD.77.044020.

[19] Hannam M, Husa S, Brügmann B, Gopakumar A. Comparison between numerical-relativity and post-Newtonian waveforms from spinning binaries:

The orbital hang-up case. Phys Rev D. 2008 Nov;78:104007. Available from: https://link.aps.org/doi/10.1103/PhysRevD.78.104007.

[20] Buonanno A, Damour T. Effective one-body approach to general relativistic two-body dynamics. Phys Rev D. 1999 Mar;59:084006. Available from: https://link.aps.org/doi/10.1103/PhysRevD.59.084006.

[21] Buonanno A, Pan Y, Pfeiffer HP, Scheel MA, Buchman LT, Kidder LE. Effective-one-body waveforms calibrated to numerical relativity simulations: Coalescence of nonspinning, equal-mass black holes. Phys Rev D. 2009 Jun;79:124028. Available from: https://link.aps.org/doi/10.1103/PhysRevD.79.124028.

[22] Damour T, Nagar A. Comparing effective-one-body gravitational waveforms to accurate numerical data. Phys Rev D. 2008 Jan;77:024043. Available from: https://link.aps.org/doi/10.1103/PhysRevD.77.024043.

[23] Pan Y, Buonanno A, Buchman LT, Chu T, Kidder LE, Pfeiffer HP, et al. Effective-one-body waveforms calibrated to numerical relativity simulations: Coalescence of nonprecessing, spinning, equal-mass black holes. Phys Rev D. 2010 Apr;81:084041. Available from: https://link.aps.org/doi/10.1103/PhysRevD.81.084041.

[24] Pan Y, Buonanno A, Boyle M, Buchman LT, Kidder LE, Pfeiffer HP, et al. Inspiral-merger-ringdown multipolar waveforms of nonspinning black-hole binaries using the effective-one-body formalism. Phys Rev D. 2011 Dec;84:124052. Available from: https://link.aps.org/doi/10.1103/PhysRevD.84.124052.

[25] Damour T, Nagar A, Bernuzzi S. Improved effective-one-body description of coalescing nonspinning black-hole binaries and its numerical-relativity completion. Phys Rev D. 2013 Apr;87:084035. Available from: https://link.aps.org/doi/10.1103/PhysRevD.87.084035.

[26] Taracchini A, Pan Y, Buonanno A, Barausse E, Boyle M, Chu T, et al. Prototype effective-one-body model for nonprecessing spinning inspiral-merger-ringdown waveforms. Phys Rev D. 2012 Jul;86:024011. Available from: https://link.aps.org/doi/10.1103/PhysRevD.86.024011.

[27] Pan Y, Buonanno A, Taracchini A, Boyle M, Kidder LE, Mroué AH, et al. Stability of nonspinning effective-one-body model in approximating two-body dynamics and gravitational-wave emission. Phys Rev D. 2014 Mar;89:061501. Available from: https://link.aps.org/doi/10.1103/PhysRevD.89.061501.

[28] Blackman J, et al. Numerical relativity waveform surrogate model for generically precessing binary black hole mergers. Phys Rev D. 2017 Jul;96:024058. Available from: https://link.aps.org/doi/10.1103/PhysRevD.96.024058.

[29] Blackman J, et al. A Surrogate model of gravitational waveforms from numerical relativity simulations of precessing binary black hole mergers. Phys Rev D. 2017 May;95:104023. Available from: https://link.aps.org/doi/10.1103/PhysRevD.95.104023.

[30] Blackman J, Field SE, Galley CR, Szilágyi B, Scheel MA, Tiglio M, et al. Fast and Accurate Prediction of Numerical Relativity Waveforms from Binary Black Hole Coalescences Using Surrogate Models. Phys Rev Lett. 2015 Sep;115:121102. Available from: https://link.aps.org/doi/10.1103/PhysRevLett.115.121102.

[31] Ajith P, Hannam M, Husa S, Chen Y, Brügmann B, Dorband N, et al. Inspiral-Merger-Ringdown Waveforms for Black-Hole Binaries with Nonprecessing Spins. Phys Rev Lett. 2011 Jun;106:241101. Available from: https://link.aps.org/doi/10.1103/PhysRevLett.106.241101.

[32] Husa S, et al. Frequency-domain gravitational waves from nonprecessing black-hole binaries. I. New numerical waveforms and anatomy of the signal. Phys Rev D. 2016 Feb;93:044006. Available from: https://link.aps.org/doi/10.1103/PhysRevD.93.044006.

[33] Khan S, Husa S, Hannam M, Ohme F, Pürrer M, Forteza XJ, et al. Frequency-domain gravitational waves from nonprecessing black-hole binaries. II. A phenomenological model for the advanced detector era. Phys Rev D. 2016 Feb;93:044007. Available from: https://link.aps.org/doi/10.1103/PhysRevD.93.044007.

[34] Cannon K, Chapman A, Hanna C, Keppel D, Searle AC, Weinstein AJ. Singular value decomposition applied to compact binary coalescence gravitational-wave signals. Phys Rev D. 2010 Aug;82:044025. Available from: https://link.aps.org/doi/10.1103/PhysRevD.82.044025.

[35] Cannon K, et al. Interpolation in waveform space: Enhancing the accuracy of gravitational waveform families using numerical relativity. Phys Rev D. 2013 Feb;87:044008. Available from: https://link.aps.org/doi/10.1103/PhysRevD.87.044008.

[36] Cannon K, et al. Efficiently enclosing the compact binary parameter space by singular-value decomposition. Phys Rev D. 2011 Oct;84:084003. Available from: https://link.aps.org/doi/10.1103/PhysRevD.84.084003.

[37] Pürrer M. Frequency-domain reduced order models for gravitational waves from aligned-spin compact binaries. Classical and Quantum Gravity. 2014 September;31:195010. Available from: http://iopscience.iop.org/article/10.1088/0264-9381/31/19/195010/pdf.

[38] Pürrer M. Frequency domain reduced order model of aligned-spin effective-one-body waveforms with generic mass-ratios and spins. Phys Rev. 2016;D93(6):064041.

[39] Ajith P, et al. Phenomenological template family for black-hole coalescence waveforms. Class Quant Grav. 2007;24:S689–S700.

[40] Ajith P, et al. A Template bank for gravitational waveforms from coalescing binary black holes. I. Non-spinning binaries. Phys Rev. 2008;D77:104017. [Erratum: Phys. Rev.D79,129901(2009)].

[41] Santamaría L, Ohme F, Ajith P, Brügmann B, Dorband N, Hannam M, et al. Matching post-Newtonian and numerical relativity waveforms: Systematic errors and a new phenomenological model for nonprecessing black hole binaries. Phys Rev D. 2010 Sep;82:064016. Available from: https://link.aps.org/doi/10.1103/PhysRevD.82.064016.

[42] Hannam M, Schmidt P, Bohé A, Haegel L, Husa S, Ohme F, et al. Simple Model of Complete Precessing Black-Hole-Binary Gravitational Waveforms. Phys Rev Lett. 2014;113(15):151101.

[43] ;. http://www.black-holes.org/waveforms. Available from: http://www.black-holes.org/waveforms.

[44] Brügmann B, González JA, Hannam M, Husa S, Sperhake U, Tichy W. Calibration of moving puncture simulations. Phys Rev D. 2008 Jan;77:024027. Available from: https://link.aps.org/doi/10.1103/PhysRevD.77.024027.

[45] Husa S, González JA, Hannam M, Brügmann B, Sperhake U. Reducing phase error in long numerical binary black hole evolutions with sixth-order finite differencing. Classical and Quantum Gravity. 2008;25(10):105006. Available from: http://stacks.iop.org/0264-9381/25/i=10/a=105006.

[46] ;. https://wiki.ligo.org/DASWG/LALSuite. Available from: https://wiki.ligo.org/DASWG/LALSuite.

[47] Field SE, Galley CR, Herrmann F, Hesthaven JS, Ochsner E, Tiglio M. Reduced Basis Catalogs for Gravitational Wave Templates. Phys Rev Lett. 2011 Jun;106:221102. Available from: https://link.aps.org/doi/10.1103/PhysRevLett.106.221102.

[48] Smith R, Field SE, Blackburn K, Haster CJ, Pürrer M, Raymond V, et al. Fast and accurate inference on gravitational waves from precessing compact binaries. Phys Rev D. 2016 Aug;94:044031. Available from: https://link.aps.org/doi/10.1103/PhysRevD.94.044031.

[49] Pürrer M. Frequency domain reduced order model of aligned-spin effective-one-body waveforms with generic mass ratios and spins. Phys Rev D. 2016 Mar;93:064041. Available from: https://link.aps.org/doi/10.1103/PhysRevD.93.064041.

[50] Galassi M, Davies J, J T, Gough B, Jungman G, Alken P, et al. GNU Scientific Library: Reference Manual . 3rd ed. United Kingdom: Network Theory Limited; 2009.

[51] Doctor Z, Farr B, Holz DE, Pürrer M. Statistical gravitational waveform models: What to simulate next? Phys Rev D. 2017 Dec;96:123011. Available from: https://link.aps.org/doi/10.1103/PhysRevD.96.123011.

[52] ;. https://dcc.ligo.org/LIGO-P1200087/public. Available from: https://dcc.ligo.org/LIGO-P1200087/public.

[53] Field SE, Galley CR, Ochsner E. Towards beating the curse of dimensionality for gravitational waves using reduced basis. Phys Rev D. 2012 Oct;86:084046. Available from: https://link.aps.org/doi/10.1103/PhysRevD.86.084046.

[54] Veitch J, Raymond V, Farr B, Farr W, Graff P, Vitale S, et al. Parameter estimation for compact binaries with ground-based gravitational-wave observations using the LALInference software library. Phys Rev D. 2015 Feb;91:042003. Available from: https://link.aps.org/doi/10.1103/PhysRevD.91.042003.

[55] O'Shaughnessy R, Blackman J, Field SE. An architecture for efficient gravitational wave parameter estimation with multimodal linear surrogate models. Classical and Quantum Gravity. 2017;34(14):144002. Available from: http://stacks.iop.org/0264-9381/34/i=14/a=144002.

[56] Pankow C, Brady P, Ochsner E, O'Shaughnessy R. Novel scheme for rapid parallel parameter estimation of gravitational waves from compact binary coalescences. Phys Rev D. 2015 Jul;92:023002. Available from: https://link.aps.org/doi/10.1103/PhysRevD.92.023002.

II

Regression methods in waveform modeling: a comparative study

Yoshinta Setyawati[1,2], Michael Pürrer[3], Frank Ohme[1,2]

[1]Max Planck Institute for Gravitational Physics (Albert Einstein Institute), Callinstr. 38, 30167 Hannover, Germany
[2]Leibniz Universität Hannover, 30167 Hannover, Germany
[3]Max Planck Institute for Gravitational Physics (Albert Einstein Institute), D-14476 Potsdam-Golm, Germany

Abstract

Theoretical gravitational-wave models of compact-binary mergers need to be accurate, but also fast in order to compare millions of signals in near real time with experimental data. Various regression and interpolation techniques have been employed to build efficient waveform models, but no study has systematically compared the performance of these methods yet. Here we provide such a comparison. For analytical binary-black-hole waveforms, assuming either aligned or precessing spins, we compare the accuracy as well as the computational speed of a variety of regression methods, ranging from traditional interpolation to machine-learning techniques. We find that most methods are reasonably accurate, but efficiency considerations favour in many cases the simpler approaches. We con-

clude that sophisticated regression methods are not necessarily needed in standard gravitational-wave modeling applications, although machine-learning techniques might be more suitable for problems with higher complexity than what is tested here.

Author's contribution

YS contributed to the presented idea motivated by the ROM workshop in 2018. Following the discussion with FO and MP, YS shaped the study and performed most computational work. MP wrote some of the computational codes and FO supervised the findings of this work. Furthermore, YS wrote most part of the manuscript.

Copyright Notice

II.1 Introduction

The laser interferometer and GW detectors LIGO [1] and Virgo [2] have reported observations of one BNS and ten BBH mergers in their first two observing runs [3]. In the third observing run (O3), we expect to observe several tens of signals from compact binary coalescences [4]. The analysis of these GW data is the motivation for our study. The data from the interferometers are filtered with many theoretically predicted waveforms with varying binary parameters. These waveform templates are drawn from models of the emitted GWs. The waveform models need to fulfil accuracy and speed requirements so that the parameters of the GW source can be estimated well in a reasonable amount of time.

We highlight two major modeling approaches: analytical and NR. The basis of analytical models is the PN expansion [5]. Waveform models in this category are fairly computationally efficient, but the PN approximation breaks down for merger and ringdown part of the signal. The second category is NR. NR waveforms are built by numerically solving Einstein's equations [6, 7, 8]. Although these waveforms are known to have exceptional accuracy to model the correct GW signals in General Relativity, they require high computational resources and need weeks to months to generate.

Combining the two approaches above, new methods have been developed to model full waveforms. Two major families in this group, namely the EOB [9, 10, 11, 12] and the *phenomenological* models [13, 14, 15, 16, 17, 18] are commonly used in GW analyses. In general, these models start from a reformulation of PN results and calibrate the model to a select number of NR simulations. In this study, we employ `SEOBNRv3` [11] and `IMRPhenomPv2` [17, 18] as two representative models that have been widely used to explore the full parameter space of non-eccentric, precessing BBHs.

Over the past few years, complementary techniques have been developed to build fast surrogates of EOB models and NR waveforms with a much higher computational efficiency. Unlike the previous approaches, these models do not start from PN expansions. They use existing EOB or NR waveforms, decompose, and interpolate them. The NRSurrogate models [19, 20, 21, 22, 12, 23, 24] have an exceptional accuracy against the original NR signals, but are more limited in the parameter range and waveform length they cover. Reduced order and surrogate models of EOB waveforms have been crucial to allow EOB models to be used for template bank construction [25] and parameter estimation [26, 27].

In a similar spirit, unique methods have been explored to speed up the waveform generation without compromising accuracy [28, 29, 30, 31, 32]. They have shown that advanced mathematical, statistical, and computational techniques are needed to build waveform models optimized for the demands of GW analyses.

We stress that in order to make a relatively small number of computationally expensive waveforms usable for analysis applications that rely on the ability to freely vary all parameters, all waveform models described above crucially rely on some form of *interpolation* or fitting method as part of their construction. Phenomenological and EOB models typically fit free coefficients (often representing unknown, higher-order PN contributions) to a set of NR data. The fits or interpolants are then evaluated over the binary parameter space. Other approaches, such as NR or EOB surrogate models, rely more on data-driven techniques to interpolate the key quantities needed to reconstruct waveforms anywhere in a given parameter-space region. In fact, the interpolation techniques that have recently been employed cover standard methods such as polynomial fits [16, 12, 33], linear interpolation [34, 30], and more complex method such as GPR [21, 32]. Additionally, novel interpolation methods have been developed such as GMVP [31, 29] and TPI [24, 23].

In this study, we investigate the importance of interpolation and fits in waveform models (which themselves are crucial for GW astronomy), given the accuracy and computational time of various regression methods. We study whether the use of more complicated methods to model the waveforms given the same data preparation and noise reduction is justified in practice. Finally, we compare the performance of machine learning against various traditional methods. In particular, we explore the prospects of ANN as a regression method [35, 36] that has not been widely employed in waveform modeling so far. We focus on BBH systems with spins either aligned with the orbital angular momentum or precessing and provide both theoretical overviews and references to practical tools such as *ready-to-use* algorithms. Our analysis is not only of relevance for current LIGO and Virgo data and their extensions such as the Advanced LIGO A+, Voyager [37], and KAGRA [38], but also for future analysis of GW data by LISA [39] and the third generation instruments such as Einstein Telescope [40] and Cosmic Explorer [41].

The testbed we use is as follows. We compare various methods on waveform data at a fixed point in time as a function of mass ratios and spins. We use two models to generate waveform data: the time-domain model `SEOBNRv3` [11], and the inverse Fourier transform of `IMRPhenomPv2` [17, 18] which is natively given in the frequency domain. Both models were designed for precessing BBH mergers which are described by seven intrinsic parameters: the mass ratio q and the two spin vectors $\vec{\chi}_1$ and $\vec{\chi}_2$ with Cartesian components in the x, y, z directions. `IMRPhenomPv2` models precessing waveforms in a single spin approximation using an effective precession spin parameter.

We consider two classes of training data:

1. Data on a regular three-dimensional grid describing nonprecessing binaries,

$(q, \chi_{1z}, \chi_{2z})$, where $1 \leq q \leq 10$ and $|\chi_{iz}| \leq 1$ for $i = 1, 2$.

2. Random uniform data on a full seven-dimensional grid ($q, \vec{\chi}_1$ and $\vec{\chi}_2$), where $1 \leq q \leq 2$ and $-1/\sqrt{3} \leq \vec{\chi}_i \leq 1/\sqrt{3}$ for $i = 1, 2$.

For each case, the regression methods were tested over test sets made up from random uniform test points that were drawn independently of the training set, but covering the same physical domain.

This paper is organized as follows. We prepare the data by defining the waveform and its reference frame and defining waveform data pieces in a precession adapted frame as discussed more detail in sec. II. We explain the background and the features of traditional methods such as linear interpolation, TPI, polynomial fit, GMVP, and RBF as well as machine learning methods, GPR and ANN in section II. In section II we present the results of our study. Finally, a brief conclusion and discussion of future studies are found in section II. Throughout the manuscript, we employ geometric units with the convention $G = c = 1$.

II.2 Method

II.2.1 Waveform data

We generate training and test waveform datasets for various regression methods from two state-of-the art models of the GWs emitted by merging BBHs. We use the phenomenological model `IMRPhenomPv2` [18, 14, 16] and the effective-one-body model `SEOBNRv3` [42, 43, 11]. `IMRPhenomPv2` includes an effective treatment of precession effects, while `SEOBNRv3` incorporates the full two-spin precession dynamics. The models have been independently tuned in the aligned-spin sector to NR simulations.

The GW strain can be written as an expansion into spin-weighted spherical harmonic modes in the inertial frame

$$h(t; \vec{\lambda}; \theta, \phi) = \sum_{\ell=2}^{\infty} \sum_{m=-\ell}^{\ell} h_{\mathrm{i}}^{\ell,m}(t; \vec{\lambda})_{-2}Y_{\ell,m}(\theta, \phi). \tag{II.1}$$

We can choose to model the waveform modes $h_{\mathrm{i}}^{\ell,m}(t; \theta)$ directly which depend a collection of parameters $\vec{\lambda}$. The spherical harmonics ${}_{-2}Y_{\ell,m}(\theta, \phi)$ for a given (ℓ, m) depend on the direction of emission described by the polar and azimuthal angles θ and ϕ. The two waveform models employed in this study provide approximations to the dominant modes at $\ell = 2$. In a precession adapted frame `SEOBNRv3` includes $m = \pm 2$ and $m = \pm 1$ modes (the negative m modes by symmetry), whereas `IMRPhenomPv2` includes only the $m = \pm 2$ modes. For `SEOBNRv3` we directly

generate time-domain inertial modes $h_{\rm i}^{2,m}(t)$, while for `IMRPhenomPv2` we compute the native inertial modes in the Fourier domain $\tilde{h}_{\rm i}^{2,m}(f)$, and subsequently condition and inverse Fourier transform them to obtain an approximation to the time-domain modes.

To test interpolation methods we work in the setting of the empirical interpolation (EI) method [20, 28]. In this approach we can define an *empirical interpolant* of waveform data piece $X(t;\vec{\lambda})$ (such as, e.g., amplitude or phase of the gravitational waveform) by

$$I_N[X](t;\vec{\lambda}) = \sum_{i=1}^{N} c_i(\vec{\lambda}) e^i(t) = \sum_{j=1}^{N} X(T_j;\vec{\lambda}) b^j(t). \tag{II.2}$$

The first expression is an expansion with coefficients c_i of waveform data in an orthonormal linear basis $\{e^i(t)\}_{i=1}^N$ (e.g. obtained from computing the singular value decomposition [44, 45] for discrete data [23, 24]). A transformation to the basis $\{b^i(t)\}$ allows to have coefficients which are the waveform data piece X evaluated at empirical node times T_j. The EI basis $\{b^i(t)\}$ and the EI times can be obtained by solving a linear system of equations as discussed in [28]. Here we forgo the basis construction step and just choose EI times manually to select waveform data for accessing regression methods.

To simulate the process of building an efficient model we want to transform the inertial frame modes into a more appropriate form, such that data pieces are as simple and non-oscillatory as possible in time and smooth in their parameter dependence on $\vec{\lambda}$. In evaluating the model, we reconstruct the full waveforms by transforming back to the inertial frame. This transformation includes the choice of a precession adapted frame of reference that follows the motion of the orbital plane of the binary. In this frame the waveform modes have a simple structure and are well approximated by non-precessing waveforms. A further simplification in the modes can be achieved by taking out the orbital motion. In addition, we align the waveform and frame following [20] at the same time for different configurations and waveform models. The procedure is comprised of the following steps:[1]

- We define time relative to the peak of the sum of squares of the inertial frame modes.
- We transform the inertial frame waveform modes $h_{\rm i}^{\ell,m}(t)$ (dropping the parameter dependence on $\vec{\lambda}$ for now) to the minimally rotating co-precessing

[1] We represent rotations through unit quaternions. Quaternions can be notated as a scalar plus a vector $\mathbf{Q} = q_0 + \mathbf{q} = (q_0, q_1, q_2, q_3)$. A unit quaternion $\mathbf{R} = e^{\theta\hat{\mathbf{u}}/2}$ generates a rotation through the angle θ about the axis $\hat{\mathbf{u}}$. For calculations we use the `GWFrames` [46, 47] package and notation conventions from [46].

frame [48] and thereby obtain the co-precessing waveform modes

$$h^{2,m}_{\rm copr}(t) = \sum_{m'} h^{2,m}_{\rm i}(t) \mathcal{D}^{2}_{m',m}\left(\mathbf{R}_{\rm copr}(t)\right), \tag{II.3}$$

where $\mathcal{D}^{\ell}_{m',m}$ are Wigner matrices [49, 46] and $\mathbf{R}_{\rm copr}(t)$ is the time-dependent unit quaternion which describes the motion of this frame.

- We compute the Newtonian orbital angular momentum unit vector $\hat{\mathbf{l}}_N(t) = \mathbf{R}_{\rm copr}(t)\,\hat{\mathbf{z}}\,\mathbf{R}^{*}_{\rm copr}(t)$, where $\mathbf{Q}^{*}$ is the conjugate of the quaternion $\mathbf{Q}$ and $\hat{\mathbf{z}} = (0,0,1)$. We interpolate $\hat{\mathbf{l}}_N(t)$ to the desired alignement time $t_{\rm align}$.

- We use the rotor $\mathbf{R_a} = \sqrt{-\hat{\mathbf{l}}_N(t_{\rm align})\,\hat{\mathbf{z}}}$ that rotates $\hat{\mathbf{z}}$ into $\hat{\mathbf{l}}_{\mathbf{N}}(t_{\rm align})$ to align the inertial modes at $t_{\rm align}$ and then compute the aligned co-precessing frame modes $\bar{h}^{2,m}_{\rm copr}(t)$ and quaternion time series $\bar{\mathbf{R}}_{\rm copr}(t)$, where the bar indicates alignment in time.

- Finally, we rotate around the z-axis to make the phases of the $(2,2)$ and $(2,-2)$ modes small by applying a fixed Wigner rotation with the rotor $\mathbf{R_z} = \exp(\theta/2\,\hat{\mathbf{z}})\,\bar{\mathbf{R}}_{\rm copr}$ to obtain $\bar{\bar{h}}^{2,m}_{\rm i}(t)$ and $\bar{\bar{h}}^{2,m}_{\rm copr}(t)$.

We choose the following quantities to test the accuracy and efficiency of interpolation methods: (i) the "orbital phase" defined as one quarter the averaged GW-phase from the $(\ell, m) = (2,2)$ and $(2,-2)$ modes in the co-precessing frame

$$\phi(t) := \frac{1}{4}\left(\arg\left[\bar{\bar{h}}^{2,-2}_{\rm copr}(t)\right] - \arg\left[\bar{\bar{h}}^{2,2}_{\rm copr}(t)\right]\right), \tag{II.4}$$

(ii) a linear combination of the $\ell = m = 2$ modes in the co-orbital frame

$$A(t) := \mathrm{Re}\,\bar{\bar{h}}^{2,2}_{+} = \frac{1}{2}\mathrm{Re}\,\left(\bar{\bar{h}}^{2,2}_{\rm coorb}(t) + \bar{\bar{h}}^{2,-2^{*}}_{\rm coorb}(t)\right), \tag{II.5}$$

where the co-orbital modes are defined as

$$h^{\ell,m}_{\rm coorb}(t) = h^{\ell,m}_{\rm copr}(t) e^{im\phi(t)}. \tag{II.6}$$

The rationale for choosing these two quantities is the following: the phasing is usually the quantity that requires the most care in GW-modeling with accuracy requirements of a fraction of a radian over hundreds of waveform cycles. The co-orbital frame mode combinations play the role of a generalized amplitude and are typically smooth and non-oscillatory.

We consider the following waveform training datasets in this study: (i) Three-dimensional datasets: Several interpolation methods we consider in this study

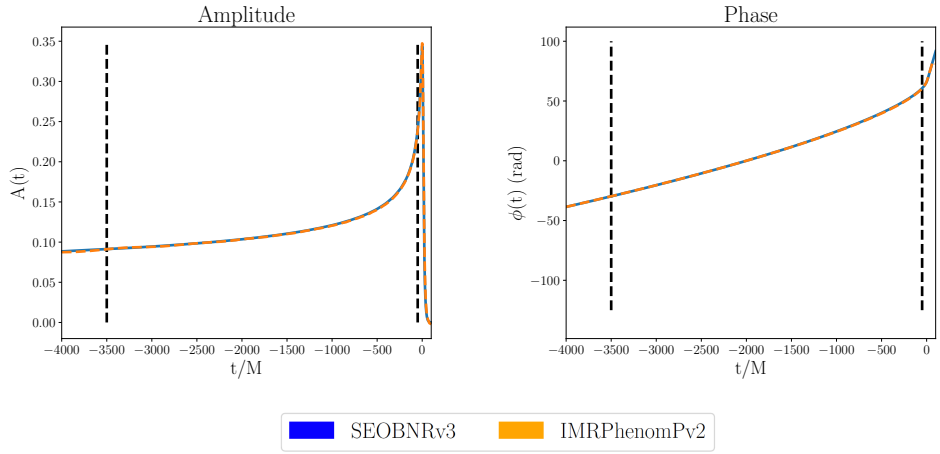

Figure II.1: The key quantities of the GW signal of a precessing BBH, here illustrated for a binary with $(q,\chi_{1x},\chi_{1y},\chi_{1z},\chi_{2x},\chi_{2y},\chi_{2z}) = (1.99, 0.51, 0.04, 0.03, 0.01, 0.6, 0.1)$. *Left: the dimensionless amplitude* $A(t)$. *Right: the phase* $\phi(t)$ *(in unit radian). The black dashed lines show the points in time-space, where we perform different interpolation methods (t=-3500M and t=-50M).*

require data on a regular grid. We prepare three-dimensional datasets (q,χ_{1z},χ_{2z}) in the mass-ratio $q = m_1/m_2$ and the aligned component spins $\chi_{iz} = \vec{S}_i \cdot \hat{L}_N/m_i^2$ for $i = 1, 2$. We do not include the total mass since it can be factored out from the waveform for GWs emitted from BBHs which are solutions of Einstein's equations in vacuum. The grids have an equal number of points per dimension, ranging from 5 to 11. We choose parameter ranges $1 \leq q \leq 10$ and $|\chi_{iz}| \leq 1$. (ii) The full intrinsic parameter space we consider is seven-dimensional: we include the dimensionless spin vector of each black hole $\chi_i = S_i/m_i^2$ and the mass-ratio q of the binary. Due to the *curse of dimensionality* regular grid methods require a prohibitive amount of data in 7D. For instance, ten points per dimension would require 10^7 waveform evaluations. Therefore, we only produce scattered waveform data in seven dimensions which are drawn from a random uniform distribution in each parameter. Here we choose parameter ranges $1 \leq q \leq 2$ and $-1/\sqrt{3} \leq \vec{\chi}_i \leq 1/\sqrt{3}$. For both choices of dimensionality we also generate test data of 2500 points drawn randomly from the respective parameter space.

Waveform data in three and seven dimensions is produced at a total mass of $M = 50M_\odot$ with a starting frequency of 20Hz. We align the waveform and frames at $t_{\rm align} = -2000M$ with the above procedure. We record waveform data from the key quantities at two different times, $t_{\rm target} = -3500M$ and $-50M$, where we have performed alignment in time such that the mode sum of the waveform amplitudes peaks at $t = 0M$. This choice allows us to independently probe the inspiral and

the merger regime. We expect that the waveform data will be very smooth in the inspiral, but more irregular close to merger due to the calibration of internal model parameters to numerical relativity waveforms at a limited number of points in parameter space.

II.2.2 Regression methods: a general overview

A large number of techniques have been developed to improve the speed and accuracy of generating gravitational waveforms. A priori, one would expect that higher speed would go hand-in-hand with less accuracy and less complexity. One frequent question is how to select a method for a specific purpose. Depending on the goals, a choice needs to be made between complex, highly accurate methods with moderate efficiency versus simpler but more efficient methods, and we can choose to trade accuracy for speed.

In this subsection, we discuss various methods and categorize them into two groups. The first group is comprised of traditional interpolation and fitting methods which are based on mathematical techniques and algorithms that are straightforward to implement and easily evaluated. The second group is made up of ML methods which may require a more advanced mathematical and computational background. Methods from the second group are in general more complex and require more computational resources than the first group. Here we give a basic description of these methods, their limitation and provide some references.

II.2.2.1 Traditional interpolation and fitting methods

The traditional interpolation and fitting methods are either interpolatory, i.e., the approximation is designed such that it exactly includes the data points, or they produce an approximate fit, where a distance function between the data and the model is minimized. Many of these methods rely on polynomials as building blocks to model the data. Some models have a fixed order of approximation, while others let the number of terms be a free parameter. These methods are relatively straightforward to use and do not usually require much computational power.

1. **Linear interpolation**

   Linear interpolation is a straight line approximation that predicts the value of an unknown data point which lies between two known points [50]. Given its simplicity, this method has been widely used as a standard method to perform interpolation in various fields. If we have several data points, the transition between the adjacent data points is only continuous but not smooth. Higher order methods such as cubic interpolation can be used if a smoother approximation is desired (see subsection 2).

Since linear interpolation is available as a standard Python package, we include this method to compare to other more complicated techniques. In particular, we investigate the application of multivariate linear interpolation on a regular grid using the regular grid interpolator (RGI) [51, 52] that is available in `scipy`.

The mathematical background of linear interpolation can be explained as follows. Assume two known points (x_0, y_0) and (x_1, y_1) and an unknown point (x, y) with $x_0 \leq x \leq x_1$. This method assumes that the slope between x_0 and x is equal to the slope between x and x_1. Hence, we use the following relation to predict the data point y in one dimension.

$$\frac{y - y_0}{x - x_0} = \frac{y_1 - y}{x_1 - x} \qquad \text{(II.7)}$$
$$\Leftrightarrow y = y_0 + (x - x_0)\frac{y_1 - y_0}{x_1 - x_0}.$$

In dimensions $d > 1$, this method requires a regular grid of data points as a training set.

Multivariate linear interpolation works as follows. Let $y_i(\vec{x})$ be the data point we want to predict, where $\vec{x}$ denotes the input parameters in d dimensions. Initially, we need to obtain the parameters of the projection of $y_i(\vec{x})$ in $d-1$ dimensions, followed iteratively by $d-2$ and so on until we reach one-dimensional case $d = 1$. Once we obtain these projection points, we can employ Eq (II.7) to predict the values of these points in one dimension. Subsequently, we use the predicted values as the known points to predict the result in higher dimensions iteratively. We then repeat the process further to find $y_i(\vec{x})$ in d dimensions. This algorithm involves a small number of multiplications and additions, which are relatively fast.

Since RGI assumes a regular grid, it is affected by *the curse of dimensionality*: the number of training points grows as the power of d. Therefore, we only investigate this method in three dimensions.

Other popular regression methods that we do not consider here are ridge regression [53], LASSO regression [54], and Bayesian regression [55]. One reason is that the GW training data is quite well-behaved and does not usually include outliers such that would require special treatment.

2. **Tensor product interpolation**

   On regular or Cartesian product grids one can use the same univariate interpolation method in each dimension and the grid points can be unequally spaced. This gives rise to TPI methods. Popular choices for the univariate

method are splines [56] and, if the data is very smooth, spectral interpolation [57, 58].

Let us assume that we want to model a waveform quantity $X(t; \vec{\lambda})$ at a particular time $t = t_i$. We define the d-dimensional TPI interpolant (where $d = \dim(\vec{\lambda})$) as an expansion in a tensor product of one-dimensional basis functions $\Psi_j(\lambda_j)$,

$$I[X](t_i; \vec{\lambda}) = \sum_{j_1,\ldots,j_d} a_{j_1,\ldots,j_d} \left(\Psi_{j_1} \otimes \cdots \otimes \Psi_{j_d}\right)(\vec{\lambda}), \tag{II.8}$$

A popular choice for the basis functions are univariate splines, which are piecewise polynomials of degree $k - 1$ (order k) with continuity conditions. For instance, cubic splines have degree $k = 4$ and continuous first and second derivatives. The boundaries of the domain require special attention. A simple choice is the natural spline where the second derivative is set to zero at the endpoints. If boundary derivatives are not known it is better to use the so-called "not-a-knot" boundary condition [56]. This condition is defined by demanding that even the third derivative must be continuous at the first and last knots.

To construct splines in a general manner it is advantageous to introduce basis functions with compact support, so-called *B-splines*. We denote the i-th B-spline basis function [56, 59] of order k with the knots vector $\vec{t}$, a nondecreasing sequence of real numbers, evaluated at x by $B_{i,k,t}(x)$. The knots refer to the locations in the independent variable where the polynomial pieces of B-spline basis function are connected. For distinct knots $t_i, \ldots, t_{i+k+1}$, the B-splines can be defined as

$$B_{i,k,t}(x) := (t_{i+k} - t_i)[t_i, \ldots, t_{i+k}](\cdot - x)_+^{k-1}, \tag{II.9}$$

where $[t_i, \ldots, t_{i+k}]f$ is the *divided difference* [56, 59] of order k of the function f at the sites $t_i, \ldots, t_{i+k}$, and $(x)_+ := \max\{x, 0\}$. The B-splines can also be defined in terms of recurrence relations. The definition can be extended to partially coincident knots which are useful for the specification of boundary conditions. B-splines can be shown to form a basis [56] of the spline space for a given order and knots vector. A spline function or spline of degree k with knots $\vec{t}$ can be then defined as an expansion

$$s = \sum_i s_i B_{i,k,t}(x), \tag{II.10}$$

with real coefficients $\{s_i\}_{i=1}^n$. Given data, a fixed order and knots vector, and a choice of boundary conditions, we can solve the linear system for the

spline coefficients s_i. For efficient evaluation we only compute the parts of the B-spline basis functions that are nonzero.

For smooth data, Chebyshev interpolation [57, 58] is a popular choice. Chebyshev polynomials (of the first kind) are defined as the unique polynomials satisfying

$$T_n(\cos(\theta)) = \cos(n\theta) \tag{II.11}$$

on [-1,1]. In contrast to splines where the polynomial degree is usually low, global high order polynomial interpolation requires a special choice of nodes to be well-conditioned. A good choice are Chebyshev-Gauss-Lobatto nodes (which are defined to be the extrema of the $T_n(x)$ plus the endpoints of the domain)

$$x_k = -\cos\left(\frac{k\pi}{m-1}\right), \quad k = 0, \ldots, m-1. \tag{II.12}$$

Then we can approximate a function $f(x)$ by an expansion

$$f(x) \approx I[f(x)] := \sum_{k=0}^{m-1} c_k T_k(x), \tag{II.13}$$

For $f \in C^\infty$ the error of Chebyshev interpolation converges exponentially with the number of polynomials $T_n(x)$.

Tensor product interpolation is a very useful tool for constructing fast *reduced order models* (ROM) or *surrogate models* of time or frequency dependent functions that depend on a moderate number of parameters $\vec{\lambda}$. TPI with splines and Chebyshev polynomials has been used to build several GW models [21, 29, 24, 23] and [60], respectively. TPI is not available in standard Python packages. For TPI spline interpolation we use the Cython [61] implementation in the `TPI` package [62].

3. **Polynomial fits**

   A polynomial fit is a multiple linear regression model where the independent variables form a polynomial [63].

   Different settings of maximum polynomial degrees may cause *underfitting* or *overfitting*, therefore care must be taken in choosing the ansatz.

   Assume that we have N training points $(\{\vec{x}_i, y_i\} \in \mathbb{R}^d \times \mathbb{R} | i = 1, \cdots, N)$. Our goal is to find a function or regressor such that each $\vec{x}_i$ yields an output with the lowest error against its function values y_i. We assume that this function $f(\vec{x})$ is expressed by a polynomial of degree k and parameters $\vec{c}$.

In one dimension we have:

$$f(\vec{x}) = c_0 x^k + c_1 x^{k-1} + \cdots + c_{k-1} x + c_k. \tag{II.14}$$

If we had as many degree of freedom as data points, we could demand:

$$f(x_i) = y_i. \tag{II.15}$$

In matrix form, Eq (II.15) can be written as:

$$\mathbf{X}\vec{c} = \vec{Y}$$
$$\begin{pmatrix} x_1^k & x_1^{k-1} & \cdots & x_1 & 1 \\ x_2^k & x_2^{k-1} & \cdots & x_2 & 1 \\ \vdots & & \ddots & & \vdots \\ x_N^k & x_N^{k-1} & \cdots & x_N & 1 \end{pmatrix} \begin{pmatrix} c_0 \\ c_1 \\ \vdots \\ c_k \end{pmatrix} = \begin{pmatrix} y_1 \\ y_2 \\ \vdots \\ y_N \end{pmatrix}, \tag{II.16}$$

where $\mathbf{X}$ is the $N \times (k+1)$ Vandermonde matrix. The parameters $\vec{c}$ are obtained by solving Eq (II.16) for the known input and output data, $\mathbf{X}$ and $\vec{Y}$ in the training set. In general, the linear system may be over or under determined such that no unique solution would exist. Instead, we employ the standard discrete least squares fit to minimize the error (see section 10 of [64] and [65]):

$$\Sigma_{j=1}^{N} |f(x_j) - y_j|^2 \tag{II.17}$$

Similar to linear interpolation, univariate polynomial interpolation is available in the `scipy` package.

Ref [63] discusses several methods and provide an overview of multivariate interpolation with polynomials. We employ polynomial fits for multivariate interpolation as in [66] and explained more detail in [67].

4. **Greedy multivariate polynomial fit (GMVP)**

   London and Fauchon-Jones [31] recently introduced methods that build an interpolant for a given data set by adaptively choosing a small set of analytical basis function from a certain class of functions. In our study here, we test the GMVP procedure described in detail in Sec. II B of [31].

   In this method, a scalar function, f, that is known at discrete points in the d-dimensional parameter space, $\vec{x}_j = \{x_j^1, x_j^2, \ldots, x_j^d\}$, is approximated by a linear sum of analytical basis functions, $\phi_k(\vec{x})$,

$$f(\vec{x}) \approx \sum_k \mu_k \, \phi_k(\vec{x}). \tag{II.18}$$

Given a set of basis functions, the coefficients μ_k are determined by a 'least-squares' optimal fit to the known function values $f(\vec{x}_j)$. In practice, this is calculated using the pseudoinverse (Moore-Penrose) matrix of $\phi_k(\vec{x}_j)$ (that is, the values of the basis functions at the given location in the parameter space).

In GMVP, the basis functions are chosen to be multivariate polynomials of maximal degree D. In order to prevent overfitting, however, not all possible polynomial terms from the set

$$\phi_k(\vec{x}) \in \left\{ (x^1)^{\alpha_1} (x^2)^{\alpha_2} \dots (x^n)^{\alpha_d}, \quad \sum_{i=1}^{n} \alpha_i \leq D \right\} \tag{II.19}$$

are included in the basis. Instead, a greedy algorithm [67] iteratively adds the basis functions to (II.18) that minimize the error

$$\epsilon^2 = \frac{\sum_j \left[f(\vec{x}_j) - \sum_k \mu_k \, \phi_k(\vec{x}_j) \right]^2}{\sum_j \left[f(\vec{x}_j) \right]^2}. \tag{II.20}$$

This process terminates when the difference in ϵ between two successive iterations becomes smaller than some user-defined tolerance. In order to improve the stability of the algorithm, the maximally allowed multinomial degree D is successively increased, which the authors of [31] refer to as degree tempering.

In our study, we use GMVP with a tolerance of $\epsilon = 5 \times 10^{-4}$ and a maximal multinomial degree of $D = 16$.

5. **Radial basis functions (RBF)**

   Radial basis functions [68] are an approximation for continuous functions, where the predicted outputs depend on the Euclidean distance between the points and a chosen origin. This method is applicable in arbitrary dimensions and does not require a regular grid.

   We include RBF in this study due to several reasons. Primarily, because this method is simple, rapid, and has been integrated as a standard Python package in `scipy`. Moreover, RBFs are used in machine learning as activation functions in radial basis functions neural networks (see section II).

   The mathematical background of RBFs is explained as follows. Let N be the number of training points, $\vec{x}_i$ the parameters of each data point, and y_i the data defining the training set $\{(\vec{x}_i, y_i) \in \mathbb{R}^d \times \mathbb{R} | i = 1, \dots, N\}$.

The goal is to find an approximant $s : \mathbb{R}^d \to \mathbb{R}$ to the function $y : \mathbb{R}^d \to \mathbb{R}$ such that $s(\vec{x}_i) = y_i$ (s interpolates y at the chosen points) with the form:

$$s(\vec{x}) = \sum_{i=1}^{N} w_i \varphi(r), \tag{II.21}$$

where $\vec{x}$ is the vector of independent variables, w_i are the coefficients, r is the Euclidean distance between $\vec{x}$ and $\vec{x}_i$ ($r = \|\vec{x} - \vec{x}_i\|$), and $\varphi(r)$ is known as the *radial basis function*.

To obtain the approximant s, we need to solve:

$$\Phi(r)\vec{w} = \vec{Y}, \tag{II.22}$$

where $\Phi(r) = \{\|\vec{x} - \vec{x}_i\|\}_{x,x_i \in \Xi}$, $\vec{Y} = \{y_i\}_{i=1}^N$ and $\vec{w} = \{w_i\}_{i=1}^N$. Ξ is a finite subset of $\mathbb{R}^d$ with more than one element [68]. We can solve the linear system for the coefficients and obtain the interpolant. Hence, the computational complexity and thus the training time of RBF is dominated by the computation of vector coefficients $\vec{w}$ that involves matrix inversion and goes as $O(N^3)$ [69].

The interpolation matrix $\Phi(r)$ has to be nonsingular so that it does not violate the Mairhuber-Curtis theorem [68]. The solution is to choose a kernel function such that $\Phi(r)$ is a semi-definite matrix and therefore nonsingular. One common choice is the multiquadric kernel function $\varphi(r)$ expressed by:

$$\varphi(r) = \sqrt{1 + \left(\frac{r}{\varepsilon}\right)^2}, \tag{II.23}$$

where ε is the average distance between nodes based on a bounding hypercube as defined in `scipy` [70].

The multiquadric kernel function is commonly applied to scattered data because of its versatility due to its adjustable parameter ε which can improve the accuracy or the stability of the approximation. Ref. [68] shows that this kernel is also able to approximate smooth functions well so that it useful for approximation. Hence, we employ the *multiquadric* kernel function in this study.

II.2.2.2 Machine learning methods (ML)

Machine learning is the scientific study of computer algorithms and statistics which aims to find patterns or regularities in the data sets. Systems learn from

the training data and can predict output values for test data. ML is a branch of artificial intelligence.

Although the distinction is a blur, one major difference between ML and traditional interpolation methods lies in their objectives. In traditional methods, the objective is not only to provide an approximation of an underlying function from which the training data were generated, but also to understand the mathematical process behind the relation of input and output data. In that case, we seek interpolants or fits which often can be found analytically by solving linear systems for the coefficients in the model. Hence, the traditional methods originated from approximation theory and numerical analysis in mathematics. Conversely, in machine learning, the objective is to recognize patterns from the input-output training set and to construct a model from this data. Although we know that the result follows some mathematical procedures that depend on free parameters, these details are considered to be less important. Hence ML can be seen as a sub-field of computer science.

1. **Gaussian process regression (GPR)**

   GPR is a unique method that combines statistical techniques and machine learning. It can predict function values away from training points and can provide uncertainties of the predicted values, which will be useful for certain applications. GPR can be used with multivariate scattered data.

   Compared to traditional methods, GPR requires more knowledge of advanced statistics such as covariance matrices, regression and Bayesian statistics for the optimization strategy. GPR can be considered as a combination of traditional and machine learning methods.

   We provide a summary of GPR as discussed in detail in Ref. [71, 72]. We start with the most important assumption in GPR. Any discrete set of function values $y_i = y(\vec{x}_i)$ is assumed to be a realization of a Gaussian process (GP). Assuming the data can be pre-processed to have zero mean, $\mu(\vec{x}) = 0$, the covariance function $k(\vec{x}, \vec{x}')$ fully defines the Gaussian process:

$$y(\vec{x}) \sim GP\Big(\mu(\vec{x}) = 0, k(\vec{x}, \vec{x}')\Big). \tag{II.24}$$

   Assume that we want to predict the value y_* at $\vec{x}_* \in \mathbb{R}^d$ and that we have N numbers of training points, where each point depends on d parameters expressed by $\{(\vec{x}_i, y_i)|i = 1, \ldots, N\}$. The training and test outputs can be written as follows:

$$\begin{bmatrix} \vec{y} \\ y_* \end{bmatrix} \sim \mathcal{N}\left(0, \begin{bmatrix} K(X,X) + \sigma_n^2 I & K(X, X_*) \\ K(X_*, X) & K(X_*, X_*) \end{bmatrix}\right), \tag{II.25}$$

where $K(X, X)$ denotes the matrix of the covariances evaluated at all pairs of the training points and similarly for $K(X_*, X_*)$, $K(X, X_*)$, and $K(X_*, X)$, σ_n^2 (also called *nugget*) is the variance of the Gaussian (white) *noise* kernel that will be discussed later (see the *hyperparameters*).

Explicitly, in order to predict a single value y_*, we need to compute $K(X, X)$ as the covariance matrix between each point in the training set, $K(X, X_*)$ and its transpose that are vectors and the scalar $K(X_*, X_*)$. In a different form, our main goal is to find the conditional probability expressed by the following distribution:

$$p(y_*|\vec{x}_i, \vec{x}_*, \vec{y}, \vec{\theta}) = \mathcal{N}(\bar{y}_*, \mathrm{var}(y_*)), \tag{II.26}$$

i.e., the probability of finding the value y_* given the training data $\vec{x}_i$ and $\vec{y}$, the hyperparameters $\vec{\theta}$, and the location $\vec{x}_*$ is a normal distribution with mean $\bar{y}_*$ and variance $\mathrm{var}(y_*)$.

The mean and variance can be shown to be:

$$\bar{y}_* = K(X_*, X)(K(X, X))_{ij}^{-1} y_j \tag{II.27}$$

$$\mathrm{var}(y_*) = K(X_*, X_*) - K(X_*, X_i)(K(X, X))_{ij}^{-1} K(X_*, X_j). \tag{II.28}$$

In the equation above, the covariance $K(x_i, x_j)$ is expressed by:

$$K(x_i, x_j) = \sigma_f^2 k(x_i, x_j) + \sigma_n^2 \delta_{ij}, \tag{II.29}$$

where σ_f and σ_n are hyperparameters, δ_{ij} is the standard Kronecker delta, $k(x_i, x_j) = k(r)$, and r is the distance:

$$r = \sqrt{(\vec{x} - \vec{x}')^T M (\vec{x} - \vec{x}')}. \tag{II.30}$$

In the following, we discuss the form of M as a diagonal matrix with a tunable length scale in each physical parameter which form part of the hyperparameters.

The hyperparameters

We assume that our training data has some numerical noise σ_n^2 and a scale factor σ_f that can be estimated by optimizing the hyperparameters $\vec{\theta} = \{\sigma_f, \sigma_n, M\}$. For instance, the explicit form of M in the seven-dimensional case is:

$$M = \mathrm{diag}(\ell_q^{-2}, \ell_{\chi_{1x}}^{-2}, \ell_{\chi_{1y}}^{-2}, \ell_{\chi_{1z}}^{-2}, \ell_{\chi_{2x}}^{-2}, \ell_{\chi_{2y}}^{-2}, \ell_{\chi_{2z}}^{-2}), \tag{II.31}$$

where the ℓ_i are length scales. Ref. [73] describes the length-scale ℓ as the distance taken in the input space before the function value changes significantly. Small values of the lengthscale ℓ imply that the function values change quickly and vice versa. Hence, the lengthscale ℓ describes the smoothness of a function.

To determine the hyperparameters, we can maximizse the marginal log-likelihood:

$$\ln p(y_i|\vec{x}_i, \vec{\theta}) = -\frac{1}{2}\Big(y_i(K(X,X))^{-1}_{ij} y_j + \ln|K(X,X)| + N\ln 2\pi\Big). \qquad \text{(II.32)}$$

Because the log-likelihood may have more than one local optimum, we repeatedly start the optimizer and we choose ten repetitions. For the first run, we set the initial value of each length scale to unity, with bounds of 10^{-5} to 10^5. Furthermore, we set $\sigma_n^2 = 10^{-10}$, where higher σ_n^2 value means that the data are more irregular. The subsequent runs use the allowed values of the hyperparameters from the previous runs until the maximum number of iterations is achieved.

In Eq (II.32), we see that the partial derivatives of the maximum log likelihood can be computed using matrix multiplication. However, the time needed for this computation grows with more data in the training set as $O(N^3)$. Additionally, we employ Algorithm 2.1 of [71], because Cholesky decomposition is about six time faster than the ordinary matrix inversion to compute Eq (II.32). We highlight that although GPR becomes more accurate in predicting the underlying functional form of the data given more training points N, it has complexity $O(N^3)$ and therefore the method becomes ineffective for large N.

We estimate the posterior distribution of the hyperparameters using Bayes' theorem as follows:

$$p(\vec{\theta}|\vec{x}_i, y_i) \propto p(\theta)p(y_i|\vec{x}_i, \vec{\theta}), \qquad \text{(II.33)}$$

where we employ a uniform prior distribution $p(\theta)$. Additionally, we use the `sckit-learn` package [72] to optimize the hyperparameters as in the implementation of Algorithm 2.1 in [71].

This method is non-parametric because no direct model ansatz is used. Note however that a choice for the covariance function needs to be made.

The covariance functions

In statistics, covariance expresses how likely two random variables change together [74]. Various choices of covariance functions which are usually

called kernels $k(\vec{x}, \vec{x}')$ are discussed in more detail in Ref. [72] and [71]. In this study, we compare the two most commonly used kernel functions in GPR: the squared exponential kernel and the Matérn kernel explained below.

(a) The squared exponential kernel (SE) is a standard kernel for Gaussian processes:

$$k_{SE}(r) = \exp\left(\frac{-r^2}{\ell^2}\right), \tag{II.34}$$

with r defined in Eq. II.30 and ℓ is the length-scale.

(b) The Matérn class of kernels is named after a Swedish statistician, Bertil Matérn and has less smoothness than the SE kernel. The Matérn kernel is given by:

$$k_M(r) = \frac{2^{1-\nu}}{\Gamma(\nu)}\left(\frac{\sqrt{2\nu}r}{\ell}\right)^{\nu} K_\nu\left(\frac{\sqrt{2\nu}r}{\ell}\right), \tag{II.35}$$

where K_ν is a modified Bessel function [75], Γ is the gamma function and ν is usually half-integer. Common choices of ν are $k_{\nu=3/2}$ and $k_{\nu=5/2}$.

$$k_{\nu=3/2}(r) = \left(1 + \frac{\sqrt{3}r}{\ell}\right)\exp\left(-\frac{\sqrt{3}r}{\ell}\right), \tag{II.36}$$

$$k_{\nu=5/2}(r) = \left(1 + \frac{\sqrt{5}r}{\ell} + \frac{5r^2}{3\ell^2}\right)\exp\left(-\frac{\sqrt{5}r}{\ell}\right). \tag{II.37}$$

The Matérn kernel is a generalization of the radial basis function kernel. For $\nu = 1/2$, it reduces to exponential kernel and $\nu = \infty$ reduces to the SE kernel. We use the Matérn kernel with $\nu = 3/2$ in our analysis.

2. **Artificial neural networks**

Artificial neural networks (ANNs) as computing systems are inspired by emulating the work of brains to learn complex things and to find patterns in biology. In machine learning algorithms, ANN has been widely used as a framework to perform advanced tasks such as pattern recognition [76], forecasting [77], and many other applications in various disciplines [78]. This framework works analogously to brains: it receives some inputs, processes them, and yields some output [79].

In this study, we employ ANNs or feedforward networks as the simplest neural networks architecture to perform interpolation. The feedforward network with hidden layers can approximate of any function which is known

as the universal approximation theorem [79, 80]. This class is called *feed-forward* because the information flow from the input to the output and the connection between them does not form a cycle (loop). In our case, the inputs are the waveform's parameters $\vec{\lambda}$ and the output is the predicted value of $A(t_i;\vec{\lambda})$ or $\phi(t_i;\vec{\lambda})$. We define *hidden layer* as a layer between the input and the output of ANN [2].

Four types of commonly used ANNs are:

- Single-layer perceptron
  In a single-layer perceptron, the inputs are weighted and fed directly to the output. Hence, the single-layer perceptron is the simplest neural network system.
- Multi-layer perceptron
  In multi-layer-perceptron (MLP), there is at least one hidden layer between the input and the output layer, where each neuron in each layer is connected to another neuron in the following layer.
- Radial basis function network
  This class has the same workflow and architecture as the MLP with input, hidden layers and output, where each neuron is connected directly to the following layer. The only difference is the input, where the radial basis function network (RBFN) uses the Euclidean distances with respect to some origin as its input and Gaussian activation functions [81].
- Convolutional neural network
  The feedforward convolutional neural network is commonly used to train neural network for visual analysis. Convolutional neural networks use convolution in place of general matrix multiplication in at least one of its layers [79].

We employ MLP as one of the simplest architectures to perform function approximation [80, 82]. Fig. II.2 shows the illustration of the network architecture used in this study.

In Fig. II.2, each layer consists of a finite number of neurons. Each neuron in each layer is connected to the subsequent layer and the previous layer which are generally called *links* or *synapses*. The workflow of MLP is explained as follows:

[2] In some references, the input layer is counted as the first hidden layer. Here we use the definition of *hidden layer* as a layer between the input and the output layer

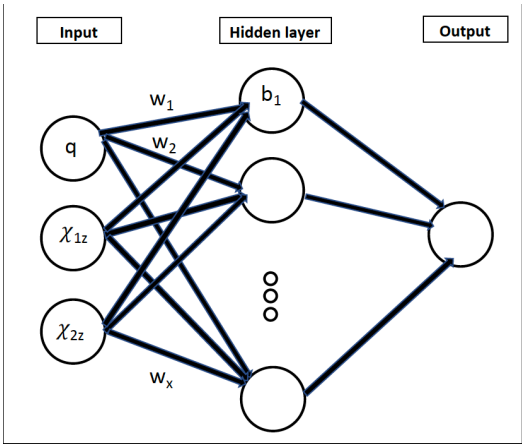

Figure II.2: Diagram of ANN architecture used for three-dimensional interpolation in this study. The circles represent the neurons and we indicate weights w_i along neuron connections and biases b_i.We employ two layers in the hidden layer part of the diagram. The same architecture is used for the seven-dimensional case, where the input contains seven neurons that depend on the seven parameters.

(a) Define the input as x_{ij}, where i is the index of the layers. Starting at $i = 0$ at the input layer, and j indexes the neurons in a layer. Thus, with x_{0j}, $j = 1, 2, 3$ corresponds to q, χ_{1z}, χ_{2z} respectively.

(b) The k-th neuron of the $(i + 1)$-th layer receives the value of x_{ij} from the i-th layer multiplied by the weight w_{ijk}. These products are then summed over all links from the i-th to the $(i + 1)$-th layer.

(c) A bias or shift b_{ik} is added to the above value and an activation function σ is applied to the final result. In this study, we use the Rectified Linear Unit (ReLU) [83] because it faster than other functions such as *sigmoid* and *tanh* and it is commonly used in other studies. ReLU is mathematically expressed by the following equation:

$$\sigma(z) = \max(z, 0), \tag{II.38}$$

and the MLP procedure is expressed by the following relation:

$$x_{i+1,k} = \sigma\left(\sum_j w_{ijk} x_{ij} + b_{ik}\right) \tag{II.39}$$

We vary the number of neurons in the first hidden layer between 2 to 2000 for the three-dimensional data sets and 2 to 5000 for the seven-dimensional

data sets. We then set the number of neurons in the second hidden layer identical to the first hidden layer. For each network and training data set, we compute mean squared error and the mean absolute error (see [84]) of $A(t)$ and $\phi(t)$, respectively.

To train the networks, the training data is separated into several *batches*, where each batch contains the same number of data samples. Each batch is then passed through the networks (see Eq. II.39). When each data sample in the training set has had an opportunity to pass the networks a single time, this is known as an *epoch*. The number of epochs affects the learning of the networks, i.e., the higher the epoch, the better the learning. In this study, we set our batch size to five and train them through one thousand epochs.

The networks compute the *loss functions* during each epoch. The *loss functions* measure the errors or inconsistency between the predicted value and the true data. In this study, we employ the *mean squared error* loss function for $A(t)$ and the *absolute error* for $\phi(t)$ respectively (see Ref. [84]).

Training neural networks means that we minimize the loss functions so that our predicted values are as close as possible to the true values [85]. To minimize the loss functions, the networks adjust learnable parameters, i.e., the values of the weights and biases of the model. In most cases, the minimization cannot be solved analytically, but can be approached with *optimization algorithms*.

During optimization, the network learns the values of weights and biases of the previous epoch and calculates its loss functions. Subsequently, it adjusts the values of weights and biases in the next epoch so that the loss functions become smaller. One way to minimize the loss functions is to compute the gradient values with respect to the learnable parameters. In this study, we employ *Adam* [86] as the optimization algorithm. Adam is a popular algorithm in deep learning due its robustness (see Ref. [86] for more detail).

Following the above procedure, a model is then saved at the end of the run and evaluated through the test data. We then compute the accuracy and execution time of this process similar to other methods. We employ `Keras` [84] and `TensorFlow` [87] to perform this computation.

II.3 Results

In this section, we show results for accuracy and computational time for different regression methods. We apply methods to the three-dimensional and seven-dimensional data sets defined in sec. II.

II.3.1 Three-dimensional case

We investigated the results for aligned spin waveforms with parameters q, χ_{1z}, and χ_{2z}. Training points were given on a regular grid. We placed the same number of points equally spaced to each other for each parameter (see sec. II). Hence the total number of training points is proportional to the number of training points per dimension cubed. We then varied the number of training points in each dimension from five to eleven which corresponds to a total number of training points of 125 to 1331. We distributed 2500 test points randomly (see section II). These test points are located inside the same domain covered by the training points. Hence, we do not test how well the methods perform for extrapolation.

We calculated relative errors (in percent) for the amplitude $A(t)$:

$$\varepsilon_{re} = \frac{\sum_i^N |A^i_{\rm pred}(t) - A^i_{\rm true}(t)|}{\sum_i^N |A^i_{\rm true}(t)|} \times 100. \tag{II.40}$$

The phase error is an important diagnostic to measure the accuracy of GW waveform models. Therefore, we consider the absolute phase error (in radians)

$$\varepsilon_{ae} = \frac{1}{N} \sum_i^N |\phi^i_{\rm pred}(t) - \phi^i_{\rm true}(t)|. \tag{II.41}$$

ε_{re} and ε_{ae} are the relative error and the average of the absolute error, respectively, $A_{\rm pred}(t)$ and $\phi_{\rm pred}(t)$ are the predicted results of the amplitude and phase regression respectively, and $A_{\rm true}(t)$ and $\phi_{\rm true}(t)$ are their true values.

Subsequently, we investigated the computational time taken to evaluate each interpolation method. Here we define the *training time* as the time to compute the interpolant and the *execution time* being the time to compute the 2500 interpolation points following our test set. Furthermore, we define *total time* as the sum between the training time and the execution time, i.e., the entire process to perform interpolation for 2500 points. The comparison results in the early inspiral ($t = -3500M$) are shown in Fig. II.3, whereas the results at $t = -50M$ are shown in Fig. II.4. We now discuss the results shown the results for different regression methods.

1. **Traditional interpolation and fitting methods & GPR**

   We expect that the key quantities for two waveform models, `SEOBNRv3` and `IMRPhenomPv2` agree quite well in the early inspiral. The error in $A(t)$ and $\phi(t)$, decreases with more training points for both models. This result is expected as we populate our parameter space with more points located on a regular grid.

For both quantities, we find that errors for different methods are similar between waveform models. GPR errors show a dependence on the kernel choice. We first consider the amplitude errors. For `SEOBNRv3` the errors fall off in a similar way for either choice of kernel, whereas for `IMRPhenomPv2` the error is much higher for the SE kernel compared to the Matérn kernel. This is likely due to the higher level of noise in the `IMRPhenomPv2` data due to the inverse Fourier transformation.

The SE kernel assumes a higher degree of smoothness in the data than the Matérn kernel. Similarly, we find for either waveform model that the SE kernel shows a higher phase error than the Matérn kernel.

2. **Artificial neural networks**

We now discuss errors for ANNs as indicated by the filled circles in Fig. II.3. Here we compare the results of the double layer MLP with various numbers of neurons. By design, the double layer MLP consists of one input layer, two hidden layers, and one output layer. We set the number of inputs as the dimensionality of the parameter space and only produce a single output. In the aligned spin case, our inputs are the parameters q, χ_{1z}, and χ_{2z} and output is either $A(t)$ or $\phi(t)$. For the hidden layers, we varied the number of neurons between 2 and 2000 in the first hidden layer, and set an equal number of neurons for the second hidden layer.

Thus, we obtained a set of errors as we modified the number of neurons in the *hidden layers* for a fixed number of training points N per dimension. In Fig. II.3, we only show the results of the smallest errors for each training set. In this plot, different colors of the circles correspond to different numbers of neurons as indicated by the color bar. We note that the ANN with the smallest error may not be the fastest one.

Regarding the computational time, the training time obviously grows with the number of neurons per layer. However, we argue that there is no guarantee that many neurons yield smaller error than fewer neurons. In fact, too many neurons lead to overfitting and too few neurons lead to underfitting. We could reduce overfitting by activating the *Dropout* function in `Keras`, *Dropout* removes the result from a selected number of neurons randomly. However, we prefer to not include an additional stochastic element and do not include *Dropout* in this study.

Next, we compare execution times. Execution time is relatively similar between the GPR, RBF, TPI, and ANN methods. Other traditional methods such as linear, polynomial fit and GMVP, and linear interpolation are faster.

To ensure a fair comparison between all methods, we explored the performance on the same machines (2x Intel Xeon E5-2698 v4) with 20 CPU cores, 256 Gigabytes of RAM, and 1x HDD (1TB, 6Gbps) of storage.

Due to the limited scope of our study, we only investigate results for the double layer ANN. This leaves tuning parameters and architectures to be explored in future studies. A possible way to reduce training and execution times is to use on GPUs instead of CPUs.

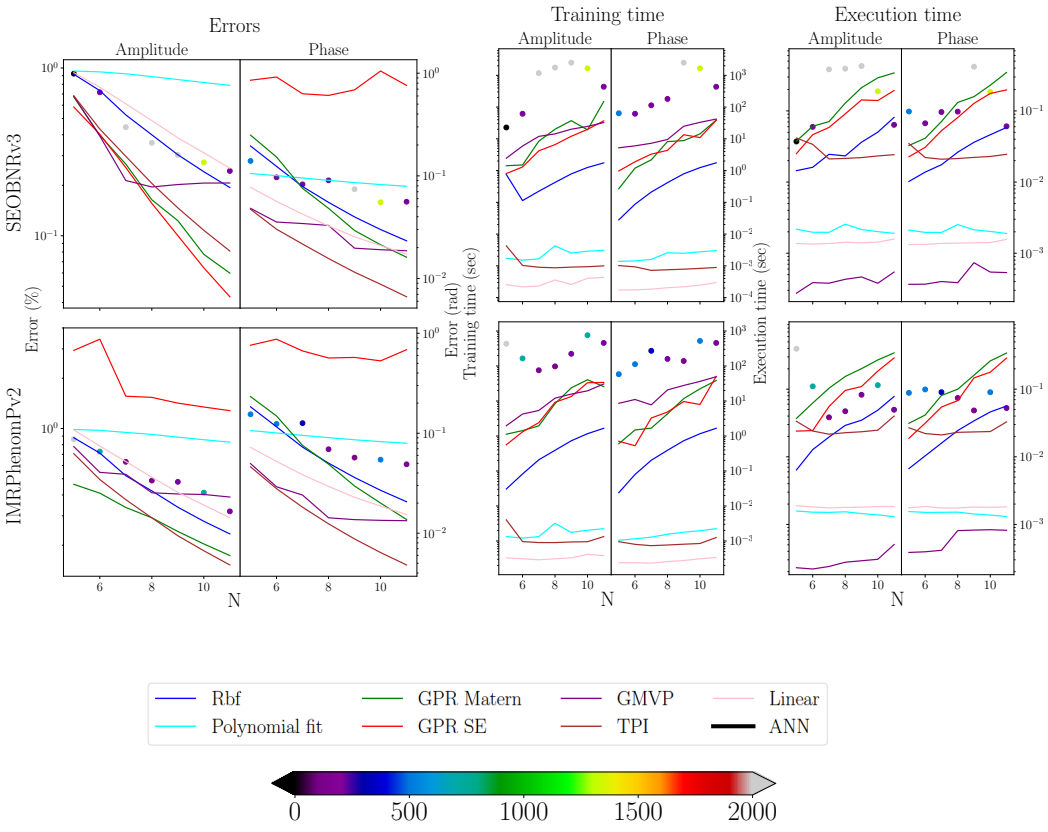

Figure II.3: The three-dimensional interpolation results at t=-3500M. Top: `SEOBNRv3`*, bottom:* `IMRPhenomPv2`*. The x-axes show the number of training points in each dimension, N, and the y−axes show the errors, training, and indicated execution time as on the labels of the panels. Left: errors of the amplitude and phase respectively, middle: training time in (seconds), and right: execution time (seconds). Different colors represent different interpolation methods as shown in the shared legend. The colored circles show ANN results, where different colors represent the number of neurons per layer in a double layer ANN as shown in the corresponding color bar.*

Finally, we discuss results for training times. The training time for RBF and GPR rise proportionally with the number of training points. In RBF, this is caused by the least-squares-fit computation that takes a longer time with more training points. For GPR, the training time goes as $O(N^3)$ with N the number of training points as explained in Sect. II. Polynomial fit, TPI and linear interpolation do not depend strongly on the size of the training set and their training time is relatively fast.

For both models, ANN yields comparable errors and execution times as other interpolation methods, but generally with longer training time than other methods. Several methods have execution times that are independent of the size of the training set for a fixed order of approximations. This includes TPI, linear interpolation, polynomial fit, and ANNs.

Combining all the results at $t = -3500M$ and at $t = -50M$, we found that the errors are generally larger in noisy data. We also found that the methods with longer training time do not always yield a better result than the methods with less training time (see Fig. II.4).

Using too many neurons in the hidden layers may cause problems such as overfitting. It occurs when the networks have too much capacity to process information such that the amount of information in the training set is not enough to train the networks [88]. Hence, the number of neurons must be set such that there are not too few or not too many. The selection however, depend on the architecture of the networks and the *hyperparameters*.

II.3.2 Seven-dimensional case

In seven dimensions, we distribute the training points randomly in each dimension. The main reason for this placement is to avoid the *curse of dimensionality* as explained in the previous section. Similarly to the three-dimensional case, we investigate training sets of different sizes, from 500 to 3000 points. As discussed in Sec. II, the seven-dimensional case has a narrower range of mass ratio ($1 \leq q \leq 2$) than the three-dimensional one ($1 \leq q \leq 10$) and full-spin range.

We construct a single test set with 2500 points distributed randomly and located within the parameter ranges. Some of the test points may be outside the domain covered by the training points. This means that our results may contain a small extrapolation.

Since TPI and linear interpolation require regular grid training points, we do not include them in our analysis. For other methods, we employed the same settings (kernels, hyperparameters, degree) as in the three-dimensional case.

We built the architecture of ANN in a similar way as before. The results of the seven-dimensional case for different interpolation methods ($t = -3500M$ and $t = -50M$) are shown in Fig. II.5.

We observed that errors of SEOBNRv3 are not significantly different than the corresponding three-dimensional results. Furthermore, the errors of this model at $t = -50M$ are higher than at $t = -3500M$ in a similar way as in three dimensions.

Surprisingly, the relative amplitude errors for IMRPhenomPv2 (top left plots) in the late inspiral are smaller than in the early inspiral in contrast to SEOBNRv3. The $A(t)$ quantity of IMRPhenomPv2 is smoother at $t = -50M$ than at $t = -3500M$. We emphasize that both models, SEOBNRv3 and IMRPhenomPv2 have comparable amplitude values at $t = -50M$ and at $t = -3500M$.

In the early inspiral ($t = -3500M$), both waveforms agree well, similar to the three-dimensional case. Hence, the percent errors are not significantly different as shown in the same plot.

The phase errors were computed as absolute errors (see Eq. II.41). We find that the phase errors for SEOBNRv3 and IMRPhenomPv2 are comparable. Furthermore, the late inspiral errors are higher than the early inspiral as the data fluctuates more. In Fig. II.5, we observe a similar behavior for the training time as in three dimensions, where higher training time was found for GPR, ANN, and RBF. This is caused by the same factors as explained in the three-dimensional case. For the execution time (right panel), we found that the more complex methods take longer time than the simpler methods. For RBF and GPR this is due to their dependence on the size of the training set. Interestingly, the execution time for ANNs is faster than GPR and RBF. This is because ANN picks the optimum weights and biases during the training and its execution time does not depend on the number of training points in the data.

We remind the reader that we set the parameter space of the seven-dimensions analysis narrower in mass ratio than the three-dimensions. Hence, the errors should not be compared directly to the three-dimensional case. For the same parameter ranges, the seven dimensional case yields errors up to 100 times larger for the $A(t)$ and 15 times larger for the $\phi(t)$. The order of accuracy does not significantly change, where the best accuracy in this range is obtained by polynomial interpolation.

Overall, we found that in some cases, a simple method such as polynomial fit yields lower errors and performs faster than the more complex methods.

II.4 Discussion and conclusion

Various approximation methods play important roles in building gravitational waveform models. Methods with high accuracy, low complexity, and fast computational time are needed for current and future applications. In this paper, we presented a comparative study of interpolation, fitting and regression methods applied to precessing and aligned BBH systems. Precessing BBH model depends on

seven key intrinsic parameters $(q, \vec{\chi}_1, \vec{\chi}_2)$, whereas the aligned model depends on three parameters $(q, \chi_{1z}, \chi_{2z})$.

We generated the data sets in the time domain using two waveform models: `SEOBNRv3` (originally built in the time domain) and the inverse Fourier transform of `IMRPhenomPv2` (originally built in frequency domain). The full waveforms were transformed into a precession adapted frame where we extracted two quantities: amplitude $A(t)$ and phase $\phi(t)$ as explained in section II to perform a comparative study. For each key quantity, we picked two points in time, $t = -3500M$ in the inspiral for the smoother data set and $t = -50M$ near merger for the more irregular data. We employed this procedure on different numbers of training sets and used different approximation methods.

We split approximation methods into two categories: traditional methods and machine learning mehods (see Sect. II). The traditional methods consist of linear interpolation, polynomial fits, radial basis function, GMVP, and TPI. Since linear interpolation and TPI package require a regular grid, we do not include them in the seven dimensional analysis. Furthermore, we investigated machine learning methods such as GPR and ANN. For GPR, we compared two kernel functions: the square exponential kernel and the Matérn kernel. We took the mean results of each kernel and compared them against other methods. For ANN, we focused on networks with two hidden layers and varied the number of their neurons.

We computed the relative errors for $A(t)$ and the absolute errors for $\phi(t)$. To validate the result, we generated 2500 test points distributed randomly within the same parameter space. The comparison results of different methods in accuracy, training time and execution time (in second) are presented in Sec.II.

We found that all methods perform better with more training data. Furthermore, we compared the performance of the same method in a set of smoother data and a set of more irregular data. In general, we found that approximation methods perform better in smoother data as expected. We recommend to use preprocessing methods to improve the smoothness of the data where possible which should increase the accuracy of regression results. This preparation is crucial as any methods perform well with smoother data sets. Different accuracies are attained by different methods in handling the irregularities in the data. We give a brief summary of different methods in Table. II.1.

For lower dimensions, simpler methods such as linear interpolation and TPI provide good accuracy and speed. However, these methods need a regular grid and therefore are less useful for high dimensional data sets as explained above. For this situation, we found that polynomial fits are one of the simplest methods that offers a good combination between accuracy and speed. Furthermore, polynomial fits have been used widely and can be coded manually making it reliable and easy. The computational timing of polynomial fits depends on the number of parameters and the maximum polynomial degree. Another method that can per-

form approximation of scattered data sets is GMVP. GMVP which is based on polynomials can perform very well by setting error tolerance on its algorithm. For lower dimensionality, GMVP is computationally cheap. However, as the number of parameters rise, the computational time to compute the interpolant with the same error tolerance grows significantly higher. Therefore, we do not include this method in our analysis for the seven-dimensional case.

RBF and GPR are promising methods for scatterred data points. RBF has been integrated in a standard `scipy` package, making it easy for users. GPR computes the uncertainty of the predicted values. This feature is useful for future applications and cannot be found in other methods. Furthermore, GPR has been integrated in `sckit-learn` package [72]. Both RBF as GPR have the freedom to choose suitable kernel functions and hyperparameters. However, their speed depends on the number of training points cubed $O(N^3)$. Hence, these methods become inefficient for larger data set.

A simple ANN can be used to perform regression for scattered data points. Similar to GPR, this method is more complex and depends on the choice of architecture and hyperparameters. We showed that the the three-dimensional result of ANN requires a longer training time with relatively comparable accuracy to other methods. We argue that such complexity is less needed for lower dimensional parameter and users should use a more simpler methods that provide good accuracy and speed. However, ANN is highly versatile to solve problems in higher dimensions and is promising to be explored further.

One might expect that methods with higher complexity perform better than methods with lower complexity. We find that this is not always the case. A more complicated method does not guarantee that the results are always better or faster. We find that simpler methods may yield smaller errors than more complex methods and perform faster in many cases. Hence, we suggest that one should critically evaluate the performance of approximation methods and understand the features of the method that are necessary for the data of interest. Simpler methods that perform better or at least equal to more complicated methods should be used as the first choice to avoid unnecessary complexity.

Acknowledgments

The authors would like to thank to Lionel London, Scott Field, Stephen Green, Chad Galley, Christopher Moore, Zoheyr Doctor, Rory Smith, Ed Fauchon-Jones, and Lars Nieder for useful discussions. Computations were carried out on the Holodeck cluster of the Max Planck Independent Research Group "Binary Merger Observations and Numerical Relativity." This work was supported by the Max Planck Society's Independent Research Group Grant.

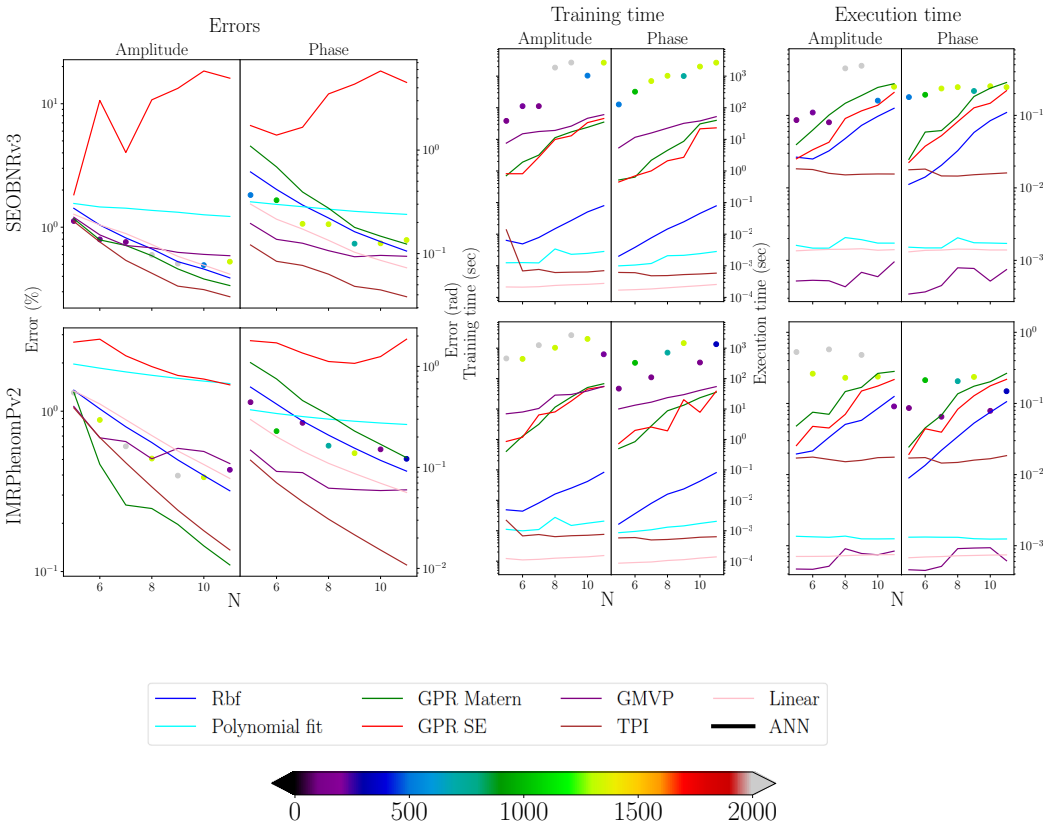

Figure II.4: The three-dimensional interpolation results at t=-50M. Top: `SEOBNRv3`*, bottom:* `IMRPhenomPv2`*. The x-axes show the number of training points in each dimension, N, and the y−axes show the errors, training, and indicated execution time as on the labels of the panels. Left: errors of the amplitude and phase respectively, middle: training time in (seconds), and right: execution time (seconds). Different colors represent different interpolation methods as shown in the shared legend. The colored circles show ANN results, where different colors represent the number of neurons per layer in a double layer ANN as shown in the corresponding color bar.*

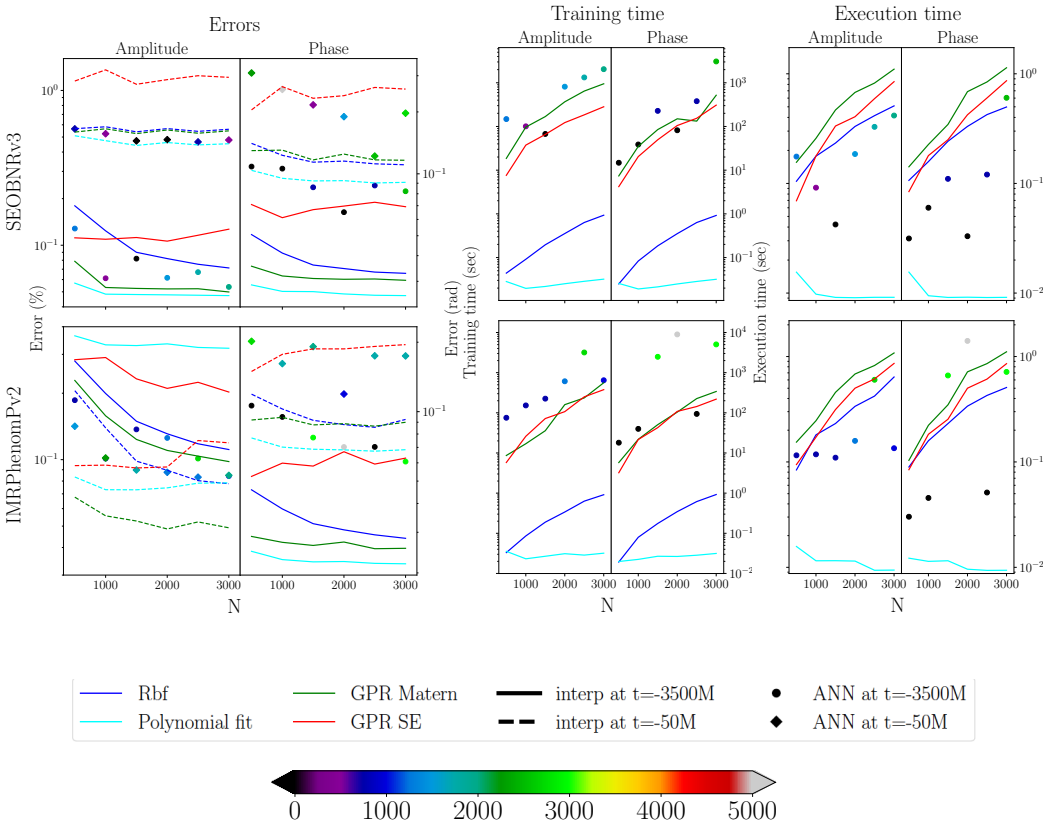

Figure II.5: The seven-dimensional interpolation results. Top: `SEOBNRv3`*, bottom:* `IMRPhenomPv2`*. The x-axes show the number of training points N and the y-axes shows the errors, training, and execution time as shown on the plot. Left: errors of the amplitude ($A(t)$) and phase ($\phi(t)$) respectively, middle: training time in unit seconds, and right: execution time in unit seconds. The solid lines show the results at $t = -3500M$ and the dashed lines for $t = -50M$. Different colors represent different interpolation methods as shown in the shared legend. The colored circles correspond to the results of ANN at $t = -3500M$ and the colored diamonds for $t = -50M$. Different colors represent a different number of neurons on a double layer ANN as shown in the corresponding color bar.*

Methods	Advantages	Disadvantages	Training time
Linear (RGI)	standard `scipy`	needs regular grid	$O(N)$
TPI	robust and high accuracy	needs regular grid	$O(N^k)$
GMVP	irregular grid fast execution time	complex	#basis function #error tolerance
Polynomial fit	irregular grid simple and fast	Runge's phenomenon only univariate in `scipy`	$O(N)$ and #polynomial degree
RBF	`scipy` irregular grid	high computational complexity	$O(N^3)$
GPR	irregular grid can predict uncertainty	depends on the choice of kernel and hyperparameters complex	$O(N^3)$
ANN	irregular grid flexible architecture choices	complex	#neurons #hidden layers

Table II.1: Summary of features of the methods used in this study. We present the advantages, the disadvantages and the scaling complexity for each method. For linear interpolation, TPI, RBF, and GPR the (training time) depends on the number of training points N (and polynomial degree k). Other methods have different complexity scalings that affect their training time.

Bibliography

[1] LIGO: The laser interferometry gravitational wave detector;. https://www.ligo.caltech.edu.

[2] Virgo;. http://www.virgo-gw.eu.

[3] Abbott BP, et al. GWTC-1: A Gravitational-Wave Transient Catalog of Compact Binary Mergers Observed by LIGO and Virgo during the First and Second Observing Runs. Phys Rev X. 2019 Sep;9:031040. Available from: https://link.aps.org/doi/10.1103/PhysRevX.9.031040.

[4] LIGO third obesrerving time (O3);. https://dcc.ligo.org/public/0152/G1801056/004/G1801056-v4.pdf.

[5] Blanchet L. Gravitational Radiation from Post-Newtonian Sources and Inspiralling Compact Binaries. Living Reviews in Relativity. 2014 Feb;17. Available from: https://link.springer.com/article/10.12942/lrr-2014-2#aboutcontent.

[6] Campanelli M, Lousto CO, Marronetti P, Zlochower Y. Accurate Evolutions of Orbiting Black-Hole Binaries without Excision. Phys Rev Lett. 2006 Mar;96:111101. Available from: https://link.aps.org/doi/10.1103/PhysRevLett.96.111101.

[7] Pretorius F. Evolution of Binary Black-Hole Spacetimes. Phys Rev Lett. 2005 Sep;95:121101. Available from: https://link.aps.org/doi/10.1103/PhysRevLett.95.121101.

[8] Baker JG, Centrella J, Choi DI, Koppitz M, van Meter J. Gravitational-Wave Extraction from an Inspiraling Configuration of Merging Black Holes. Phys Rev Lett. 2006 Mar;96:111102. Available from: https://link.aps.org/doi/10.1103/PhysRevLett.96.111102.

[9] Damour T. Coalescence of two spinning black holes: An effective one-body approach. Phys Rev D. 2001 Nov;64:124013. Available from: https://link.aps.org/doi/10.1103/PhysRevD.64.124013.

[10] Damour T, Jaranowski P, Schäfer G. Effective one body approach to the dynamics of two spinning black holes with next-to-leading order spin-orbit coupling. Phys Rev D. 2008 Jul;78:024009. Available from: https://link.aps.org/doi/10.1103/PhysRevD.78.024009.

[11] Babak S, Taracchini A, Buonanno A. Validating the effective-one-body model of spinning, precessing binary black holes against numerical relativity. Phys Rev D. 2017 Jan;95:024010. Available from: https://link.aps.org/doi/10.1103/PhysRevD.95.024010.

[12] Bohé A, et al. Improved effective-one-body model of spinning, nonprecessing binary black holes for the era of gravitational-wave astrophysics with advanced detectors. Phys Rev D. 2017 Feb;95:044028. Available from: https://link.aps.org/doi/10.1103/PhysRevD.95.044028.

[13] Santamaría L, Ohme F, Ajith P, Brügmann B, Dorband N, Hannam M, et al. Matching post-Newtonian and numerical relativity waveforms: Systematic errors and a new phenomenological model for nonprecessing black hole binaries. Phys Rev D. 2010 Sep;82:064016. Available from: https://link.aps.org/doi/10.1103/PhysRevD.82.064016.

[14] Khan S, Husa S, Hannam M, Ohme F, Pürrer M, Forteza XJ, et al. Frequency-domain gravitational waves from nonprecessing black-hole binaries. II. A phenomenological model for the advanced detector era. Phys Rev D. 2016 Feb;93:044007. Available from: https://link.aps.org/doi/10.1103/PhysRevD.93.044007.

[15] Hannam M, Husa S, González JA, Sperhake U, Brügmann B. Where post-Newtonian and numerical-relativity waveforms meet. Phys Rev D. 2008 Feb;77:044020. Available from: https://link.aps.org/doi/10.1103/PhysRevD.77.044020.

[16] Husa S, Khan S, Hannam M, Pürrer M, Ohme F, Forteza XJ, et al. Frequency-domain gravitational waves from nonprecessing black-hole binaries. I. New numerical waveforms and anatomy of the signal. Phys Rev D. 2016 Feb;93:044006. Available from: https://link.aps.org/doi/10.1103/PhysRevD.93.044006.

[17] Schmidt P, Hannam M, Husa S. Towards models of gravitational waveforms from generic binaries: A simple approximate mapping between precessing and nonprecessing inspiral signals. Phys Rev D. 2012 Nov;86:104063. Available from: https://link.aps.org/doi/10.1103/PhysRevD.86.104063.

[18] Hannam M, Schmidt P, Bohé A, Haegel L, Husa S, Ohme F, et al. Simple Model of Complete Precessing Black-Hole-Binary Gravitational Waveforms. Phys Rev Lett. 2014 Oct;113:151101. Available from: https://link.aps.org/doi/10.1103/PhysRevLett.113.151101.

[19] Blackman J, Field SE, Galley CR, Szilágyi B, Scheel MA, Tiglio M, et al. Fast and Accurate Prediction of Numerical Relativity Waveforms from Binary Black Hole Coalescences Using Surrogate Models. Phys Rev Lett. 2015 Sep;115:121102. Available from: https://link.aps.org/doi/10.1103/PhysRevLett.115.121102.

[20] Blackman J, et al. Numerical relativity waveform surrogate model for generically precessing binary black hole mergers. Phys Rev D. 2017 Jul;96:024058. Available from: https://link.aps.org/doi/10.1103/PhysRevD.96.024058.

[21] Doctor Z, Farr B, Holz DE, Pürrer M. Statistical gravitational waveform models: What to simulate next? Phys Rev D. 2017 Dec;96:123011. Available from: https://link.aps.org/doi/10.1103/PhysRevD.96.123011.

[22] Varma V, Field SE, Scheel MA, Blackman J, Kidder LE, Pfeiffer HP. Surrogate model of hybridized numerical relativity binary black hole waveforms. Phys Rev D. 2019 Mar;99:064045. Available from: https://link.aps.org/doi/10.1103/PhysRevD.99.064045.

[23] Pürrer M. Frequency-domain reduced order models for gravitational waves from aligned-spin compact binaries. Classical and Quantum Gravity. 2014 September;31:195010. Available from: http://iopscience.iop.org/article/10.1088/0264-9381/31/19/195010/pdf.

[24] Pürrer M. Frequency domain reduced order model of aligned-spin effective-one-body waveforms with generic mass ratios and spins. Phys Rev D. 2016 Mar;93:064041. Available from: https://link.aps.org/doi/10.1103/PhysRevD.93.064041.

[25] Abbott BP, et al. GW150914: First results from the search for binary black hole coalescence with Advanced LIGO. Phys Rev D. 2016 Jun;93:122003. Available from: https://link.aps.org/doi/10.1103/PhysRevD.93.122003.

[26] Veitch J, et al. Parameter estimation for compact binaries with ground-based gravitational-wave observations using the LALInference software library. Phys Rev D. 2015 Feb;91:042003. Available from: https://link.aps.org/doi/10.1103/PhysRevD.91.042003.

[27] Veitch J, Mandel I, Aylott B, Farr B, Raymond V, Rodriguez C, et al. Estimating parameters of coalescing compact binaries with proposed advanced

detector networks. Phys Rev D. 2012 May;85:104045. Available from: https://link.aps.org/doi/10.1103/PhysRevD.85.104045.

[28] Field SE, Galley CR, Hesthaven JS, Kaye J, Tiglio M. Fast Prediction and Evaluation of Gravitational Waveforms Using Surrogate Models. Phys Rev X. 2014 Jul;4:031006. Available from: https://link.aps.org/doi/10.1103/PhysRevX.4.031006.

[29] Blackman J, et al. A Surrogate model of gravitational waveforms from numerical relativity simulations of precessing binary black hole mergers. Phys Rev D. 2017 May;95:104023. Available from: https://link.aps.org/doi/10.1103/PhysRevD.95.104023.

[30] Setyawati Y, Ohme F, Khan S. Enhancing gravitational waveform models through dynamic calibration. Phys Rev D. 2019 Jan;99:024010. Available from: https://link.aps.org/doi/10.1103/PhysRevD.99.024010.

[31] London L, Fauchon-Jones E. On modeling for Kerr black holes: Basis learning, QNM frequencies, and spherical-spheroidal mixing coefficients; 2018. arXiv 1810.03550.

[32] Lackey B, Pürrer M, Taracchini A, Marsat S. Surrogate model for an aligned-spin effective one body waveform model of binary neutron star inspirals using Gaussian process regression; 2018. arXiv 1812.08643.

[33] Buonanno A, Pan Y, Pfeiffer HP, Scheel MA, Buchman LT, Kidder LE. Effective-one-body waveforms calibrated to numerical relativity simulations: Coalescence of nonspinning, equal-mass black holes. Phys Rev D. 2009 Jun;79:124028. Available from: https://link.aps.org/doi/10.1103/PhysRevD.79.124028.

[34] Vinciguerra S, Veitch J, Mandel I. Accelerating gravitational wave parameter estimation with multi-band template interpolation. Classical and Quantum Gravity. 2017 May;34:115006. Available from: https://iopscience.iop.org/article/10.1088/1361-6382/aa6d44.

[35] Rebei A, A H, Wang S, Habib S, Haas R, Johnson D, et al.. Fusing numerical relativity and deep learning to detect higher-order multipole waveforms from eccentric binary black hole mergers; 2018. arXiv 1807.09787.

[36] Chua AJK, Galley CR, Vallisneri M. Reduced-Order Modeling with Artificial Neurons for Gravitational-Wave Inference. Phys Rev Lett. 2019 May;122:211101. Available from: https://link.aps.org/doi/10.1103/PhysRevLett.122.211101.

[37] Collaboration TLS. LIGO instrument white paper: LIGO A+, Cosmic Explorer and Voyager; 2018. https://dcc.ligo.org/LIGO-T1500290/public.

[38] KAGRA;. https://gwcenter.icrr.u-tokyo.ac.jp/en/.

[39] LISA;. https://lisa.nasa.gov.

[40] Einstein Telescope;. http://www.et-gw.eu.

[41] Cosmic Explorer;. https://cosmicexplorer.org.

[42] Pan Y, Buonanno A, Taracchini A, Kidder LE, Mroué AH, Pfeiffer HP, et al. Inspiral-merger-ringdown waveforms of spinning, precessing black-hole binaries in the effective-one-body formalism. Phys Rev D. 2014;89(8):084006.

[43] Taracchini A, et al. Effective-one-body model for black-hole binaries with generic mass ratios and spins. Phys Rev D. 2014;89(6):061502.

[44] Golub GH, Van Loan CF. Matrix Computations (3rd ed.). Johns Hopkins; 1996.

[45] Demmel JW. Applied Numerical Linear Algebra. SIAM; 1997.

[46] Boyle M. Angular velocity of gravitational radiation from precessing binaries and the corotating frame. Phys Rev. 2013;D87(10):104006.

[47] Boyle M. GWFrames. GitHub; 2019. https://github.com/moble/GWFrames.

[48] Boyle M, Owen R, Pfeiffer HP. A geometric approach to the precession of compact binaries. Phys Rev. 2011;D84:124011.

[49] Wigner EP. Group theory and its application to the quantum mechanics of atomic spectra. Academic Press, Inc.; 1959.

[50] Garrido JM. Introduction to Computational Models with Python. vol. 1. 1st ed. Chapman and Hall/CRC; 2015.

[51] Regular grid interpolator;. https://pypi.org/project/regulargrid/.

[52] Scipy RGI;. https://docs.scipy.org/doc/scipy-0.16.0/reference/generated/scipy.interpolate.RegularGridInterpolator.html.

[53] Birkes D, Dodge Y. Alternative Methods of Regression. 1st ed. 605 Third Avenue, New York: John Wiley and Sons, Inc; 1993.

[54] Hastie T, Tibshirani R, Wainwright M. Statistical Learning with Sparsity: The Lasso and Generalizations. 1st ed. 6000 Broken Sound Parkway NW, Suite 300: CRC Press; 2015.

[55] Wakefield J. Bayesian and Frequentist Regression Methods. Springer Series in Statistics. Springer New York; 2013. Available from: https://books.google.de/books?id=0UJEAAAAQBAJ.

[56] de Boor C. A Practical Guide to Splines. Springer; 2001.

[57] Boyd JP. Chebyshev and Fourier Spectral Methods. Dover Publications, Inc.; 2000.

[58] Canuto C, Hussaini MY, Quarteroni A, Zang TA. Spectral Methods, Fundamentals in Single Domains. Springer; 2006.

[59] Quarteroni A, Sacco R, Saleri F. Numerical Mathematics. Springer; 2000.

[60] Lackey BD, Bernuzzi S, Galley CR, Meidam J, Van Den Broeck C. Effective-one-body waveforms for binary neutron stars using surrogate models. Phys Rev. 2017;D95(10):104036.

[61] Cython: C-Extensions for Python;. http://cython.org/.

[62] Pürrer M, Blackman J. Tensor Product Interpolation Package for Python (TPI). GitHub; 2018. https://github.com/mpuerrer/TPI.

[63] Phillips GM. Interpolation and Approximation by Polynomials. 1st ed. Clarkson Rd, Chesterfield: Springer Science+Business Media New York; 2003.

[64] Quarteroni A, Sacco R, Saleri F. Numerical Mathematics. vol. 1 of 10. 2nd ed. Springer-Verlag Berlin Heidelberg: Springer, Berlin, Heidelberg; 2007.

[65] Press W, Flannery B, Teukolsky S, Vetterling W. Numerical Recipes in C: The Art of Scientific Computing, Second Edition. vol. 1. 2nd ed. Cambridge University Press; 1992.

[66] rompy;. https://bitbucket.org/chadgalley/rompy/src/master/.

[67] Field SE, Galley CR, Herrmann F, Hesthaven JS, Ochsner E, Tiglio M. Reduced basis catalogs for gravitational wave templates. Phys Rev Lett. 2011;106:221102.

[68] Buhmann MD. Radial Basis Function: Theory and Implementaions. The Pitt Building, Trumpington Street, Cambridge, United Kingdom: Cambridge University Press; 2004.

[69] Roussos G, Baxter B. Rapid evaluation of radial basis functions. Journal of Computational and Applied Mathematics. 2005;180:51–70.

[70] Scipy RBF;. https://docs.scipy.org/doc/scipy/reference/generated/scipy.interpolate.Rbf.html.

[71] Rasmussen C, Williams C. Gaussian Processes for Machine Learning. The MIT Press; 2006.

[72] Pedregosa F, Varoquaux G, Gramfort A, Michel V, Thirion B, Grisel O, et al. Scikit-learn: Machine Learning in Python. Journal of Machine Learning Research. 2011;12:2825–2830.

[73] Rasmussen C, Williams C. Gaussian Processes for Regression. Advances in Neural Information Processing Systems. 1996;p. 514–520.

[74] Jackson JE. A User's Guide to Principal Components. vol. 1 of 1. 3rd ed. 222 Rosewood Drive, Danvers, MA 01923: Wiley-Interscience; 2003.

[75] Abramowitz M, Stegun I. Handbook of mathematical functions. Dover Publications; 1965.

[76] Egmont-Petersen M, de Ridder D, Handels H. Image processing with neural networks: a review. Pattern Recognition. 2002;35(10):2279–2301.

[77] Zhang G, Patuwo BE, Hu MY. Forecasting With Artificial Neural Networks: The State of the Art. International Journal of Forecasting. 1998;14(1):35–62.

[78] Abiodun O, Jantan A, Omolara A, Dada K, Mohamed N, Arshad H. State-of-the-art in artificial neural network applications: A survey. International Journal of Forecasting. 2018;4(11).

[79] Goodfellow I, Bengio Y, Courville A. Deep Learning. MIT Press: Cambridge University Press; 2017.

[80] Hornik K, Stinchcombe M, White H. Multilayer feedforward networks are universal approximators. Neural Networks. 1989;2(5):359–366.

[81] Orr MJL. Introduction to Radial basis function networks. EH 9LW, Scotland, UK; 1996.

[82] Sonoda S, Murata N. Neural Network with Unbounded Activation Functions is Universal Approximator. Applied and Computational Harmonic Analysis. 2017;43,(2):233–268.

[83] Glorot X, Bordes A, Bengio Y. Deep Sparse Rectifier Neural Networks. Journal of Machine Learning Research. 2011;15. Available from: http://proceedings.mlr.press/v15/glorot11a/glorot11a.pdf.

[84] Chollet F, et al.. Keras; 2015. https://keras.io.

[85] da Silva IN, Spatti DH, Flauzino RA, Liboni LHB, dos Reis Alves SF. Artificial Neural Networks: A Practical Course . 1st ed. Springer International Publishing AG Switzerland; 2017.

[86] Kingma D, Ba J. Adam: a methods for stochastic optimization; 2017. arXiv 1412.6980.

[87] An Open Source Machine Learning Framework for Everyone: tensorflow/tensorflow v1.14.0; 2019. https://github.com/tensorflow/tensorflow/releases/tag/v1.14.0.

[88] Heaton J. Introduction to Neural Networks with Java. 2nd ed. Clarkson Rd, Chesterfield: Heaton Research, Inc; 2008.

III

Adding eccentricity to quasicircular binary-black-hole waveform models

Yoshinta Setyawati[1,2,3], Frank Ohme[1,2]

[1]Max Planck Institute for Gravitational Physics (Albert Einstein Institute), Callinstrß 38, 30167 Hannover, Germany
[2]Leibniz Universität Hannover, 30167 Hannover, Germany
[3]Institute for Gravitational and Subatomic Physics (GRASP) Department of Physics, Utrecht University, Princetonplein 1, 3584 CC Utrecht, The Netherlands

Abstract

The detection of gravitational-wave signals from coalescing eccentric binary black holes would yield unprecedented information about the formation and evolution of compact binaries in specific scenarios, such as dynamical formation in dense stellar clusters and three-body interactions. The gravitational-wave searches by the ground-based interferometers, LIGO and Virgo, rely on analytical waveform models for binaries on quasicircular orbits. Eccentric merger waveform models are less developed, and only a few numerical simulations of eccentric mergers are publicly available, but several eccentric inspiral models have been developed from the post-Newtonian expansion. Here we present a novel method to convert the dominant quadrupolar mode of any circular analytical binary-black-hole model into an eccentric model. First, using numerical simulations, we examine

the additional amplitude and frequency modulations of eccentric signals that are not present in their circular counterparts. Subsequently, we identify suitable analytical descriptions of those modulations and interpolate key parameters from twelve numerical simulations designated as our training dataset. This allows us to reconstruct the modulated amplitude and phase of any waveform up to mass ratio 3 and eccentricity 0.2. We find that the minimum overlap of the new model with numerical simulations is around 0.98 over all of our test dataset that are scaled to a $50M_{\odot}$ black-hole binary starting at 35 Hz with aLIGO A+ design sensitivity. A Python package `pyrex` easily carries out the computation of this method.

Author's contribution

YS initiated the research idea, design of the study, the development of the theory, and performed all the computations. FO supervised the findings and the analysis of this work. Furthermore, YS wrote most of the manuscript.

Copyright Notice

III.1 Introduction

Coalescing stellar-mass black-hole binaries are one of the primary sources of GW signals detected by the ground-based interferometers, the aLIGO [1], Virgo [2], and KAGRA [3]. In the first three observing runs (O1–O3), detection pipelines assumed BBH mergers to have negligible eccentricity when entering the orbital frequencies to which aLIGO, Virgo, and KAGRA are sensitive [4, 5, 6]. BBHs formed in an isolated environment through a massive stellar evolution are expected to circularize and therefore have undetectable eccentricity by the time they enter the LIGO band [7]. However, BBHs with a detectable eccentricity can form in a dense stellar cluster through dynamical capture [8, 9].

A possible scenario is that the binary gains eccentricity due to gravitational torques exchanged with a circumbinary disk [10]. Eccentric BBHs can also form from three-body interactions [9], where the BBH behaves as the inner binary. In this system, the Kozai-Lidov [11, 12] mechanism triggers the oscillation that boosts the eccentricity.

Interactions of BBHs in a typical globular cluster suggest a significant eccentric BBH merger rate. As many as $\sim$ 5% of binaries may enter the LIGO detector band ($f \geq 10$ Hz) with eccentricities $e > 0.1$ [13, 14, 15]. A confident measurement of significant eccentricity in a BBH system would be strong evidence for the dynamical formation scenarios in dense stellar clusters and would boost our understanding of the dynamical evolution of compact objects.

The impact of eccentricity is more substantial during the early inspiral and therefore plays a vital role in the space-based detector era [16]. In the LIGO band, the detection of GWs from an eccentric orbit would suggest that the binary was formed with a small initial separation and did not have time to circularize, or the binary evolved through an unknown dynamical process. Incorporating eccentric BBH simulations may also lead to an increase in the LIGO/Virgo/KAGRA detection rate [14]. Besides, the detection of eccentric BBH mergers could capture effects from the extreme-gravity regime and therefore can be used for testing the general theory of relativity [17, 18].

We highlight the significance of detecting GWs from eccentric BBHs. Constructing template models for eccentric waveforms is challenging, and we aim to make progress towards this goal especially for the late inspiral and merger regimes that are most accessible with today's observations. One of the main difficulties in developing an eccentric waveform model is that only a few NR simulations with higher eccentricity are available. Thus, many studies focus on developing eccentric models from the PN expansion. The development of full IMR eccentric waveform models is currently an actively researched area [19, 20, 21].

Huerta *et* al. [19] construct a time-domain eccentric nonspinning waveform

model ($e_0 < 0.2$) up to mass ratio 5.5, where e_0 is the eccentricity 10 cycles before the merger. Their model is called `ENIGMA`, a hybrid waveform that has been calibrated using a set of numerical simulations and trained using GPR. Reference [20] presents a low-eccentricity model ($e_0 < 0.2$) called `SEOBNRE` using the expansion of the EOB waveform family. A more up-to-date EOB formalism is demonstrated in Refs. [22, 23]. Hinder *et* al. [21] present a time-domain, nonspinning eccentric waveform model up to mass ratio $q = m_1/m_2 = 3$ from 23 NR simulations that are publicly available in the SXS catalog. The referenced eccentricity is $e_{\rm ref} \leq 0.08$ starting at seven cycles before the merger. Like Ref. [19], the early inspiral of this model is hybridized with a PN expansion to produce a full IMR model in a *Mathematica* package [24]. In addition, Ref. [25] recently developed an eccentric model `NRSur2dq1Ecc` for nonspinning waveforms and eccentricities up to 0.2 from 47 NR simulations. Although the model was trained for $q = 1$, it can be extended to mass ratio $q \approx 3$. Apart from the studies above, nonspinning, low-eccentricity frequency-domain models from the PN expansion are publicly available in the LAL [26, 27, 28].

The excitement to search for an eccentric BBH motivated the following analysis. References [29, 30, 31] recently developed an analysis to find the signature of an eccentric BBH in the O1, O2 and several events in the O3 data using the `SEOBNRE` model. Additionally, Ref. [32] analyzed the heaviest BBH system during O1–O3, GW190521 [33] with 325 NR simulations. They found that this event is consistent with highly precessing, eccentric model with $e \approx 0.7$.

We present a promising method to add eccentricity to quasicircular systems independent of the PN expansion. We apply this method to nonspinning, time-domain waveforms, although in principle it can be used in more general settings. Our technique focuses on a fast reconstruction of the near-merger eccentric BBH waveform and can be applied to any analytical circular nonspinning model. We build our model from 12 NR simulations and test against further 8 NR simulations from the open SXS catalog [34]. Our method is very simple and can be applied to *any* circular time-domain model obtained from, e.g., the phenomenological [35, 36, 37] or EOB [38, 39] families.

We model the deviation from circularity visible in the amplitude and phase of eccentric GW signals. This deviation is modeled across the parameter space and can be simply added to any quasicircular model, which elevates that model to include eccentric effects. This approach is inspired by the "twisting" technique that is applied for reconstructing precessing spins from an aligned-spin model to build, e.g., the `IMRPhenomP` family [36, 40, 41, 42, 43]. The dynamic calibration of the waveform model is motivated by our previous study [44] and the regression techniques tested in detail in Ref. [45].

We calibrate our model for mass ratios $q \leq 3$ and eccentricity $e \leq 0.2$, and provide it as a Python package called `pyrex` [46]. Our model has been constructed

for a fiducial 50 $M_\odot$ BBH and can then be rescaled for other total masses M. We find that the overlap of all our test data against NR is above 98%. Moreover, we expand the construction to earlier regimes than the calibrated time span. Although we do not calibrate for higher mass ratios, the early inspiral, or higher orbital eccentricity, we allow the building of waveforms beyond the parameter boundaries used for calibration.

The organization of this manuscript is as follows: In Sec. III, we present the methodology to construct this model. Section III discusses the primary outcome and the faithfulness of our model. Finally, Sec. III summarizes and concludes the prospect of our studies. Throughout this article, we use geometric units in which $G = c = 1$.

III.2 Method

Using NR simulations, we investigate the frequency and amplitude modulations in eccentric BBH signals and implement them in analytical waveforms to develop our model. As described by Peters [7], the orbital eccentricity in binary systems decreases over time due to energy loss through GW radiation. Pfeiffer *et* al. [47] investigated this in numerical simulations of the SXS catalog. The authors point out that one of the main differences in the evolution of low-eccentricity initial data compared to quasicircular binaries is an overall time and phase shift, where the quasicircular data represent the binary at a point close to merger. Following these studies, Hinder et al. [21] showed that the GW emissions from low-eccentric binaries and circular binaries are indistinguishable near the merger stage. Specifically, Hinder *et* al. suggest that one only loses 4% of the signal when substituting the GW emission from low-eccentricity binaries with circular orbits $30M$ before the peak of the amplitude ($t = 0$). They use this fact to build an eccentric IMR model by replacing the late inspiral eccentric model with a circular waveform. Combining the finding above, we model the decaying eccentricity as amplitude and phase modulation up to $t = -29M$. We then substitute the GW strain at $t > -29M$ with the circular model for the same binary masses.

III.2.1 Data preparation

We use 20 nonspinning NR simulations from the SXS catalog up to mass ratio 3 and eccentricity 0.2 to build our model (see Table III.1). We follow the definition of eccentricity $e_{\rm comm}$ in Ref. [21] as the eccentricity measured at the referenced frequency, $x = (M\omega)^{2/3} = 0.075$. These simulations are divided into a training data set of 12 simulations and the test datasets of 8 simulations, as shown in Fig. III.1. Binaries of the test dataset fall within the training data's parameter boundaries.

Hence, we do not perform extrapolation with the test data.

We combine the "+" and "×" polarization using the spin-weighted spherical harmonics with the following expression [48]:

$$h_+ - ih_\times = \frac{M}{r} \sum_{\ell=2}^{\infty} \sum_{m=-\ell}^{m=\ell} h_{\ell m}(t)\ {}^{-2}Y_{\ell m}(\iota, \phi), \tag{III.1}$$

where M and r are the total mass of the system and the distance from the observer, respectively; ${}^{-2}Y_{\ell m}$ are the spin-weighted spherical harmonics that depend on the inclination angle ι and the phase angle ϕ; and $h_{\ell m}(t)$ can be extracted from the NR data in the corresponding catalog. We construct our model for $h_{2\pm2}$, the leading contribution of spherical harmonic modes with $\ell = 2$, $m = \pm2$. Reference [21] suggests that other, subdominant modes are less significant for nearly equal-mass systems with low eccentricity. Here we consider only moderately small eccentricities; therefore we only model the dominant mode. For future studies, subdominant harmonics will be important to model high-eccentricity signals accurately.

We prepare the data as follows. First, we align all the waveforms in the time domain such that the peak amplitude is at $t = 0$. Subsequently, we remove the first $250M$ from the start of the waveforms due to the junk radiation, and the last $29M$ before $t = 0$ due to circularization (see Fig. III.2). Later, we use a circular waveform for $t > -29M$. We then decompose $h_{2\pm2}$ into amplitude ($\mathcal{A}$), phase (Ψ), and the phase derivative, $\omega = \frac{d\Psi}{dt}$, where the referenced frequency follows Ref [21].

We model amplitude $\mathcal{A}_{22}$ and frequency (ω_{22}) as a simple quasicircular piece plus an oscillatory function. The final model then yields the phase (Ψ_{22}) by integrating the frequency.

III.2.2 Eccentricity estimator

In numerical simulations, eccentricity is often discussed as a consequence of imperfections in the initial data [49]. It manifests itself as small oscillations on top of the gradual binary evolution, where the oscillation's amplitude is proportional to the eccentricity (see $\mathcal{A}_{22}$ and ω_{22} plots in Figs. III.2 and III.3). We use this residual oscillation as a key to estimating the eccentricity evolution.

Mroué *et* al. [50] compare various methods to estimate eccentricity using $e_{\rm X}(t)$. The orbital eccentricity is proportional to the amplitude of a sinusoidal function, $e_{\rm X}(t)$, expressed by

$$\begin{aligned} e_X(t) &= \frac{X_{\rm NR}(t) - X_{\rm c}(t)}{2X_{\rm c}(t)}, \\ \Leftrightarrow e_X(X_c) &= \frac{X_{\rm NR}(X_c) - X_{\rm c}}{2X_{\rm c}}, \end{aligned} \tag{III.2}$$

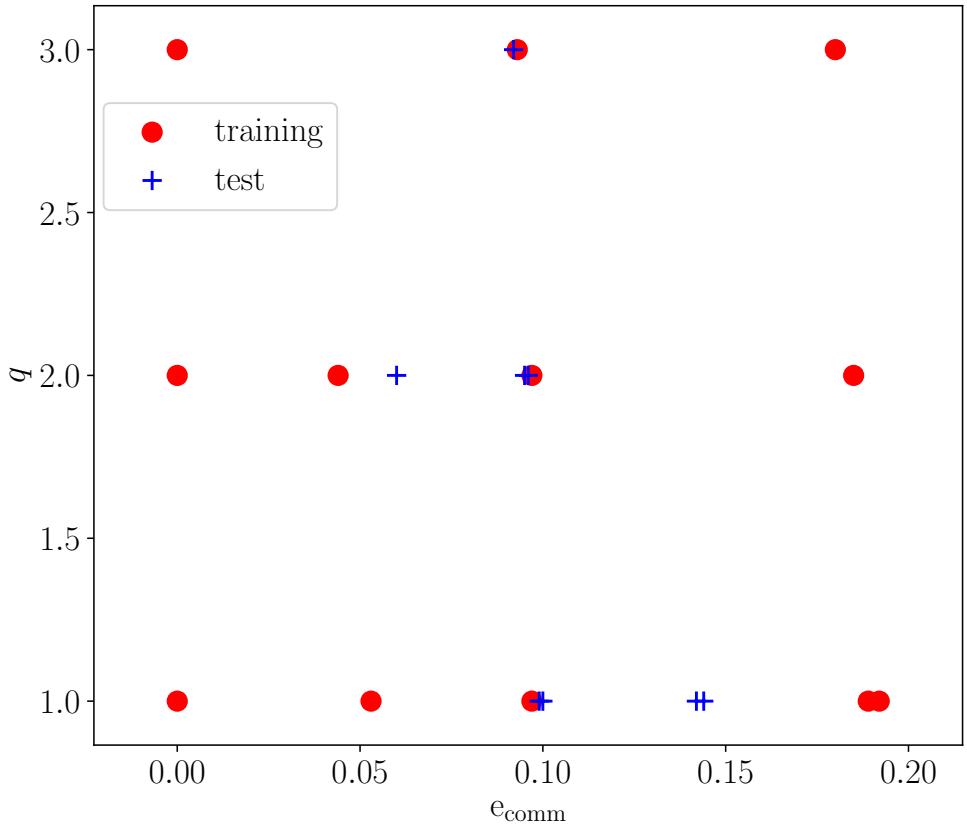

Figure III.1: The training and test data, shown by the red circles and the blue plus signs, are located in the parameter space of mass ratio and eccentricity. We use 20 NR simulations from the SXS catalog and divide them into 12 NR training datasets and 8 test datasets.

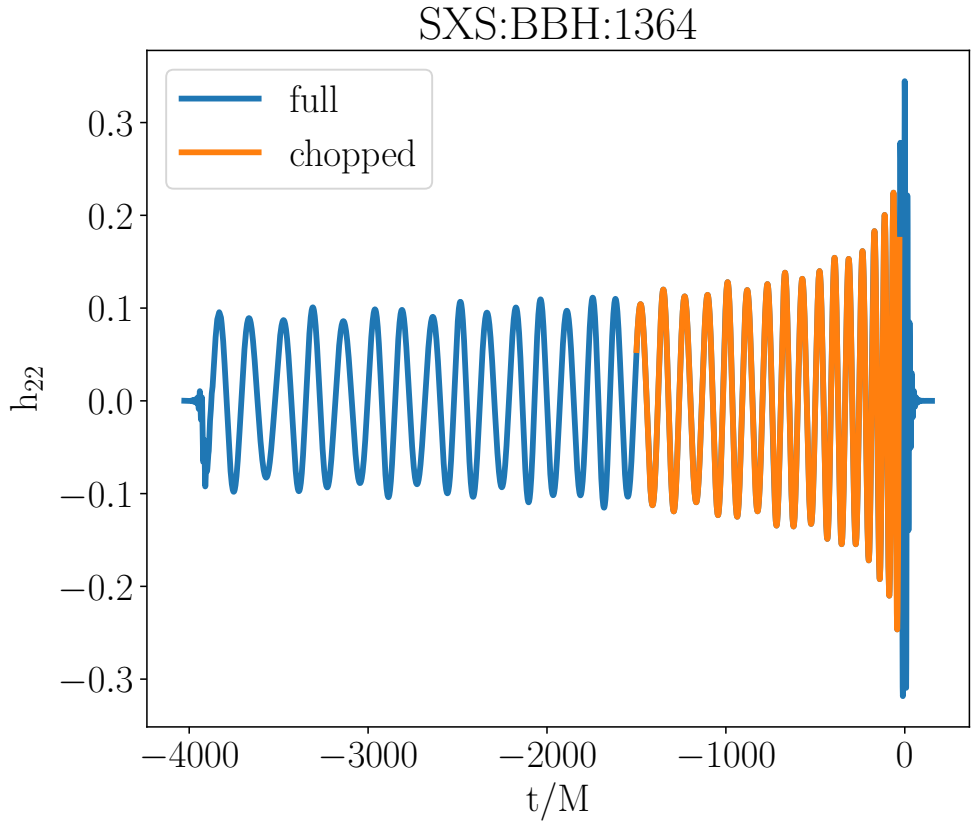

Figure III.2: The full and the chopped waveform of the SXS:BBH:1364 simulation ($q = 2, e_{comm} = 0.044$). The blue line shows the full NR h_{22} mode, and the orange line presents the time range used in this study. We remove the first $250M$ due to the junk radiation and modulate the residual oscillation at $-1500M \leq t \leq -29M$.

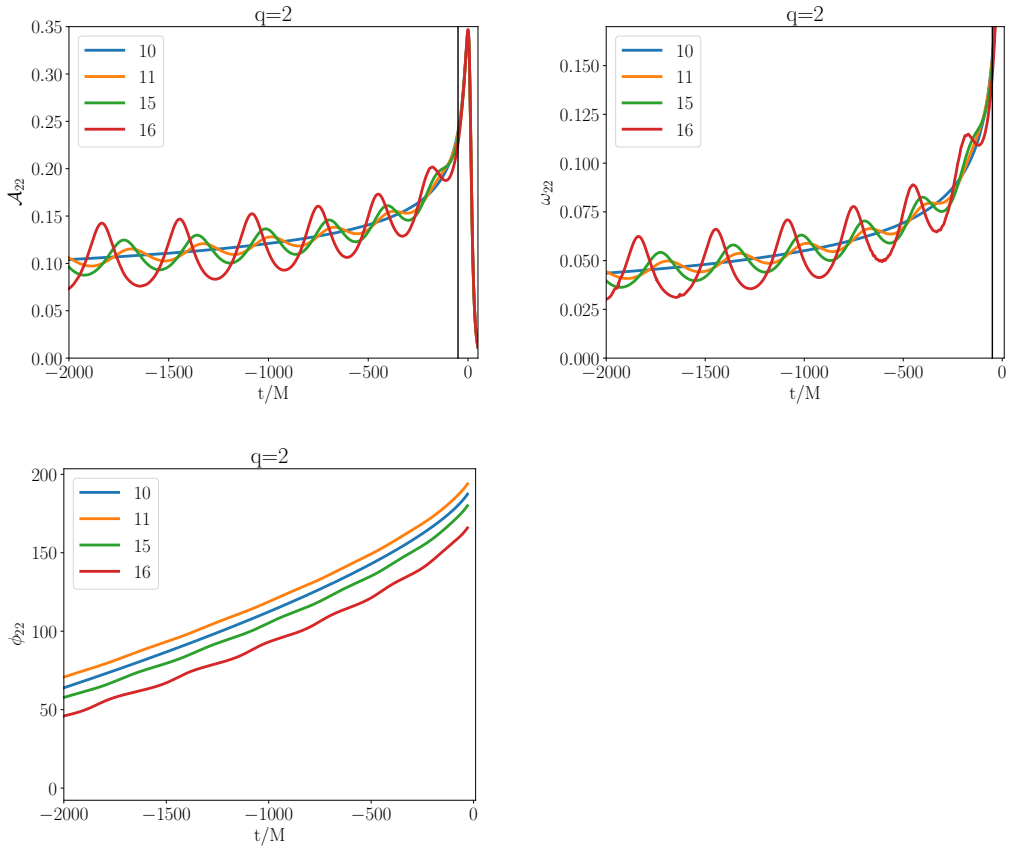

Figure III.3: The top-left panel shows the amplitude, the top-right panel shows the time derivative of the phase $\omega_{22} = d\Psi_{22}/dt$, and the bottom panel shows the phase of h_{22}. We present the key parameters from the training dataset for $q = 2$ ($\ell = 2, m = 2$). The numbers in the legend correspond to the case numbers of the simulations shown in Table III.1. Although higher-eccentricity waveforms produce more oscillations than the lower-eccentricity waveforms, all data appear identical at $t > -30M$ due to circularization as shown in the top panels. We employ the residual amplitude $\mathcal{A}_{22}$ and frequency ω_{22} to develop our model in the late inspiral regime.

Table III.1: NR simulations from the SXS catalog used in this study with mass ratio $q = m_1/m_2$, eccentricity at the reference frequency e_{comm}, and the number of orbits before the maximum amplitude of $\|h_{22}\|$. e_{comm} is the eccentricity at the reference frequency $(M\omega)^{2/3} = 0.075$ as described in Ref. [21]. The quasicircular waveforms ($e_{comm} = 0.000$) have eccentricities lower than 10^{-5} at the reference frequency.

Case	Simulations	Training/test	q	$e_{\rm comm}$	$N_{\rm orbs}$
1	SXS:BBH:0180	Training	1	0.000	26.7
2	SXS:BBH:1355	Training	1	0.053	11.9
3	SXS:BBH:1357	Training	1	0.097	12.8
4	SXS:BBH:1358	Test	1	0.099	12.1
5	SXS:BBH:1359	Test	1	0.100	11.7
6	SXS:BBH:1360	Test	1	0.142	11.1
7	SXS:BBH:1361	Test	1	0.144	10.9
8	SXS:BBH:1362	Training	1	0.189	10.2
9	SXS:BBH:1363	Training	1	0.192	10.1
10	SXS:BBH:0184	Training	2	0.000	13.7
11	SXS:BBH:1364	Training	2	0.044	14.2
12	SXS:BBH:1365	Test	2	0.060	14.1
13	SXS:BBH:1366	Test	2	0.095	13.6
14	SXS:BBH:1367	Test	2	0.096	13.6
15	SXS:BBH:1368	Training	2	0.097	13.6
16	SXS:BBH:1369	Training	2	0.185	13.6
17	SXS:BBH:0183	Training	3	0.000	13.5
18	SXS:BBH:1372	Test	3	0.092	15.6
19	SXS:BBH:1373	Training	3	0.093	15.3
20	SXS:BBH:1374	Training	3	0.180	13.5

where X is either ω_{22} or $\mathcal{A}_{22}$, and $X_{\rm c}(t)$ is the X quantity in circular binaries instead of low-order polynomial fitting functions that are often used in the literature. We reverse this relation to convert a circular model [with given $X_c(t)$] to an eccentric model using an analytical description of the oscillatory function $e_X(X_c)$. We apply the Savitzky-Golay filter [51] to smooth the $e_X(t)$ curves from noises caused by numerical artifacts. Savitzky-Golay is a digital filter applied to smooth the selected data points without altering the signal direction by fitting the adjacent data with a low-degree polynomial fit.

We stress that the definition of the orbital eccentricity is not unique. Thus, one could use different definitions of eccentricity. In principle, any definition can be accepted if consistently applied to the study in question. The NR data we use are labeled with a value for the initial eccentricity that is based on PN initial data [21]. As we shall discuss below, these labels are similar to what we estimate for the eccentricity using Eq. (III.2), but not identical. However, we refrain from redefi-

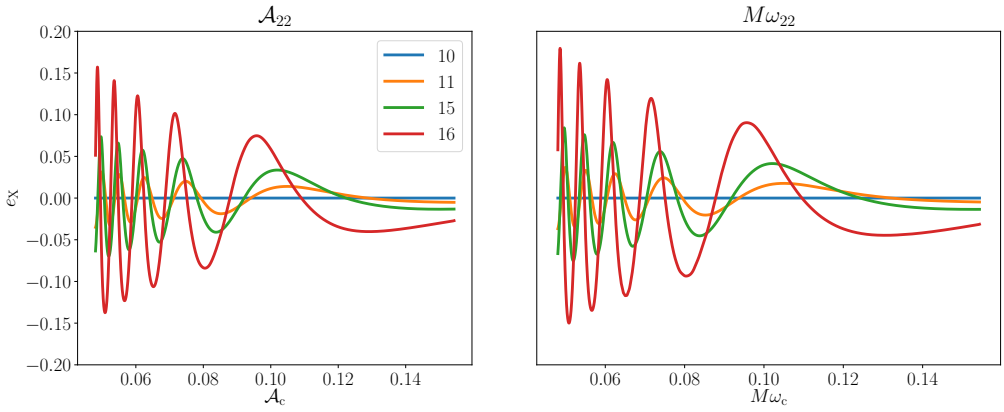

Figure III.4: The eccentricity estimator from $\mathcal{A}_{22}$ plotted against the circular amplitude $\mathcal{A}_c$ (left), and the eccentricity estimator from ω_{22} plotted against the circular omega ω_c (right) with the same mass ratio. Different colors show different cases of training data for mass ratio $q = 2$. We smooth the data from numerical artifacts using the Savitzky-Golay filter (see text).

nition of the initial eccentricity of the NR data and instead identify each NR simulation with the value of eccentricity at the reference frequency $(M\omega)^{2/3} = 0.075$ determined by the original Ref. [21]. We do this because (i) we want to avoid any confusion as to what NR data we are using and what their properties are, and (ii) by making the amplitude of e_X a function of the eccentricity label imposed by Ref. [21], we introduce an extra uncertainty that may be seen as representing the ambiguity in determining the initial eccentricity of the respected NR simulations. Thus, we present a conservative estimate of the approach's accuracy.

As a check, we compute the orbital eccentricity using the eccentricity estimator ($e_{\rm X}$) and find that the results agree with a maximum relative error of roughly 10% against $e_{\rm comm}$ quoted in the SXS catalog and given in Table. III.1. In Fig. III.4, we present the eccentricity estimator $e_{\rm X}(X_{\rm c})$ as a function of its circular amplitude and frequency, $\mathcal{A}_{\rm c}$ and $\omega_{\rm c}$, respectively.

III.2.3 Fitting $e_{\rm X}$

Our main goal is to model an eccentric waveform by modulating the amplitude and phase of a circular model. To construct the model, we interpolate the additional oscillation of an eccentric waveform depending on its eccentricity and mass ratio, where the relationship between the circular and the eccentric model is expressed in Eq. (III.2). Accordingly, we look for a fitting function to model $e_{\rm X}(X_{\rm c})$ that relies on the desired parameters (q, e) and reverse Eq. (III.2) to obtain the eccentric

amplitude and frequency. We then integrate the frequency to obtain the eccentric phase and construct the eccentric h_{22}.

We note that alternatives to fitting the amplitude and frequency modulations have been studied in Ref. [25]. In particular, they investigated using the phase residual instead of the frequency, or fitting the eccentric amplitude and phase (or frequency) directly instead of recasting the problem in terms of differences to noneccentric signals. Here we find that the most suitable strategy for our approach is to fit the residual amplitude and frequency oscillation defined as the eccentricity estimator ($e_{\rm X}$) that comes from $\{\mathcal{A}_{22}, \omega_{22}\}$ and integrate ω_{22} to obtain the phase (Ψ_{22}).

In a suitable parametrization, the eccentricity estimator $e_{\rm X}$ is a decaying sinusoidal function (see Fig. III.4) with its amplitude defined by the orbital eccentricity e [50]. To model $e_{\rm X}$ for various eccentricities and mass ratios, we fit $e_{\rm X}$ with a set of free parameters modifying a damped sinusoidal function. These parameters are two amplitude quantities (A and B), a frequency (f), and phase (φ) with the following relation:

$$e_{\rm X}(X_{\rm c}) = A e^{B X_c^{\kappa}} \sin(f\, X_c^{\kappa} + \varphi). \tag{III.3}$$

A, B, f, and φ are standard damped sinusoidal parameters obtained from the optimized curve fitting.

We use a X_c^{κ} instead of $X_{\rm c}$ to describe the evolution of the residual oscillations of the amplitude and frequency mainly for the following reasons: $X_{\rm c}$ is a rapidly evolving function. Therefore, it is more difficult to model e_X with a standard sinusoidal function with a constant frequency. Although it is in principle possible to use $X_{\rm c}$ directly in the model, we would have to slice the data into multiple small time windows that overlap. Thus, the results will be less smooth; one would have to blend all those individual functions defined on small intervals into one big function. Besides, we cannot guarantee our result beyond our calibration range, especially for the early inspiral. Using a power law allows us to fit the entire region with one set of free parameters. However, we note that the power law of $X_{\rm c}$ induces a twist resulting in infinitely large eccentricities for the very early inspiral stage. That is a problem with assuming exponential decay, and the fact that the power law we use has a negative exponent.

We fit our model $e_{\rm X}$ from the starting frequency $f_{\rm low} = 25\,{\rm Hz}$ for a circular BBH with a total mass $M = 50\,M_{\odot}$. The power law for ω_c is $\kappa = -59/24$, and for $\mathcal{A}_c$ it is $\kappa = -83/24$. We emphasize that these values are customized i.e., we expect that one might need different values to calibrate with higher eccentricity, a higher mass ratio, or a different starting frequency.

By optimizing the curve fit between $e_{\rm X}$ and Eq. III.3, we obtain the four quantities (A, B, f, φ) for all training data. The relation between the mass ratio (q), eccentricity (e), and the three parameters A, B, f is shown in Fig. III.5. The am-

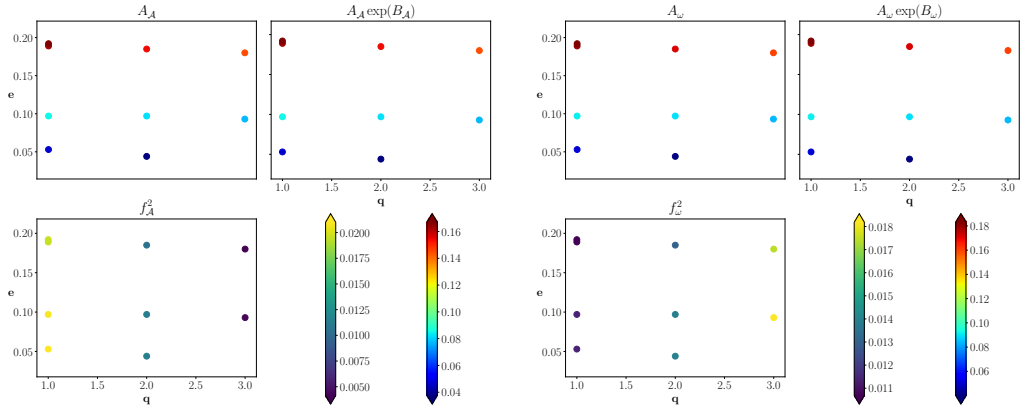

Figure III.5: Key quantities of $\mathcal{A}_{22}$ (left) and ω_{22} (right) of a damped sinusoidal function obtained from the curve fitting [see Eq. III.3]. The amplitude parameters (A and B) depend strongly on the eccentricity (e), whereas the square of the frequency (f^2) is correlated to the mass ratio (q). We leave φ as a free nuisance parameter that we maximize over when comparing to the test data. The left color bar corresponds to the bottom panel, and the right color bar to the top panel.

plitude components A and B are strongly correlated to eccentricity, whereas the mass ratio determines the frequency squared. Hence, we perform one-dimensional linear interpolation across eccentricity to obtain the values of A and B. Similar to that, we linearly interpolate f^2 across mass ratios. We choose f^2 instead of f because the data is smoother for interpolation. The square root of f^2 gives either positive or negative values. However, this ambiguity can be absorbed by the phase parameter φ.

The phase parameter φ is an additional degree of freedom that we cannot explore sufficiently with the available NR data. For small sets of NR simulations with nearly constant values of q and e, but varying ℓ, we find that the best-fit φ mirrors changes in ℓ. Thus, we expect that it may correlate strongly with the mean anomaly. Because the orientation of the ellipse is astrophysically less interesting than the value of the eccentricity, we do not attempt to model the effect of varying the mean anomaly other than introducing the phenomenological nuisance parameter φ. We interpolate the other parameters when generating a new waveform model with different mass ratios and referenced eccentricities.

We apply a one-dimensional interpolation for each key quantity shown in Fig. III.5. A and B are interpolated over different eccentricities e, f^2 is interpolated over the mass ratio q, and the phase of the oscillation φ can be chosen arbitrarily.

Once we obtain the eccentricity estimators $e_{\rm X}$ using the interpolated quantities, we substitute the results to reconstruct $\mathcal{A}_{22}$ and ω_{22} using Eq. III.2. To construct

Ψ_{22}, we integrate ω_{22} numerically using the trapezoidal rule. We truncate the waveform at $t = -50M$ and join it with the nonspinning circular model. We then smooth the transition with the Savitzky-Golay filter at $-46M < t < -25M$.

We then build $h_{2\pm2}$ as the combination of the amplitude and phase as follows:

$$h_{\ell m} = \mathcal{A}_{\ell m}\, e^{-i\Psi_{\ell m}}. \tag{III.4}$$

To reconstruct the gravitational-wave strain $h = h_+ - h_\times$, we compute the spin-weighted spherical harmonics $Y_{\ell m}(\iota, \phi)$ and employ Eq. III.1.

III.3 Results

We built a new nonspinning eccentric model by modulating the residual amplitude and phase oscillations of the circular analytical models, `IMRPhenomD` [35] and `SEOBNRv4` [52]. `IMRPhenomD` is an aligned-spin IMR model that was originally built in frequency domain and calibrated to numerical simulations for mass ratios $q \leq 18$. `SEOBNRv4` is an aligned-spin time-domain IMR model [52, 53] that has been calibrated to 140 NR waveforms produced with the SpEC code up to mass ratio 8 and extreme-mass-ratio signals.

As described in Sec. III, we interpolate the residual amplitude and phase oscillations of the training dataset for the given mass ratio and eccentricity. To construct a new, eccentric waveform for the intermediate to near-merger regime, we then use one of the nonspinning circular models with the desired mass ratio, compute the eccentricity estimators (e_X) from the analytical description given in Eq. (III.3), and reconstruct the desired eccentric waveform model for each test data. We develop a map from circular nonspinning waveforms to eccentric waveforms that can be applied to any analytical model with a relatively simple and fast function using only 20 NR simulations.

We evaluate the results by computing the overlap between the new model and the NR test data. The overlap is maximized over a time and phase shift, as well as the free phase offsets of the residual oscillations. Mathematically, we define the overlap O based on an inner product between two waveforms:

$$\langle h_1, h_2\rangle = 4\,\mathrm{Re}\int_{f_1}^{f_2} \frac{\tilde{h}_1(f)\,\tilde{h}_2^*(f)}{\mathrm{S_n}(f)}\mathrm{d}f, \tag{III.5}$$

$$O = \max_{\{t_0,\Psi_0,\varphi_{\mathcal{A}},\varphi_\omega\}} \frac{\langle h_1, h_2\rangle}{||h_1||||h_2||}, \tag{III.6}$$

where $\mathrm{S_n}$ is the sensitivity curve of the corresponding GW interferometer, $\tilde{h}(f)$ is the Fourier transform of $h(t)$, * denotes complex conjugation and $||h|| = \sqrt{\langle h, h\rangle}$.

The mismatch or unfaithfulness is defined by

$$\mathcal{M} = 1 - O. \tag{III.7}$$

We investigate three sensitivity curves for the future GW detectors, aLIGO A+, the Einstein Telescope (ET), and Cosmic Explorer (CE). LIGO A+ is the future GW interferometer with 1.7 times better sensitivity than the current detector, expected to start observing in mid-2024 at the earliest [54]. The ET is a 10 km GW observatory planned to be built on the border between Belgium, Germany, and Netherlands which could be operating in the mid-2030s [55]. The ET is expected to have higher sensitivity towards the low-frequency range. CE is a 40 km third-generation GW detector which has higher sensitivity towards low redshift ($z > 10$) that is planned to start observing in the 2030s [56]. Since our model focuses on the late inspiral case, and because the unfaithfulness is insensitive to a change in overall signal-to-noise ratio, the values obtained for the future third-generation detectors show similar behavior [57]. Hence, we only show the overlap results for the LIGO A+ design sensitivity. A possible caveat is that our model might not fill the LIGO A+ band down to 10 Hz. Thus, there is a chunk of inspiral power missing in the signal.

Figure III.6 visually compares the strain $h_{2\pm2}$ of each NR test dataset with the new eccentric nonspinning signal built from analytical models, `IMRPhenomD` and `SEOBNRv4` for a $50\,M_\odot$ BBH with inclination angle ι=0 (face-on) and phase of coalescence, ϕ_c=0. Using our method, we find that the minimum overlap between the new model and NR is ≈ 0.98 ($\log_{10}\mathcal{M} = -1.8$) over all of our test datasets. The minimum overlap occurs at the highest eccentricity in the test dataset.

Although we calibrated the new model for limited ranges in mass ratio, eccentricity, and time, we let the production of the new model go beyond our calibration range. In Fig. III.7, we show the unfaithfulness of the new model against the NR test data for various total masses with the aLIGO A+ design sensitivity curve. The left panel shows the unfaithfulness within the calibrated frequency range, between 25 Hz and the ISCO frequency scaled over the total mass. Similarly, the right panel presents the unfaithfulness beyond the calibrated frequency range, between 20 Hz and the ringdown frequency. We use the definitions of the ISCO and ringdown frequencies as follows:

$$f_{\rm ISCO} = 1/(6^{3/2}\pi M), \tag{III.8}$$

and

$$f_{\rm RD} = 0.1/M. \tag{III.9}$$

Figure III.7 shows that the mismatches decrease toward higher-total-mass systems. As the total mass increases, the overlap computation covers a smaller waveform regime towards merger in the frequency space. Since the eccentricity decreases over time, the near-merger regime has lower eccentricities. Thus, the

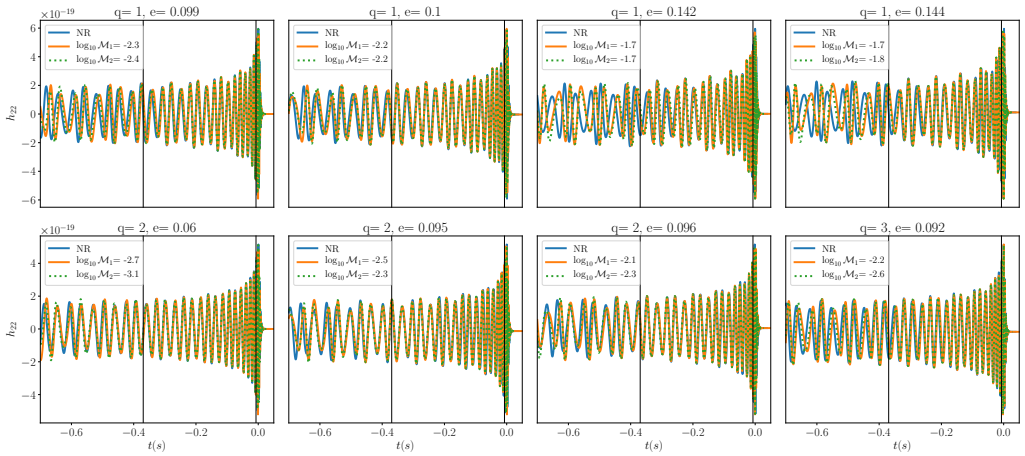

Figure III.6: `IMRPhenomD` *(orange) and* `SEOBNRv4` *(green) circular waveforms twisted into eccentric models.* $\log_{10}\mathcal{M}_1$ *is the log mismatch of* `IMRPhenomD` *against the NRs waveform (shown in blue), and* $\log_{10}\mathcal{M}_2$ *gives the log mismatch of* `SEOBNRv4` *against NR with the same mass ratio and eccentricity, respectively. The total mass of the system is* $M = 50M_\odot$*, and the mass ratio (q) and eccentricity (e) are shown in the title of each plot. We employ the A+ design sensitivity curve starting at* $f = 35\,Hz$ *(see text) to compute the match. The black vertical lines mark the range in which we perform the interpolation and compute the match.*

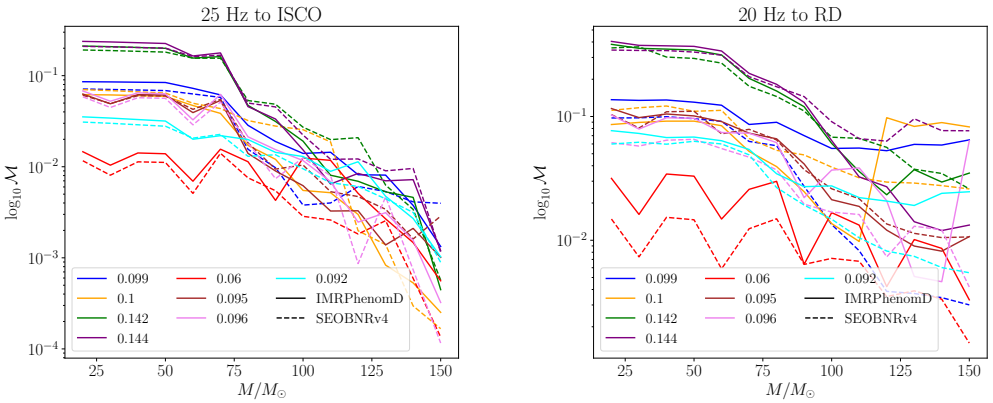

Figure III.7: Mismatch results of eccentric variants of `IMRPhenomD` *and* `SEOBNRv4` *against the NR test data for different total masses assuming aLIGO A+ design sensitivity. Left: 25 Hz to ISCO frequency (within the calibration range). Right: from 20 Hz to ringdown frequency (beyond the calibration range), where we define the ringdown frequency as* f_{RD}=0.1/M.

overlap between the model and the corresponding NR simulation is better for the higher-mass systems compared to the lower-mass ones. For comparison, we find that mismatches between circular analytical models and the eccentric NR test data are at least 1 order of magnitude worse than the results we find for our eccentric model.

The unfaithfulness between eccentric waveforms is better for {25, ISCO} than for {20, Ringdown}. We investigate the contribution weight between the early inspiral and the ringdown in the unfaithfulness results by comparing with the {25, Ringdown} and {20, ISCO} ranges. We argue that the mismatches for the low masses are dominated by the inspiral, whereas for high masses, the mismatches are dominated by the merger or ringdown. In the mismatch computation, we add padding in the ringdown area, but the early inspiral should come purely from the fitting data.

Furthermore, we test how well one can extract the parameters of an eccentric signal $h(q, e)$ by comparing with various waveforms with different eccentricities e and mass ratios q. We generate a `pyrex` waveform ($q = 1$, $e = 0.144$) and compare it with various other signal parameters (q, e) using the same analytical waveform model. The results are shown in Fig. III.8. We emphasize that in this study, we did not run a standard PE pipeline that stochastically explores a much greater parameter space. In particular, we do not consider varying the total mass or spin. Hence, our results are only a first indication of potential parameter ambiguities. Our results in Fig. III.8 show that the mismatch between the generated

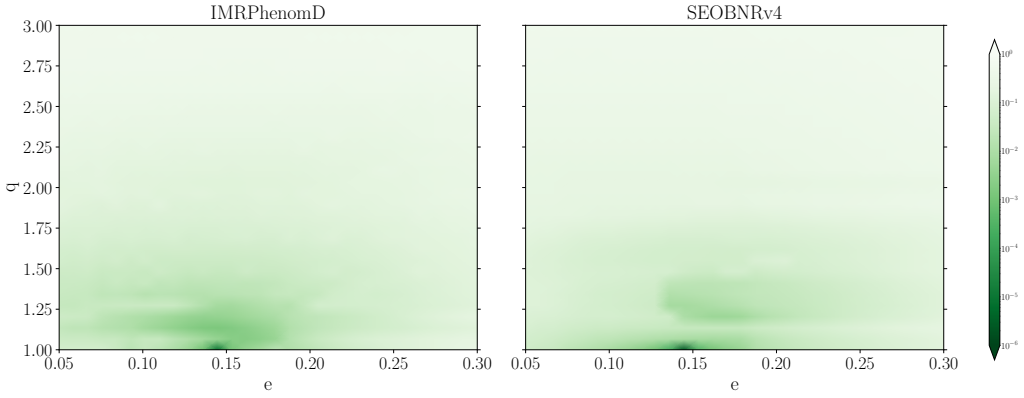

Figure III.8: Comparison with the highest eccentricity in the test dataset, $e = 0.144$, $q = 2$. We generate an eccentric waveform model derived from a nonspinning circular model, `IMRPhenomD` or `SEOBNRv4`, and compare the signal with models for different mass ratios and eccentricities. Waveforms with higher parameter distance have lower overlap. The color bar shows the $\log_{10}$ *mismatch.*

waveform and other waveforms having similar mass ratios but different eccentricities is relatively low, suggesting that an accurate measurement of the eccentricity is challenging for high-mass BBH systems where only the late inspiral and merger are accessible through the GW detection.

III.4 Conclusion and future perspectives

The detection of GWs from an eccentric BBH merger would be a crucial step towards understanding the physical evolution of compact binary coalescences and the nature of BBHs in globular clusters. Due to limitations in waveform modeling, the current search and parameter estimation pipelines in the LIGO/Virgo data analysis rely on analytical waveform models for circular binaries. One of the limitations to developing eccentric BBH models is the small number of eccentric NR simulations. NR simulations that are publicly available have low eccentricities ($e \leq 0.2$) at $M\omega^{2/3} = 0.075$. We use 20 NR simulations from the open SXS catalog and split them into 12 training datasets and 8 test datasets to develop our method.

We presented a novel method to convert any circular nonspinning waveform model into a low-eccentricity nonspinning waveform. To develop our method, we analyzed the residual modulations in the amplitude and frequency of eccentric waveforms compared to the circular signals with the same mass ratio in the 12 NR simulations of the training dataset. We modeled the decrease of eccentricity

over time, known as the eccentricity estimators, e_X, using a damped sinusoidal fit, where the fitting function is built upon four key parameters. We then performed a one-dimensional interpolation for each key parameter (A, B, and f) to build the eccentric waveform with the desired mass ratio and eccentricity. One of our model parameters, φ, shows no clear correlation with the physical parameters we explore. However, the small number of NR simulations used here did not allow us to model the effect of varying the mean anomaly in detail, and we expect φ to represent this degree of freedom. When quantifying the agreement between our model and the test data, we maximize over this nuisance parameter.

We then build a new model using the fitting values of e_X and the amplitude and frequency of the circular model which here we take from `IMRPhenomD` and `SEOBNRv4`. Our new model has an overlap $0.98 \lesssim O \lesssim 0.999$ over all NR simulations in our test dataset with the LIGO A+ design sensitivity curve. We hint that we need more training and test datasets for further development of this model beyond the current parameter boundaries. The computation of our method can be performed easily and quickly in the Python package `pyrex` [46].

Although we calibrate our model to a 50 $M_\odot$ BBH ($q \leq 3$, $e \leq 0.2$) starting at frequency $f_{\rm low} = 25$ Hz, we let the computation go slightly beyond the calibrated range. The calibrated time range of the waveform is from the late inspiral up to the near-merger phase, but we can extend the model through merger and ringdown by using the circular data. For the early inspiral, an analytical PN model could be used to complete the description of the entire coalescence. This way, our approach can be adapted to develop a complete IMR eccentric model. This would be especially important for future generations of GW interferometers as they have higher sensitivity especially in the low-frequency range. Careful studies of eccentric search and parameter estimation are needed to detect eccentric compact binary coalescences and their origin.

Acknowledgments

The authors would like to thank David Yeeles, Maria Haney, and Sebastian Khan for useful discussions, and the anonymous referee for insightful comments on the manuscript. Computations were carried out on the Holodeck cluster of the Max Planck Independent Research Group "Binary Merger Observations and Numerical Relativity" and the LIGO Laboratory computing cluster at California Institute of Technology. This work was supported by the Max Planck Society's Research Group Grant.

Bibliography

[1] Aasi J, et al. Characterization of the LIGO detectors during their sixth science run. Classical and Quantum Gravity. 2015 may;32(11):115012. Available from: https://doi.org/10.1088/0264-9381/32/11/115012.

[2] Acernese F, et al. Advanced Virgo: a second-generation interferometric gravitational wave detector. Classical and Quantum Gravity. 2015 December;32:024001. Available from: http://stacks.iop.org/0264-9381/32/i=2/a=024001.

[3] Akutsu T, Ando M, et al. KAGRA: 2.5 generation interferometric gravitational wave detector. Nat Astron. 2019 Jan;3:35–40. Available from: https://www.nature.com/articles/s41550-018-0658-y.

[4] Abbott BP, et al. GWTC-1: A Gravitational-Wave Transient Catalog of Compact Binary Mergers Observed by LIGO and Virgo during the First and Second Observing Runs. Phys Rev X. 2019 Sep;9:031040. Available from: https://link.aps.org/doi/10.1103/PhysRevX.9.031040.

[5] Abbott BP, et al. Search for Eccentric Binary Black Hole Mergers with Advanced LIGO and Advanced Virgo during Their First and Second Observing Runs. The Astrophysical Journal. 2019 sep;883(2):149. Available from: https://doi.org/10.3847/1538-4357/ab3c2d.

[6] Abbott BP, et al.. GWTC-2: Compact Binary Coalescences Observed by LIGO and Virgo During the First Half of the Third Observing Run; 2020. arXiv:2010.14527.

[7] Peters PC. Gravitational Radiation and the Motion of Two Point Masses. Phys Rev. 1964 Nov;136:B1224–B1232. Available from: https://link.aps.org/doi/10.1103/PhysRev.136.B1224.

[8] Samsing J, MacLeod M, Ramirez-Ruiz E. The formation of eccentric compact binary inspirals and the role of gravitational wave emission in binary-single stellar encounters. The Astrophysical Journal. 2014 mar;784(1):71. Available from: https://doi.org/10.1088%2F0004-637x%2F784%2F1%2F71.

[9] Lower ME, Thrane E, Lasky PD, Smith R. Measuring eccentricity in binary black hole inspirals with gravitational waves. Phys Rev D. 2018 Oct;98:083028. Available from: https://link.aps.org/doi/10.1103/PhysRevD.98.083028.

[10] Papaloizou, J C B , Nelson, R P , Masset, F . Orbital eccentricity growth through disc-companion tidal interaction. A&A. 2001;366(1):263–275. Available from: https://doi.org/10.1051/0004-6361:20000011.

[11] Kozai Y. Asteroids with large secular orbital variations. Icarus. 1980;41(1):89 – 95. Available from: http://www.sciencedirect.com/science/article/pii/001910358090161X.

[12] Lidov ML. The evolution of orbits of artificial satellites of planets under the action of gravitational perturbations of external bodies. Planetary and Space Science. 1962;9(10):719 – 759. Available from: http://www.sciencedirect.com/science/article/pii/0032063362901290.

[13] Gultekin K, Miller MC, Hamilton DP. Three-Body Dynamics with Gravitational Wave Emission. American Astronomical Society; 2006. Available from: https://doi.org/10.1086/499917.

[14] Rodriguez CL, Amaro-Seoane P, Chatterjee S, Kremer K, Rasio FA, Samsing J, et al. Post-Newtonian dynamics in dense star clusters: Formation, masses, and merger rates of highly-eccentric black hole binaries. Phys Rev D. 2018 Dec;98:123005. Available from: https://link.aps.org/doi/10.1103/PhysRevD.98.123005.

[15] Samsing J. Eccentric black hole mergers forming in globular clusters. Phys Rev D. 2018 May;97:103014. Available from: https://link.aps.org/doi/10.1103/PhysRevD.97.103014.

[16] Amaro-Seoane P, et al.. Laser Interferometer Space Antenna; 2017. arXiv:1702.00786.

[17] Ma S, Yunes N. Improved constraints on modified gravity with eccentric gravitational waves. Phys Rev D. 2019 Dec;100:124032. Available from: https://link.aps.org/doi/10.1103/PhysRevD.100.124032.

[18] Yunes N, Siemens X. Gravitational-Wave Tests of General Relativity with Ground-Based Detectors and Pulsar-Timing Arrays. Living Rev Relativ. 2013 Nov;16:9. Available from: https://link.springer.com/article/10.12942/lrr-2013-9.

[19] Huerta EA, Moore CJ, Kumar P, George D, Chua AJK, Haas R, et al. Eccentric, nonspinning, inspiral, Gaussian-process merger approximant for the detection and characterization of eccentric binary black hole mergers. Phys Rev D. 2018 Jan;97:024031. Available from: https://link.aps.org/doi/10.1103/PhysRevD.97.024031.

[20] Cao Z, Han WB. Waveform model for an eccentric binary black hole based on the effective-one-body-numerical-relativity formalism. Phys Rev D. 2017 Aug;96:044028. Available from: https://link.aps.org/doi/10.1103/PhysRevD.96.044028.

[21] Hinder I, Kidder LE, Pfeiffer HP. Eccentric binary black hole inspiral-merger-ringdown gravitational waveform model from numerical relativity and post-Newtonian theory. Phys Rev D. 2018 Aug;98:044015. Available from: https://link.aps.org/doi/10.1103/PhysRevD.98.044015.

[22] Chiaramello D, Nagar A. Faithful analytical effective-one-body waveform model for spin-aligned, moderately eccentric, coalescing black hole binaries. Phys Rev D. 2020 May;101:101501. Available from: https://link.aps.org/doi/10.1103/PhysRevD.101.101501.

[23] Nagar A, Bonino A, Rettegno P. All in one: effective one body multipolar waveform model for spin-aligned, quasi-circular, eccentric, hyperbolic black hole binaries; 2021. https://arxiv.org/abs/2101.08624.

[24] Hinder I. "EccentricIMR"; 2018. https://github.com/ianhinder/EccentricIMR. Available from: https://github.com/ianhinder/EccentricIMR.

[25] Islam T, Varma V, Lodman J, Field SE, Khanna G, Scheel MA, et al. Eccentric binary black hole surrogate models for the gravitational waveform and remnant properties: Comparable mass, nonspinning case. Phys Rev D. 2021 Mar;103:064022. Available from: https://link.aps.org/doi/10.1103/PhysRevD.103.064022.

[26] Tanay S, Haney M, Gopakumar A. Frequency and time-domain inspiral templates for comparable mass compact binaries in eccentric orbits. Phys Rev D. 2016 Mar;93:064031. Available from: https://link.aps.org/doi/10.1103/PhysRevD.93.064031.

[27] Huerta EA, Kumar P, McWilliams ST, O'Shaughnessy R, Yunes N. Accurate and efficient waveforms for compact binaries on eccentric orbits. Phys Rev D. 2014 Oct;90:084016. Available from: https://link.aps.org/doi/10.1103/PhysRevD.90.084016.

[28] Moore B, Favata M, Arun KG, Mishra CK. Gravitational-wave phasing for low-eccentricity inspiralling compact binaries to 3PN order. Phys Rev D. 2016 Jun;93:124061. Available from: https://link.aps.org/doi/10.1103/PhysRevD.93.124061.

[29] Romero-Shaw IM, Lasky PD, Thrane E. Searching for eccentricity: signatures of dynamical formation in the first gravitational-wave transient catalogue of LIGO and Virgo. Monthly Notices of the Royal Astronomical Society. 2019 10;490(4):5210–5216. Available from: https://doi.org/10.1093/mnras/stz2996.

[30] Romero-Shaw IM, Farrow N, Stevenson S, Thrane E, Zhu XJ. On the origin of GW190425. Monthly Notices of the Royal Astronomical Society: Letters. 2020 05;496(1):L64–L69. Available from: https://doi.org/10.1093/mnrasl/slaa084.

[31] Romero-Shaw I, Lasky PD, Thrane E, Bustillo JC. GW190521: Orbital Eccentricity and Signatures of Dynamical Formation in a Binary Black Hole Merger Signal. The Astrophysical Journal. 2020 oct;903(1):L5. Available from: https://doi.org/10.3847/2041-8213/abbe26.

[32] Gayathri V, Healy J, Lange J, O'Brien B, Szczepanczyk M, Bartos I, et al.. GW190521 as a Highly Eccentric Black Hole Merger; 2020. arXiv:2009.05461.

[33] Abbott R, et al. GW190521: A Binary Black Hole Merger with a Total Mass of 150 $M_{\odot}$. Phys Rev Lett. 2020 Sep;125:101102. Available from: https://link.aps.org/doi/10.1103/PhysRevLett.125.101102.

[34] "SXS catalog"; 2020. http://www.black-holes.org/waveforms. Available from: http://www.black-holes.org/waveforms.

[35] Khan S, Husa S, Hannam M, Ohme F, Pürrer M, Forteza XJ, et al. Frequency-domain gravitational waves from nonprecessing black-hole binaries. II. A phenomenological model for the advanced detector era. Phys Rev D. 2016 Feb;93:044007. Available from: https://link.aps.org/doi/10.1103/PhysRevD.93.044007.

[36] Hannam M, Schmidt P, Bohé A, Haegel L, Husa S, Ohme F, et al. Simple Model of Complete Precessing Black-Hole-Binary Gravitational Waveforms. Phys Rev Lett. 2014;113(15):151101.

[37] Santamaría L, Ohme F, Ajith P, Brügmann B, Dorband N, Hannam M, et al. Matching post-Newtonian and numerical relativity waveforms: Systematic errors and a new phenomenological model for nonprecessing black hole binaries. Phys Rev D. 2010 Sep;82:064016. Available from: https://link.aps.org/doi/10.1103/PhysRevD.82.064016.

[38] Buonanno A, Damour T. Effective one-body approach to general relativistic two-body dynamics. Phys Rev D. 1999 Mar;59:084006. Available from: https://link.aps.org/doi/10.1103/PhysRevD.59.084006.

[39] Pan Y, Buonanno A, Buchman LT, Chu T, Kidder LE, Pfeiffer HP, et al. Effective-one-body waveforms calibrated to numerical relativity simulations: Coalescence of nonprecessing, spinning, equal-mass black holes. Phys Rev D. 2010 Apr;81:084041. Available from: https://link.aps.org/doi/10.1103/PhysRevD.81.084041.

[40] Khan S, Ohme F, Chatziioannou K, Hannam M. Including higher order multipoles in gravitational-wave models for precessing binary black holes. Phys Rev D. 2020 Jan;101(2):024056.

[41] Khan S, Chatziioannou K, Hannam M, Ohme F. Phenomenological model for the gravitational-wave signal from precessing binary black holes with two-spin effects. Phys Rev D. 2019;100(2):024059.

[42] Pratten G, García-Quirós C, Colleoni M, Ramos-Buades A, Estellés H, Mateu-Lucena M, et al. Computationally efficient models for the dominant and subdominant harmonic modes of precessing binary black holes. Phys Rev D. 2021 May;103:104056. Available from: https://link.aps.org/doi/10.1103/PhysRevD.103.104056.

[43] Estellés H, Ramos-Buades A, Husa S, García-Quirós C, Colleoni M, Haegel L, et al.. IMRPhenomTP: A phenomenological time domain model for dominant quadrupole gravitational wave signal of coalescing binary black holes; 2020. arXiv:2004.08302.

[44] Setyawati Y, Ohme F, Khan S. Enhancing gravitational waveform models through dynamic calibration. Phys Rev D. 2019 Jan;99:024010. Available from: https://link.aps.org/doi/10.1103/PhysRevD.99.024010.

[45] Setyawati Y, Pürrer M, Ohme F. Regression methods in waveform modeling: a comparative study. Classical and Quantum Gravity. 2020 mar;37(7):075012. Available from: https://doi.org/10.1088%2F1361-6382%2Fab693b.

[46] Setyawati Y, Ohme F. Yoshinta/pyrex: public release of pyrex. Zenodo; 2021. Available from: https://doi.org/10.5281/zenodo.4818195.

[47] Pfeiffer HP, Brown DA, Kidder LE, Lindblom L, Lovelace G, Scheel MA. Reducing orbital eccentricity in binary black hole simulations. Classical

and Quantum Gravity. 2007 may;24(12):S59–S81. Available from: https://doi.org/10.1088%2F0264-9381%2F24%2F12%2Fs06.

[48] Ajith P, et al.. Data formats for numerical relativity waves; 2011. arXiv:0709.0093.

[49] Ramos-Buades A, Husa S, Pratten G. Simple procedures to reduce eccentricity of binary black hole simulations. Phys Rev D. 2019;99(2):023003.

[50] Mroué AH, Pfeiffer HP, Kidder LE, Teukolsky SA. Measuring orbital eccentricity and periastron advance in quasicircular black hole simulations. Phys Rev D. 2010 Dec;82:124016. Available from: https://link.aps.org/doi/10.1103/PhysRevD.82.124016.

[51] Savitzky A, Golay MJE. Smoothing and Differentiation of Data by Simplified Least Squares Procedures. Analytical Chemistry. 1964 July;36:8. Available from: https://doi.org/10.1021/ac60214a047.

[52] Bohé A, Shao L, Taracchini A, Buonanno A, Babak S, Harry IW, et al. Improved effective-one-body model of spinning, nonprecessing binary black holes for the era of gravitational-wave astrophysics with advanced detectors. Phys Rev D. 2017 Feb;95:044028. Available from: https://link.aps.org/doi/10.1103/PhysRevD.95.044028.

[53] Taracchini A, Buonanno A, Pan Y, Hinderer T, Boyle M, Hemberger DA, et al. Effective-one-body model for black-hole binaries with generic mass ratios and spins. Phys Rev D. 2014 Mar;89:061502. Available from: https://link.aps.org/doi/10.1103/PhysRevD.89.061502.

[54] Upgraded LIGO to search for universe's most extreme events; 2019. [Online; accessed 20-Jan-2021]. https://www.nsf.gov/news/news_summ.jsp?cntn_id=297414.

[55] Maggiore M, et al. Science case for the Einstein telescope. Journal of Cosmology and Astroparticle Physics. 2020 mar;2020(03):050–050. Available from: https://doi.org/10.1088/1475-7516/2020/03/050.

[56] Reitze D, et al. Cosmic Explorer: The U.S. Contribution to Gravitational-Wave Astronomy beyond LIGO. Bulletin of the AAS. 2019 9;51(7). Https://baas.aas.org/pub/2020n7i035. Available from: https://baas.aas.org/pub/2020n7i035.

[57] "Exploring the Sensitivity of Next Generation Gravitational Wave Detectors"; 2016. https://dcc.ligo.org/LIGO-P1600143/public. Available from: https://dcc.ligo.org/LIGO-P1600143/public.

4
Conclusions and future prospects

"A new scientific truth does not triumph by convincing its opponents and making them see the light, but rather because its opponents eventually die, and a new generation grows up that is familiar with it."

Max Planck

4.1 Summary and discussion

Signal analysis of GW data observed by LIGO and Virgo is carried out by computing the likelihood between the output data and the template model. These templates are derived from solving the vacuum Einstein's field equations with two main approaches, analytical and numerical relativity. Analytically, one expands the v/c terms of flux and energy known as PN approximation. Although PN is computationally quick, this approximation becomes unfaithful when the binary moves faster towards merger (fast-less accurate). Another approach is to solve Einstein's field equations numerically. NR provides better accuracy, especially in the regime where PN breaks down, despite the higher computational cost (slow-more accurate). Hence, only relatively a few numbers of NR simulations are available. Bridging these two methods has been the focus of many studies developed in the community. We highlight two semi-analytical approaches that provide fast-more accurate waveforms are known as EOB and the *Phenomenological* models.

The goal of these studies is to build a model that has high accuracy towards NR, spans wide parameter ranges and is computationally cheap.

To some extent, these semi-analytical models have been calibrated to NR. However, when new NR simulations become available, one needs to recompute the fitting algorithm or recalibrate the current model with the new numerical simulations in the parameter of interest. This work demands human resources and is time-consuming. We highlight this issue and investigate strategies to automatically calibrate any waveform models without requiring extensive human dependency.

We began with developing a method that projects sparse-more accurate waveforms onto a set of dense-less accurate ones. This method deals with dimensionality reduction and interpolation, which becomes crucial when more source parameters are included in the model. The results are a set of waveforms with accuracy that lies between the two models and can be generated swiftly. Here we guarantee that our new waveforms always have higher accuracy towards the sparse model compared to the agreement between the two initial ones. This study is important for the source modeling, especially to ensure that the transition between the new model to the existing one is smooth. More importantly, we can apply our proof of concept studies further to various models with different parameters.

Our new set of waveforms have reasonable accuracy across the parameter space. However, we face challenges as we expand to higher dimensional parameters due to poorer accuracy and higher computational cost of interpolation. We should emphasize that this problem also occurs in various models as interpolation is the cornerstone in developing a gravitational waveform model. We follow up this issue by directly comparing the accuracy and computational complexity of various interpolation, regression, and fitting techniques. This comparison is important to develop strategies with more dimensional parameters and tackle more datasets. Moreover, we find that complex interpolation techniques do not always yield the most accurate and fastest results. By direct comparison, the outcome of this study favors polynomial interpolation as a prospectus interpolation technique, especially with higher dimensional parameters that include precessing system (seven parameters). Of course, one may exchange computational complexity and accuracy depending on the study goal.

Initially, we expected to expand our studies beyond seven dimensions (precessing - eccentric). However, eccentric waveform models are poorly developed at the time of our studies as there are only a few NR data publicly available. We note that the development of an eccentric model is demanding, especially after the detection of GW190521, an event that may be highly eccentric or highly precessing BBH. Signal analysis of such events can be improved with a better eccentric model applicable in the template. Besides, the discovery of an eccentric BBH would help us understand the origin of BBH that is crucial in astronomy.

Thus, we developed an algorithm to turn any quasicircular waveform model into eccentric ones. In this study, we employ publicly available nonspinning NR simulations focusing on the late inspiral regime. We investigated the residual oscillations of eccentric NR from its quasicircular counterpart with the same mass component. This way, we interpolate quantities that depend on mass ratio and eccentricity to produce a new set of waveforms. Learning from NR behavior, we apply a similar method to any semi-analytical waveform model. Thus, we perform a 'twist' to any nonspinning quasicircular semi-analytical model to produce its eccentric counterpart. We should emphasize that we do not create a new eccentric model, but provide a ready-to-use algorithm to add eccentricity to any nonspinning quasicircular models.

In summary, the key contribution of our studies lies in the general methods that can be applied to improve any existing models and can be adopted in any waveform family. Through publications I, II, and III, we summarize our findings as follows

1. The enriched basis method (see publication I) is reliable in developing a rapid and accurate model. This method guarantees that the new model has at least the same accuracy as the basis. The faithfulness is increased with more iterations.

2. The enriched basis method from the projection of one model to another would produce less smooth waveforms than the data reduction originated from the same model. Studies in the data placing and regression lead to further improvements.

3. The traditional regression methods in publication II may provide a comparable accuracy or speed against ML methods, at least up to seven-dimensional parameter spaces. According to our analysis, advanced computational complexity may not be necessary. However, ML may speed up the process for parameter spaces with more dimensions.

4. We show that we can convert circular waveform models into eccentric ones in publication III. For the nonspinning model, the fitting function depends strongly on mass ratio and eccentricity. The residual amplitude oscillation depends on the eccentricity, and the frequency depends on the mass ratio.

Furthermore, we obtained the following results:

(i) A proof of concept to dynamically calibrate any waveform model using an iterative SVD. We investigate a method to update waveforms with lower dimensionality using another model with more dimensions.

(ii) A Python package that automatically categorizes training and test data from the dataset. This package is called `pycachu`, where the computation of iterative SVD is carried over.

(iii) Analysis of various regression methods that include accuracy, speed, and computational complexity.

(iv) A publicly available Python package, `pyrex` adds eccentricity to any circular nonspinning analytical waveforms.

4.2 Future prospects

We highlight possible extension of our studies as follows:

A **Reduced order quadrature (ROQ).** Future GW interferometers are expected to be more sensitive. Hence, we would observe more distant compact binary coalescences and higher SNR for closer binaries. The detection rates increase with the improved sensitivity. This improvement comes with a demand for faster parameter estimation. We can expand the enriched basis method further with the detector output data s to speed up the analysis. We start with the reduced basis from a set of orthogonal basis waveforms varying in parameters, B. Subsequently, we project a full GW signal onto these data and interpolate the results. We then iterate the procedure with some validation points until the overlap results are below some threshold.

Let us start with the waveform generation by projecting the enriched basis waveforms (Eq. (I.16) in publication II), which reads

$$P_j^{EB}(f;\vec{\lambda}) = \Sigma_{k=1}^{K} c_k'(\vec{\lambda}) v_{kj}^T. \tag{4.1}$$

We can remove index j and rename the notation of the reduced bases by

$$h = \Sigma_{k=1}^{K} c_k'(\vec{\lambda}) v_k^T. \tag{4.2}$$

Revisiting Eq. (2.47), the log-likelihood ratio satisfies

$$\ln \Lambda = (s|h) - \frac{1}{2}(h|h), \tag{4.3}$$

with the *inner product* defined as

$$(s|h) = 4\mathcal{R} \int_0^\infty \frac{h(f)s^*(f)}{S_n(f)}. \tag{4.4}$$

We can substitute Eq. (4.2) to (2.47) and modify $(s|h)$ such that

$$(s|h)_{ROQ} = \mathcal{R}\Sigma_{k=1}^{K} h(\vec{\lambda})\omega_k, \tag{4.5}$$

with

$$\omega_k = 4\Delta f \Sigma_{j=1}^{M} \frac{s^*(f_j)v_k^T(f_j)}{S_n(f_j)}. \tag{4.6}$$

Similarly,

$$(h|h)_{ROQ} = \Sigma_k h^*(\vec{\lambda})h(\vec{\lambda})\Psi_k, \tag{4.7}$$

with the weights Ψ_k

$$\Psi_k = 4\Delta f \Sigma_{j=1}^{M} \frac{C_k(f_j)}{S_n(f_j)}, C_k = v_k^T(f_j)(v_k^T(f_j))^* \tag{4.8}$$

where Δf is the delta frequency, and f_j is the j^{th} sample frequency.

The ROQ method [48] has been applied to speed up the analysis of GW data. Further improvements may include precessing systems and parameter spaces with higher dimensionality.

B **Prospect of developing waveforms with ML**. We described various regression techniques to speed up the waveform generations in Publication II. Although ML is a promising technique, it might be redundant for parameter spaces with less than seven dimensions. We argue that other traditional methods can provide comparable accuracy and speed. However, ML may speed up the process when including more than seven-dimensional parameter spaces such as precessing eccentric model. Studies on ML in waveform generation are currently underway [106, 107, 108, 109].

C **Modeling eccentric BBH for the 3G era.** The first detection of an eccentric BBH would help us to learn more about binary evolution. However, only a few numbers of eccentric models are available and are relatively difficult to compute. We proposed a simple method to convert any circular waveform model into an eccentric model without losing much accuracy. The algorithm can be applied further to create an IMR model by hybridizing with the inspiral from PN approximation, higher eccentricity from NR simulations, and the inclusion of the spin parameters.

Acknowledgements

First and foremost, I would like to thank God for His blessing along the path of my scientific studies. The works presented here are the results of numerous discussions, advice, and support from many people. I would like to express my sincere thanks to all of them.

I am very grateful to my supervisor, Frank Ohme, for giving me an opportunity to conduct research and support me with countless guidance and training during my studies. I am pleased to be part of his group funded by the Max Planck Independent Research Group grant at the Albert Einstein Institute, Hannover.

During my PhD, I received supportive advice from the thesis advisory committee, Prof. Michèle Heurs, and Prof. Bruce Allen. Our discussion shaped my studies. I would also like to thank Prof. Badri Krishnan, Prof. Domenico Giulini, Prof. Harald Pfeiffer, and Prof. Benno Willke in my thesis defense committee for carefully evaluate my dissertation.

I thank my colleagues, Wolfgang Kastaun, Benjamin Knispel, Collin Capano, and my housemate, Natassa Rustandi, for the thorough comments on my dissertation. The published articles presented here are the results of numerous back-and-forth discussions between my co-authors and me, as well as the referees. Thanks to Sebastian Khan, Michael Pürrer, and the anonymous referees for the critical review of my papers.

I would like to thank Prof. Chris van den Broeck of Utrecht University for offering me an opportunity to expand my knowledge and skills. Through exciting projects and meetings in the group, I learn about the big picture of my research.

I appreciate any non-scientific supports during my studies. Thanks to the secretaries Gabriela Richardson, Oksana Khiari, Birgit Ohlendorf, and Luisa Gärner for helping me with administrative issues. I am also grateful to the AEI cluster team, Carsten Aulbert, Henning Fehrmann, and Alexander Post for their numerous help and swift responses on the computational cluster problems.

Thanks to my former supervisor and lectures at Unpar Bandung, Paulus Tjiang, Philips Gunawidjaja, Aloysius Rusli, and Reinard Primulando for giving me an opportunity to present my work and my thoughts on many occasions. I enjoyed my time giving webinars and motivating young physics students in Indonesia.

Furthermore, I am grateful that I receive support from my friends Nunik Rukmini and Jane Arifin. A special thanks to my mentor, Dr. Roger Cutler, who advise and strengthen me during my PhD. It is a wonderful experience to be his mentee.

Further, I would like to thank my colleagues and friends at the AEI, Krishnendu, Marlin Schäfer, Lars Nieder, Banafsheh Beheshtipour, Xisco Jimenez Forteza, Sumit Kumar, Alexander Nitz, Julian Westerweck, Anjana Ashok, Rahul Dhurkunde, Christoph Dreissigacker, Reinhard Prix, Kate Vanderpool, and Doris Stubenrauch for amazing discussions and creating a friendly environment on different occasions. I enjoyed my time in Hannover, learning German culture while still engaging in an international community.

These acknowledgements would not be complete without mentioning supports from my family. I would like to thank my parents, sister, and uncle for their faith in me and support me throughout the years. Last but not least, I would like to thank Benjamin Wied for his patience and for helping me with the German translation.

Bibliography

[1] Einstein, A . Approximate integration of the field equations of gravitations. Sitzungsber Preuss Akad Wiss Berlin (Math Phys). 1916;p. 688–696.

[2] Wheeler JA. A journey into gravity and spacetime. Scientific American Library; 1990.

[3] Cervantes-Cota JL, Galindo-Uribarri S, Smoot GF. A Brief History of Gravitational Waves. Universe. 2016;2(3). Available from: https://www.mdpi.com/2218-1997/2/3/22.

[4] Bailes M, et al. Gravitational-wave physics and astronomy in the 2020s and 2030s. Nature Reviews Physics. 2021 Jun;3(5):344–366.

[5] Abbott, B P and others. Properties of the Binary Neutron Star Merger GW170817. Phys Rev X. 2019 Jan;9:011001. Available from: https://link.aps.org/doi/10.1103/PhysRevX.9.011001.

[6] Hughes S. Trust but verify: The case for astrophysical black holes; 2005.

[7] Hulse RA, Taylor JH. Discovery of a pulsar in a binary system. ApJ. 1975 Jan;195:L51–L53.

[8] Abbott, B P and others. Observation of Gravitational Waves from a Binary Black Hole Merger. Phys Rev Lett. 2016;116(6):061102.

[9] Michelson AA, Morley EW. On the Relative Motion of the Earth and the Luminiferous Ether. American Journal of Science. 1887;34(203):333–345.

[10] Abbott R, et al. Observation of Gravitational Waves from Two Neutron Star–Black Hole Coalescences. The Astrophysical Journal Letters. 2021 jun;915(1):L5. Available from: https://doi.org/10.3847/2041-8213/ac082e.

[11] GWaviz; 2021. https://github.com/Yoshinta/GWaviz.

[12] Hartle JB. Gravity: An Introduction to Einstein's General Relativity. vol. 1. Addison-Wesley; 2003.

[13] Maggiore M. Gravitational waves : Volume 1, Theory and experiments. vol. 1. Great Clarendon Street, Oxford OX2 6DP, UK: Oxford University Press; 2008.

[14] Ohme F. Bridging the Gap between Post-Newtonian Theory and Numerical Relativity in Gravitational-Wave Data Analysis. Potsdam U.; 2012.

[15] Schutz B. A First Course in General Relativity. 2nd ed. Cambridge University Press; 2009.

[16] Maggiore M, et al. Science case for the Einstein telescope. Journal of Cosmology and Astroparticle Physics. 2020 mar;2020(03):050–050. Available from: https://doi.org/10.1088/1475-7516/2020/03/050.

[17] Hough J, Rowan S, Sathyaprakash BS. The search for gravitational waves. Journal of Physics B: Atomic, Molecular and Optical Physics. 2005 apr;38(9):S497–S519. Available from: https://doi.org/10.1088/0953-4075/38/9/004.

[18] Flanagan ÉÉ, Hughes SA. The basics of gravitational wave theory. 2005 sep;7:204–204. Available from: https://doi.org/10.1088/1367-2630/7/1/204.

[19] Weber J. Detection and Generation of Gravitational Waves. Phys Rev. 1960 Jan;117:306–313. Available from: https://link.aps.org/doi/10.1103/PhysRev.117.306.

[20] Weber J. General Relativity and Gravitational Waves. New York: Interscience Publishers; 1961.

[21] Aasi J, et al. Advanced LIGO. Classical and Quantum Gravity. 2015 March;32:074001. Available from: http://stacks.iop.org/0264-9381/32/i=7/a=074001.

[22] Rakhmanov, M and Klimenko, S . Angular Correlation of LIGO Hanford and Livingston Interferometers;.

[23] Reitze D, et al.. Cosmic Explorer: The U.S. Contribution to Gravitational-Wave Astronomy beyond LIGO; 2019. arXiv:1907.04833.

[24] Ackley K, et al. Neutron Star Extreme Matter Observatory: A kilohertz-band gravitational-wave detector in the global network. Astronomical Society of Australia. 2020 Nov;37(E047).

[25] Wang B, Zhu Z, Li A, Zhao W. Comprehensive Analysis of the Tidal Effect in Gravitational Waves and Implication for Cosmology. The Astrophysical Journal Supplement Series. 2020 aug;250(1):6. Available from: https://doi.org/10.3847/1538-4365/aba2f3.

[26] Brown DA. Searching for Gravitational Radiation from Binary Black Hole MACHOs in the Galactic Halo. University of Wisconsin-Milwaukee; 2004.

[27] Abbott, B P and others. GWTC-1: A Gravitational-Wave Transient Catalog of Compact Binary Mergers Observed by LIGO and Virgo during the First and Second Observing Runs. Phys Rev X. 2019 Sep;9:031040. Available from: https://link.aps.org/doi/10.1103/PhysRevX.9.031040.

[28] Abbott R, et al. GWTC-2: Compact Binary Coalescences Observed by LIGO and Virgo during the First Half of the Third Observing Run. Phys Rev X. 2021 Jun;11:021053. Available from: https://link.aps.org/doi/10.1103/PhysRevX.11.021053.

[29] Finn LS, Chernoff DF. Observing binary inspiral in gravitational radiation: One interferometer. Phys Rev D. 1993 Mar;47:2198–2219. Available from: https://link.aps.org/doi/10.1103/PhysRevD.47.2198.

[30] Blanchet L. Gravitational Radiation from Post-Newtonian Sources and Inspiralling Compact Binaries. Living Rev Relativ. 2014 Dec;17. Available from: https://link.springer.com/content/pdf/10.12942/lrr-2014-2.pdf.

[31] Blanchet L, Damour T, Esposito-Farèse G, Iyer BR. Gravitational Radiation from Inspiralling Compact Binaries Completed at the Third Post-Newtonian Order. Phys Rev Lett. 2004 Aug;93:091101. Available from: https://link.aps.org/doi/10.1103/PhysRevLett.93.091101.

[32] Blanchet L, Faye G, Iyer BR, Sinha S. The third post-Newtonian gravitational wave polarizations and associated spherical harmonic modes for inspiralling compact binaries in quasi-circular orbits. Classical and Quantum Gravity. 2008 jul;25(16):165003. Available from: https://doi.org/10.1088/0264-9381/25/16/165003.

[33] Arun KG, Buonanno A, Faye G, Ochsner E. Higher-order spin effects in the amplitude and phase of gravitational waveforms emitted by inspiraling compact binaries: Ready-to-use gravitational waveforms. Phys Rev D. 2009 May;79:104023. Available from: https://link.aps.org/doi/10.1103/PhysRevD.79.104023.

[34] Schmidt P, Hannam M, Husa S. Towards models of gravitational waveforms from generic binaries: A simple approximate mapping between precessing and nonprecessing inspiral signals. Phys Rev D. 2012 Nov;86:104063. Available from: https://link.aps.org/doi/10.1103/PhysRevD.86.104063.

[35] Hannam M, Schmidt P, Bohé A, Haegel L, Husa S, Ohme F, et al. Simple Model of Complete Precessing Black-Hole-Binary Gravitational Waveforms. Phys Rev Lett. 2014 Oct;113:151101. Available from: https://link.aps.org/doi/10.1103/PhysRevLett.113.151101.

[36] Pratten G, et al.. Let's twist again: computationally efficient models for the dominant and sub-dominant harmonic modes of precessing binary black holes; 2020. arXiv:2004.06503.

[37] Tanay S, Haney M, Gopakumar A. Frequency and time-domain inspiral templates for comparable mass compact binaries in eccentric orbits. Phys Rev D. 2016 Mar;93:064031. Available from: https://link.aps.org/doi/10.1103/PhysRevD.93.064031.

[38] Cho G, Tanay S, Gopakumar A, Lee S. Generalized quasi-Keplerian parametric solution at the fourth PN order and its eccentric inspiral-merger-ringdown waveform; in preparation.

[39] Schnittman JD. Spin-orbit resonance and the evolution of compact binary systems. Phys Rev D. 2004 Dec;70:124020. Available from: https://link.aps.org/doi/10.1103/PhysRevD.70.124020.

[40] Buonanno B, Sathyaprakash BS. Sources of Gravitational Waves: Theory and Observations; 2014. arXiv:1410.7832.

[41] Baumgarte T, Shapiro S. Numerical Relativity: Solving Einstein's Equations on the Computer. vol. 1. The Edinburgh Building, Cambridge, CB2 8RU, UK: Cambridge University Press; 2010.

[42] Centrella, Joan and Baker, John G and Kelly, Bernard J and van Meter, James R . Black-hole binaries, gravitational waves, and numerical

relativity. Rev Mod Phys. 2010 Nov;82:3069–3119. Available from: https://link.aps.org/doi/10.1103/RevModPhys.82.3069.

[43] Cook, G B . Initial Data for Numerical Relativity. Living Rev Relativ. 2000 Nov;3:5. Available from: https://link.springer.com/article/10.12942/lrr-2000-5.

[44] Cardoso, V and Gualtieri, L and Herdeiro, C and others. Exploring New Physics Frontiers Through Numerical Relativity. Living Rev Relativ. 2015 Sep;18:1. Available from: https://link.springer.com/article/10.1007%2Flrr-2015-1.

[45] Palenzuela C. Introduction to Numerical Relativity. Frontiers in Astronomy and Space Sciences. 2020;7:58. Available from: https://www.frontiersin.org/article/10.3389/fspas.2020.00058.

[46] Arnowitt R, Deser S, Misner CW. Republication of: The dynamics of general relativity. Gen Relativ Gravit. 2008;40.

[47] Kidder LE, Scheel MA, Teukolsky SA. Extending the lifetime of 3D black hole computations with a new hyperbolic system of evolution equations. Phys Rev D. 2001 Aug;64:064017. Available from: https://link.aps.org/doi/10.1103/PhysRevD.64.064017.

[48] Shibata M, Nakamura T. Evolution of three-dimensional gravitational waves: Harmonic slicing case. Phys Rev D. 1995 Nov;52:5428–5444. Available from: https://link.aps.org/doi/10.1103/PhysRevD.52.5428.

[49] Baumgarte TW, Shapiro SL. Numerical integration of Einstein's field equations. Phys Rev D. 1998 Dec;59:024007. Available from: https://link.aps.org/doi/10.1103/PhysRevD.59.024007.

[50] Brandt S, Brügmann B. A Simple Construction of Initial Data for Multiple Black Holes. Phys Rev Lett. 1997 May;78:3606–3609. Available from: https://link.aps.org/doi/10.1103/PhysRevLett.78.3606.

[51] Brill DR, Lindquist RW. Interaction Energy in Geometrostatics. Phys Rev. 1963 Jul;131:471–476. Available from: https://link.aps.org/doi/10.1103/PhysRev.131.471.

[52] Hannam M, Husa S, Ohme F, Brügmann B, Ó Murchadha N. Wormholes and trumpets: Schwarzschild spacetime for the moving-puncture generation. Phys Rev D. 2008 Sep;78:064020. Available from: https://link.aps.org/doi/10.1103/PhysRevD.78.064020.

[53] Pretorius F. Numerical relativity using a generalized harmonic decomposition. Classical and Quantum Gravity. 2005 jan;22(2):425–451. Available from: https://doi.org/10.1088/0264-9381/22/2/014.

[54] Newman E. An Approach to Gravitational Radiation by a Method of Spin Coefficients. Journal of Mathematical Physics. 1962;3:566. Available from: https://aip.scitation.org/doi/abs/10.1063/1.1724257.

[55] Bishop NT, Rezzolla L. Extraction of gravitational waves in numerical relativity. Living Reviews in Relativity. 2016 Oct;19(1). Available from: http://dx.doi.org/10.1007/s41114-016-0001-9.

[56] Ajith P , Boyle M , Brown D , Fairhurst S , Hannam M , Hinder I , Husa S , Krishnan B , Mercer R , Ohme F , Ott C Read J , Santamaría L , Whelan J . Data formats for numerical relativity waves; 2011. arXiv:0709.0093.

[57] "SXS Gravitational Waveform Database"; 2021. http://www.black-holes.org/waveforms. Available from: http://www.black-holes.org/waveforms.

[58] "Georgia catalog"; 2021. https://github.com/cevans216/gt-waveform-catalog. Available from: https://github.com/cevans216/gt-waveform-catalog.

[59] "RIT catalog of numerical simulations"; 2021. https://ccrgpages.rit.edu/~RITCatalog/. Available from: https://ccrgpages.rit.edu/~RITCatalog/.

[60] Setyawati Y, Ohme F. Adding eccentricity to quasicircular binary-black-hole waveform models. Phys Rev D. 2021 Jun;103:124011. Available from: https://link.aps.org/doi/10.1103/PhysRevD.103.124011.

[61] Buonanno A, Damour T. Effective one-body approach to general relativistic two-body dynamics. Phys Rev D. 1999 Mar;59:084006. Available from: https://link.aps.org/doi/10.1103/PhysRevD.59.084006.

[62] Buonanno A, Damour T. Transition from inspiral to plunge in binary black hole coalescences. Phys Rev D. 2000 Aug;62:064015. Available from: https://link.aps.org/doi/10.1103/PhysRevD.62.064015.

[63] Ajith P, Babak S, Chen Y, Hewitson M, Krishnan B, Whelan JT, et al. A phenomenological template family for black-hole coalescence waveforms. Classical and Quantum Gravity. 2007 sep;24(19):S689–S699. Available from: https://doi.org/10.1088/0264-9381/24/19/s31.

[64] Damour T. Coalescence of two spinning black holes: An effective one-body approach. Phys Rev D. 2001 Nov;64:124013. Available from: https://link.aps.org/doi/10.1103/PhysRevD.64.124013.

[65] Damour T, Jaranowski P, Schäfer G. Determination of the last stable orbit for circular general relativistic binaries at the third post-Newtonian approximation. Phys Rev D. 2000 Sep;62:084011. Available from: https://link.aps.org/doi/10.1103/PhysRevD.62.084011.

[66] Cotesta R, Marsat S, Pürrer M. Frequency-domain reduced-order model of aligned-spin effective-one-body waveforms with higher-order modes. Phys Rev D. 2020 Jun;101:124040. Available from: https://link.aps.org/doi/10.1103/PhysRevD.101.124040.

[67] Nagar A, Rettegno P. Efficient effective one body time-domain gravitational waveforms. Phys Rev D. 2019 Jan;99:021501. Available from: https://link.aps.org/doi/10.1103/PhysRevD.99.021501.

[68] Nagar A, et al. Time-domain effective-one-body gravitational waveforms for coalescing compact binaries with nonprecessing spins, tides, and self-spin effects. Phys Rev D. 2018 Nov;98:104052. Available from: https://link.aps.org/doi/10.1103/PhysRevD.98.104052.

[69] Cotesta R, Buonanno A, Bohé A, Taracchini A, Hinder I, Ossokine S. Enriching the symphony of gravitational waves from binary black holes by tuning higher harmonics. Phys Rev D. 2018 Oct;98:084028. Available from: https://link.aps.org/doi/10.1103/PhysRevD.98.084028.

[70] Ajith P, Babak S, Chen Y, Hewitson M, Krishnan B, Sintes AM, et al. Template bank for gravitational waveforms from coalescing binary black holes: Nonspinning binaries. Phys Rev D. 2008 May;77:104017. Available from: https://link.aps.org/doi/10.1103/PhysRevD.77.104017.

[71] Ajith P, Hannam M, Husa S, Chen Y, Brügmann B, Dorband N, et al. Inspiral-Merger-Ringdown Waveforms for Black-Hole Binaries with Nonprecessing Spins. Phys Rev Lett. 2011 Jun;106:241101. Available from: https://link.aps.org/doi/10.1103/PhysRevLett.106.241101.

[72] Santamaría L, Ohme F, Ajith P, Brügmann B, Dorband N, Hannam M, et al. Matching post-Newtonian and numerical relativity waveforms: Systematic errors and a new phenomenological model for nonprecessing black hole binaries. Phys Rev D. 2010 Sep;82:064016. Available from: https://link.aps.org/doi/10.1103/PhysRevD.82.064016.

[73] Husa S, et al. Frequency-domain gravitational waves from nonprecessing black-hole binaries. I. New numerical waveforms and anatomy of the signal. Phys Rev D. 2016 Feb;93:044006. Available from: https://link.aps.org/doi/10.1103/PhysRevD.93.044006.

[74] Khan S, Husa S, Hannam M, Ohme F, Pürrer M, Forteza XJ, et al. Frequency-domain gravitational waves from nonprecessing black-hole binaries. II. A phenomenological model for the advanced detector era. Phys Rev D. 2016 Feb;93:044007. Available from: https://link.aps.org/doi/10.1103/PhysRevD.93.044007.

[75] Pratten G, Husa S, García-Quirós C, Colleoni M, Ramos-Buades A, Estellés H, et al. Setting the cornerstone for a family of models for gravitational waves from compact binaries: The dominant harmonic for nonprecessing quasicircular black holes. Phys Rev D. 2020 Sep;102:064001. Available from: https://link.aps.org/doi/10.1103/PhysRevD.102.064001.

[76] García-Quirós C, Colleoni M, Husa S, Estellés H, Pratten G, Ramos-Buades A, et al. Multimode frequency-domain model for the gravitational wave signal from nonprecessing black-hole binaries. Phys Rev D. 2020 Sep;102:064002. Available from: https://link.aps.org/doi/10.1103/PhysRevD.102.064002.

[77] Dietrich T , Khan S , Dudi R , Kapadia S , Kumar P , Nagar A , Ohme F , Pannarale F , Samajdar A , Bernuzzi S , Carullo G , Del Pozzo W , Haney M , Markakis C , Pürrer M , Riemenschneider G , Setyawati Y , Tsang K W , Van Den Broeck C . Matter imprints in waveform models for neutron star binaries: Tidal and self-spin effects. Phys Rev D. 2019 Jan;99:024029. Available from: https://link.aps.org/doi/10.1103/PhysRevD.99.024029.

[78] Khan S, Chatziioannou K, Hannam M, Ohme F. Phenomenological model for the gravitational-wave signal from precessing binary black holes with two-spin effects. Phys Rev D. 2019 Jul;100:024059. Available from: https://link.aps.org/doi/10.1103/PhysRevD.100.024059.

[79] Blackman J, et al. Numerical relativity waveform surrogate model for generically precessing binary black hole mergers. Phys Rev D. 2017 Jul;96:024058. Available from: https://link.aps.org/doi/10.1103/PhysRevD.96.024058.

[80] Blackman J, Field SE, Galley CR, Szilágyi B, Scheel MA, Tiglio M, et al. Fast and Accurate Prediction of Numerical Relativity Waveforms from Binary Black Hole Coalescences Using Surrogate Models. Phys Rev Lett. 2015 Sep;115:121102. Available from: https://link.aps.org/doi/10.1103/PhysRevLett.115.121102.

[81] O'Shaughnessy R, Blackman J, Field SE. An architecture for efficient gravitational wave parameter estimation with multimodal linear surrogate models. Classical and Quantum Gravity. 2017;34(14):144002. Available from: http://stacks.iop.org/0264-9381/34/i=14/a=144002.

[82] Varma V, Field SE, Scheel MA, Blackman J, Gerosa D, Stein LC, et al. Surrogate models for precessing binary black hole simulations with unequal masses. Phys Rev Research. 2019 Oct;1:033015. Available from: https://link.aps.org/doi/10.1103/PhysRevResearch.1.033015.

[83] Varma V, Field SE, Scheel MA, Blackman J, Kidder LE, Pfeiffer HP. Surrogate model of hybridized numerical relativity binary black hole waveforms. Phys Rev D. 2019 Mar;99:064045. Available from: https://link.aps.org/doi/10.1103/PhysRevD.99.064045.

[84] Islam T, Varma V, Lodman J, Field SE, Khanna G, Scheel MA, et al. Eccentric binary black hole surrogate models for the gravitational waveform and remnant properties: Comparable mass, nonspinning case. Phys Rev D. 2021 Mar;103:064022. Available from: https://link.aps.org/doi/10.1103/PhysRevD.103.064022.

[85] Damour T. Introductory lectures on the Effective One Body formalism; 2008. Available from: https://doi.org/10.1142/S0217751X08039992.

[86] Setyawati Y, Ohme F, Khan S. Enhancing gravitational waveform models through dynamic calibration. Phys Rev D. 2019 Jan;99:024010. Available from: https://link.aps.org/doi/10.1103/PhysRevD.99.024010.

[87] Khan S, Ohme F, Chatziioannou K, Hannam M. Including higher order multipoles in gravitational-wave models for precessing binary black holes. Phys Rev D. 2020 Jan;101:024056. Available from: https://link.aps.org/doi/10.1103/PhysRevD.101.024056.

[88] Field SE, Galley CR, Hesthaven JS, Kaye J, Tiglio M. Fast Prediction and Evaluation of Gravitational Waveforms Using Surrogate Models. Phys Rev X. 2014 Jul;4:031006. Available from: https://link.aps.org/doi/10.1103/PhysRevX.4.031006.

[89] Pürrer M. Frequency-domain reduced order models for gravitational waves from aligned-spin compact binaries. Classical and Quantum Gravity. 2014 September;31:195010. Available from: http://iopscience.iop.org/article/10.1088/0264-9381/31/19/195010/pdf.

[90] Pürrer M. Frequency domain reduced order model of aligned-spin effective-one-body waveforms with generic mass ratios and spins. Phys Rev D. 2016 Mar;93:064041. Available from: https://link.aps.org/doi/10.1103/PhysRevD.93.064041.

[91] Cannon K, Chapman A, Hanna C, Keppel D, Searle AC, Weinstein AJ. Singular value decomposition applied to compact binary coalescence gravitational-wave signals. Phys Rev D. 2010 Aug;82:044025. Available from: https://link.aps.org/doi/10.1103/PhysRevD.82.044025.

[92] Cannon K, et al. Efficiently enclosing the compact binary parameter space by singular-value decomposition. Phys Rev D. 2011 Oct;84:084003. Available from: https://link.aps.org/doi/10.1103/PhysRevD.84.084003.

[93] Cannon K, Hanna C, Keppel D. Interpolating compact binary waveforms using the singular value decomposition. Phys Rev D. 2012 Apr;85:081504. Available from: https://link.aps.org/doi/10.1103/PhysRevD.85.081504.

[94] Smith RJE, Cannon K, Hanna C, Keppel D, Mandel I. Towards rapid parameter estimation on gravitational waves from compact binaries using interpolated waveforms. Phys Rev D. 2013 Jun;87:122002. Available from: https://link.aps.org/doi/10.1103/PhysRevD.87.122002.

[95] Setyawati Y, Pürrer M, Ohme F. Regression methods in waveform modeling: a comparative study. Classical and Quantum Gravity. 2020 mar;37(7):075012. Available from: https://doi.org/10.1088%2F1361-6382%2Fab693b.

[96] Ashton G, Talbot C. Bilby-MCMC: An MCMC sampler for gravitational-wave inference; 2021.

[97] Smith R, Field SE, Blackburn K, Haster CJ, Pürrer M, Raymond V, et al. Fast and accurate inference on gravitational waves from precessing compact binaries. Phys Rev D. 2016 Aug;94:044031. Available from: https://link.aps.org/doi/10.1103/PhysRevD.94.044031.

[98] Antil H, Chen D, Field S. A Note on QR-Based Model Reduction: Algorithm, Software, and Gravitational Wave Applications. Computing in Science Engineering. 2018;20(4):10–25.

[99] Field S. GreedyCpp; 2020. Available from: https://bitbucket.org/sfield83/greedycpp/src/master/.

[100] Qi H, Raymond V. PyROQ: a Python-based Reduced Order Quadrature Building Code for Fast Gravitational Wave Inference; 2021.

[101] Qi H. PyROQ; 2020. Available from: https://github.com/qihongcat/PyROQ.

[102] Workshop on Reduced Order Gravitational-Wave Modeling; 2018. https://workshops.aei.mpg.de/gw-rom-roq/.

[103] Abbott R, et al. GW190521: A Binary Black Hole Merger with a Total Mass of 150 $M_{\odot}$. Phys Rev Lett. 2020 Sep;125:101102. Available from: https://link.aps.org/doi/10.1103/PhysRevLett.125.101102.

[104] Abbott R, et al. Properties and Astrophysical Implications of the 150 M ⊙ Binary Black Hole Merger GW190521. The Astrophysical Journal. 2020 sep;900(1):L13. Available from: https://doi.org/10.3847/2041-8213/aba493.

[105] Setyawati Y, Ohme F. Yoshinta/pyrex; 2021. doi:10.5281/zenodo.8475. Available from: https://zenodo.org/badge/latestdoi/246883158.

[106] Khan, Sebastian and Green, Rhys. Gravitational-wave surrogate models powered by artificial neural networks. Phys Rev D. 2021 Mar;103:064015. Available from: https://link.aps.org/doi/10.1103/PhysRevD.103.064015.

[107] Williams, D and Heng, I S and Gair, J and Clark, J A and Khamesra, B . Precessing numerical relativity waveform surrogate model for binary black holes: A Gaussian process regression approach. Phys Rev D. 2020 Mar;101:063011. Available from: https://link.aps.org/doi/10.1103/PhysRevD.101.063011.

[108] Huerta EA, Moore CJ, Kumar P, George D, Chua AJK, Haas R, et al. Eccentric, nonspinning, inspiral, Gaussian-process merger approximant for the detection and characterization of eccentric binary black hole mergers. Phys Rev D. 2018 Jan;97:024031. Available from: https://link.aps.org/doi/10.1103/PhysRevD.97.024031.

[109] Chua, Alvin J K and Galley, Chad R and Vallisneri, Michele. Reduced-Order Modeling with Artificial Neurons for Gravitational-Wave Inference. Phys Rev Lett. 2019 May;122:211101. Available from: https://link.aps.org/doi/10.1103/PhysRevLett.122.211101.

Appendix

A
Notations and conventions

A.1 Conventions in this dissertation

δ_{ij} Kronecker delta, where $\delta_{ij} = 1$, for $(i = j)$, otherwise zero,
z^* complex conjugate of z,
:= imposed absolute equality,
≡ derived absolute equality,
$\mathcal{R}x$ real part of x,
$\mathcal{I}x$ imaginary part of x,
$\vec{x}$ vector of x,
η=(-1,1,1,1).

A.2 Units

Throughout this dissertation, geometric units $G = c = 1$ are used. In SI units, these measurement corresponds to:

$$G = 6.67259 \times 10^{-11} \frac{\mathrm{m}^3}{\mathrm{kg\ s}^2}, \tag{A.1}$$

$$c = 2.99792458 \times 10^{8} \frac{\mathrm{m}}{\mathrm{sec}}, \tag{A.2}$$

$$1\mathrm{M}_\odot = 1.98892 \times 10^{30}\mathrm{kg} \tag{A.3}$$

$$= 1476.63\mathrm{m} \tag{A.4}$$

$$= 4.92549 \times 10^{-6}\mathrm{seconds}, \tag{A.5}$$

$$1\mathrm{Mpc} = 3.08568025 \times 10^{22}\mathrm{m}. \tag{A.6}$$

A.3 Fourier transforms

The convention for the Fourier transforms $\tilde{s}(f)$ of a continuous time signal $s(t)$ follows these expression:

$$\tilde{s}(f) \coloneqq \int_{-\infty}^{\infty} s(t) e^{-2\pi i f t}\, dt, \tag{A.7}$$

$$s(t) \equiv \int_{-\infty}^{\infty} \tilde{s}(f) e^{2\pi i f t}\, df. \tag{A.8}$$

B
LIGO Virgo detections

Event	$m_1/M_\odot$	$m_2/M_\odot$	$\mathcal{M}/M_\odot$	$\chi_{\rm eff}$	$M_f/M_\odot$	a_f	$E_{\rm rad}/(M_\odot c^2)$	$\ell_{\rm peak}/({\rm erg\,s^{-1}})$	$d_L/{\rm Mpc}$	z	$\Delta\Omega/{\rm deg}^2$
GW150914	$35.6^{+4.7}_{-3.1}$	$30.6^{+3.0}_{-4.4}$	$28.6^{+1.7}_{-1.5}$	$-0.01^{+0.12}_{-0.13}$	$63.1^{+3.4}_{-3.0}$	$0.69^{+0.05}_{-0.04}$	$3.1^{+0.4}_{-0.4}$	$3.6^{+0.4}_{-0.4}\times10^{56}$	440^{+150}_{-170}	$0.09^{+0.03}_{-0.03}$	182
GW151012	$23.2^{+14.9}_{-5.5}$	$13.6^{+4.1}_{-4.8}$	$15.2^{+2.1}_{-1.2}$	$0.05^{+0.31}_{-0.20}$	$35.6^{+10.8}_{-3.8}$	$0.67^{+0.13}_{-0.11}$	$1.6^{+0.6}_{-0.5}$	$3.2^{+0.8}_{-1.7}\times10^{56}$	1080^{+550}_{-490}	$0.21^{+0.09}_{-0.09}$	1523
GW151226	$13.7^{+8.8}_{-3.2}$	$7.7^{+2.2}_{-2.5}$	$8.9^{+0.3}_{-0.3}$	$0.18^{+0.20}_{-0.12}$	$20.5^{+6.4}_{-1.5}$	$0.74^{+0.07}_{-0.05}$	$1.0^{+0.1}_{-0.2}$	$3.4^{+0.7}_{-1.7}\times10^{56}$	450^{+180}_{-190}	$0.09^{+0.04}_{-0.04}$	1033
GW170104	$30.8^{+7.3}_{-5.6}$	$20.0^{+4.9}_{-4.6}$	$21.4^{+2.2}_{-1.8}$	$-0.04^{+0.17}_{-0.21}$	$48.9^{+5.1}_{-4.0}$	$0.66^{+0.08}_{-0.11}$	$2.2^{+0.5}_{-0.5}$	$3.3^{+0.6}_{-1.0}\times10^{56}$	990^{+440}_{-430}	$0.20^{+0.08}_{-0.08}$	921
GW170608	$11.0^{+5.5}_{-1.7}$	$7.6^{+1.4}_{-2.2}$	$7.9^{+0.2}_{-0.2}$	$0.03^{+0.19}_{-0.07}$	$17.8^{+3.4}_{-0.7}$	$0.69^{+0.04}_{-0.04}$	$0.9^{+0.0}_{-0.1}$	$3.5^{+0.4}_{-1.3}\times10^{56}$	320^{+120}_{-110}	$0.07^{+0.02}_{-0.02}$	392
GW170729	$50.2^{+16.2}_{-10.2}$	$34.0^{+9.1}_{-10.1}$	$35.4^{+6.5}_{-4.8}$	$0.37^{+0.21}_{-0.25}$	$79.5^{+14.7}_{-10.2}$	$0.81^{+0.07}_{-0.13}$	$4.8^{+1.7}_{-1.7}$	$4.2^{+0.9}_{-1.5}\times10^{56}$	2840^{+1400}_{-1360}	$0.49^{+0.19}_{-0.21}$	1041
GW170809	$35.0^{+8.3}_{-5.9}$	$23.8^{+5.1}_{-5.2}$	$24.9^{+2.1}_{-1.7}$	$0.08^{+0.17}_{-0.17}$	$56.3^{+5.2}_{-3.8}$	$0.70^{+0.08}_{-0.09}$	$2.7^{+0.6}_{-0.6}$	$3.5^{+0.6}_{-0.9}\times10^{56}$	1030^{+320}_{-390}	$0.20^{+0.05}_{-0.07}$	308
GW170814	$30.6^{+5.6}_{-3.0}$	$25.2^{+2.8}_{-4.0}$	$24.1^{+1.4}_{-1.1}$	$0.07^{+0.12}_{-0.12}$	$53.2^{+3.2}_{-2.4}$	$0.72^{+0.07}_{-0.05}$	$2.7^{+0.4}_{-0.3}$	$3.7^{+0.4}_{-0.5}\times10^{56}$	600^{+150}_{-220}	$0.12^{+0.03}_{-0.04}$	87
GW170817	$1.46^{+0.12}_{-0.10}$	$1.27^{+0.09}_{-0.09}$	$1.186^{+0.001}_{-0.001}$	$0.00^{+0.02}_{-0.01}$	≤ 2.8	≤ 0.89	≥ 0.04	$\geq 0.1\times10^{56}$	40^{+7}_{-15}	$0.01^{+0.00}_{-0.00}$	16
GW170818	$35.4^{+7.5}_{-4.7}$	$26.7^{+4.3}_{-5.2}$	$26.5^{+2.1}_{-1.7}$	$-0.09^{+0.18}_{-0.21}$	$59.4^{+4.9}_{-3.8}$	$0.67^{+0.07}_{-0.08}$	$2.7^{+0.5}_{-0.5}$	$3.4^{+0.5}_{-0.7}\times10^{56}$	1060^{+420}_{-380}	$0.21^{+0.07}_{-0.07}$	39
GW170823	$39.5^{+11.2}_{-6.7}$	$29.0^{+6.7}_{-7.8}$	$29.2^{+4.6}_{-3.6}$	$0.09^{+0.22}_{-0.26}$	$65.4^{+10.1}_{-7.4}$	$0.72^{+0.09}_{-0.12}$	$3.3^{+1.0}_{-0.9}$	$3.6^{+0.7}_{-1.1}\times10^{56}$	1940^{+970}_{-900}	$0.35^{+0.15}_{-0.15}$	1666

Table B.1: List of GW events during the first and second observing runs (2015-2017). 10 BBH and 1 BNS collisions were detected [27]. The numbers show the median value with 90% credible intervals, where m_1 and m_2 are the masses of the heavier and lighter BH, $\mathcal{M}$ is the chirp mass, χ_{eff} is the dimensionless spin effective, M_f and a_f denote the final source-frame mass and spin that emits radiated Energy E_{rad} and peak luminosity ℓ_{peak} at distance d_L and redshift z, and sky localization $\Delta\Omega$. We discuss the GW parameters further in Section 2.3 and the conversion to SI units can be found in Appendix. A

Event	M ($M_\odot$)	$\mathcal{M}$ ($M_\odot$)	m_1 ($M_\odot$)	m_2 ($M_\odot$)	$\chi_{\rm eff}$	$D_{\rm L}$ (Gpc)	z	$M_{\rm f}$ ($M_\odot$)	$\chi_{\rm f}$	$\Delta\Omega$ (deg^2)	SNR
GW190408_181802	$43.0^{+4.2}_{-3.0}$	$18.3^{+1.9}_{-1.2}$	$24.6^{+5.1}_{-3.4}$	$18.4^{+3.3}_{-3.6}$	$-0.03^{+0.14}_{-0.19}$	$1.55^{+0.40}_{-0.60}$	$0.29^{+0.06}_{-0.10}$	$41.1^{+3.9}_{-2.8}$	$0.67^{+0.06}_{-0.07}$	150	$15.3^{+0.2}_{-0.3}$
GW190412	$38.4^{+3.8}_{-3.7}$	$13.3^{+0.4}_{-0.3}$	$30.1^{+4.7}_{-5.1}$	$8.3^{+1.6}_{-0.9}$	$0.25^{+0.08}_{-0.11}$	$0.74^{+0.14}_{-0.17}$	$0.15^{+0.03}_{-0.03}$	$37.3^{+3.9}_{-3.8}$	$0.67^{+0.05}_{-0.06}$	21	$18.9^{+0.2}_{-0.3}$
GW190413_052954	$58.6^{+13.3}_{-9.7}$	$24.6^{+5.5}_{-4.1}$	$34.7^{+12.6}_{-8.1}$	$23.7^{+7.3}_{-6.7}$	$-0.01^{+0.29}_{-0.34}$	$3.55^{+2.27}_{-1.66}$	$0.59^{+0.29}_{-0.24}$	$56.0^{+12.5}_{-9.2}$	$0.68^{+0.12}_{-0.13}$	1500	$8.9^{+0.4}_{-0.7}$
GW190413_134308	$78.8^{+17.4}_{-11.9}$	$33.0^{+8.2}_{-5.4}$	$47.5^{+13.5}_{-10.7}$	$31.8^{+11.7}_{-10.8}$	$-0.03^{+0.25}_{-0.29}$	$4.45^{+2.48}_{-2.12}$	$0.71^{+0.31}_{-0.30}$	$75.5^{+16.4}_{-11.4}$	$0.68^{+0.10}_{-0.12}$	730	$10.0^{+0.4}_{-0.5}$
GW190421_213856	$72.9^{+13.4}_{-9.2}$	$31.2^{+5.9}_{-4.2}$	$41.3^{+10.4}_{-6.9}$	$31.9^{+8.0}_{-8.8}$	$-0.06^{+0.22}_{-0.27}$	$2.88^{+1.37}_{-1.38}$	$0.49^{+0.19}_{-0.21}$	$69.7^{+12.5}_{-8.7}$	$0.67^{+0.10}_{-0.11}$	1200	$10.7^{+0.2}_{-0.4}$
GW190424_180648	$72.6^{+13.3}_{-10.7}$	$31.0^{+5.8}_{-4.6}$	$40.5^{+11.1}_{-7.3}$	$31.8^{+7.6}_{-7.7}$	$0.13^{+0.22}_{-0.22}$	$2.20^{+1.58}_{-1.16}$	$0.39^{+0.23}_{-0.19}$	$68.9^{+12.4}_{-10.1}$	$0.74^{+0.09}_{-0.09}$	28000	$10.4^{+0.2}_{-0.4}$
GW190425	$3.4^{+0.3}_{-0.1}$	$1.44^{+0.02}_{-0.02}$	$2.0^{+0.6}_{-0.3}$	$1.4^{+0.3}_{-0.3}$	$0.06^{+0.11}_{-0.05}$	$0.16^{+0.07}_{-0.07}$	$0.03^{+0.01}_{-0.02}$	–	–	10000	$12.4^{+0.3}_{-0.4}$
GW190426_152155	$7.2^{+3.5}_{-1.5}$	$2.41^{+0.08}_{-0.08}$	$5.7^{+3.9}_{-2.3}$	$1.5^{+0.8}_{-0.5}$	$-0.03^{+0.32}_{-0.30}$	$0.37^{+0.18}_{-0.16}$	$0.08^{+0.04}_{-0.03}$	–	–	1300	$8.7^{+0.5}_{-0.6}$
GW190503_185404	$71.7^{+9.4}_{-8.3}$	$30.2^{+4.2}_{-4.2}$	$43.3^{+9.2}_{-8.1}$	$28.4^{+7.7}_{-8.0}$	$-0.03^{+0.20}_{-0.26}$	$1.45^{+0.69}_{-0.63}$	$0.27^{+0.11}_{-0.11}$	$68.6^{+8.8}_{-7.7}$	$0.66^{+0.09}_{-0.12}$	94	$12.4^{+0.2}_{-0.3}$
GW190512_180714	$35.9^{+3.8}_{-3.5}$	$14.6^{+1.3}_{-1.0}$	$23.3^{+5.3}_{-5.8}$	$12.6^{+3.6}_{-2.5}$	$0.03^{+0.12}_{-0.13}$	$1.43^{+0.55}_{-0.55}$	$0.27^{+0.09}_{-0.10}$	$34.5^{+3.8}_{-3.5}$	$0.65^{+0.07}_{-0.07}$	220	$12.2^{+0.2}_{-0.4}$
GW190513_205428	$53.9^{+8.6}_{-5.9}$	$21.6^{+3.8}_{-1.9}$	$35.7^{+9.5}_{-9.2}$	$18.0^{+7.7}_{-4.1}$	$0.11^{+0.28}_{-0.17}$	$2.06^{+0.88}_{-0.80}$	$0.37^{+0.13}_{-0.13}$	$51.6^{+8.2}_{-5.8}$	$0.68^{+0.14}_{-0.12}$	520	$12.9^{+0.3}_{-0.4}$
GW190514_065416	$67.2^{+18.7}_{-10.8}$	$28.5^{+7.9}_{-4.8}$	$39.0^{+14.7}_{-8.2}$	$28.4^{+9.3}_{-8.8}$	$-0.19^{+0.29}_{-0.32}$	$4.13^{+2.65}_{-2.17}$	$0.67^{+0.33}_{-0.31}$	$64.5^{+17.9}_{-10.4}$	$0.63^{+0.11}_{-0.15}$	3000	$8.2^{+0.3}_{-0.6}$
GW190517_055101	$63.5^{+9.6}_{-9.6}$	$26.6^{+4.0}_{-4.0}$	$37.4^{+11.7}_{-7.6}$	$25.3^{+7.0}_{-7.3}$	$0.52^{+0.19}_{-0.19}$	$1.86^{+1.62}_{-0.84}$	$0.34^{+0.24}_{-0.14}$	$59.3^{+9.1}_{-8.9}$	$0.87^{+0.05}_{-0.07}$	470	$10.7^{+0.4}_{-0.6}$
GW190519_153544	$106.6^{+13.5}_{-14.8}$	$44.5^{+6.4}_{-7.1}$	$66.0^{+10.7}_{-12.0}$	$40.5^{+11.0}_{-11.1}$	$0.31^{+0.20}_{-0.22}$	$2.53^{+1.83}_{-0.92}$	$0.44^{+0.25}_{-0.14}$	$101.0^{+12.4}_{-13.8}$	$0.79^{+0.07}_{-0.13}$	860	$15.6^{+0.2}_{-0.3}$
GW190521	$163.9^{+39.2}_{-23.5}$	$69.2^{+17.0}_{-10.6}$	$95.3^{+28.7}_{-18.9}$	$69.0^{+22.7}_{-23.1}$	$0.03^{+0.32}_{-0.39}$	$3.92^{+2.19}_{-1.95}$	$0.64^{+0.28}_{-0.28}$	$156.3^{+36.8}_{-22.4}$	$0.71^{+0.12}_{-0.16}$	1000	$14.2^{+0.3}_{-0.3}$
GW190521_074359	$74.7^{+7.0}_{-4.8}$	$32.1^{+3.2}_{-2.5}$	$42.2^{+5.9}_{-4.8}$	$32.8^{+5.4}_{-6.4}$	$0.09^{+0.10}_{-0.13}$	$1.24^{+0.40}_{-0.57}$	$0.24^{+0.07}_{-0.10}$	$71.0^{+6.5}_{-4.4}$	$0.72^{+0.05}_{-0.07}$	550	$25.8^{+0.1}_{-0.2}$
GW190527_092055	$59.1^{+21.3}_{-9.8}$	$24.3^{+9.1}_{-4.2}$	$36.5^{+16.4}_{-9.0}$	$22.6^{+10.5}_{-8.1}$	$0.11^{+0.28}_{-0.28}$	$2.49^{+2.48}_{-1.24}$	$0.44^{+0.34}_{-0.20}$	$56.4^{+20.2}_{-9.3}$	$0.71^{+0.12}_{-0.16}$	3700	$8.1^{+0.3}_{-0.9}$
GW190602_175927	$116.3^{+19.0}_{-15.6}$	$49.1^{+9.1}_{-8.5}$	$69.1^{+15.7}_{-13.0}$	$47.8^{+14.3}_{-17.4}$	$0.07^{+0.25}_{-0.24}$	$2.69^{+1.79}_{-1.12}$	$0.47^{+0.25}_{-0.17}$	$110.9^{+17.7}_{-14.9}$	$0.70^{+0.10}_{-0.14}$	690	$12.8^{+0.2}_{-0.3}$
GW190620_030421	$92.1^{+18.5}_{-13.1}$	$38.3^{+8.3}_{-6.5}$	$57.1^{+16.0}_{-12.7}$	$35.5^{+12.2}_{-12.3}$	$0.33^{+0.22}_{-0.25}$	$2.81^{+1.68}_{-1.31}$	$0.49^{+0.23}_{-0.20}$	$87.2^{+16.8}_{-12.1}$	$0.79^{+0.08}_{-0.15}$	7200	$12.1^{+0.3}_{-0.4}$
GW190630_185205	$59.1^{+4.6}_{-4.8}$	$24.9^{+2.1}_{-2.1}$	$35.1^{+6.9}_{-5.6}$	$23.7^{+5.2}_{-5.1}$	$0.10^{+0.12}_{-0.13}$	$0.89^{+0.56}_{-0.37}$	$0.18^{+0.10}_{-0.07}$	$56.4^{+4.4}_{-4.6}$	$0.70^{+0.05}_{-0.07}$	1200	$15.6^{+0.2}_{-0.3}$
GW190701_203306	$94.3^{+12.1}_{-9.5}$	$40.3^{+5.4}_{-4.9}$	$53.9^{+11.8}_{-8.0}$	$40.8^{+8.7}_{-12.0}$	$-0.07^{+0.23}_{-0.29}$	$2.06^{+0.76}_{-0.73}$	$0.37^{+0.11}_{-0.12}$	$90.2^{+11.3}_{-8.9}$	$0.66^{+0.09}_{-0.13}$	46	$11.3^{+0.2}_{-0.3}$
GW190706_222641	$104.1^{+20.2}_{-13.9}$	$42.7^{+10.0}_{-7.0}$	$67.0^{+14.6}_{-16.2}$	$38.2^{+14.6}_{-13.3}$	$0.28^{+0.26}_{-0.29}$	$4.42^{+2.59}_{-1.93}$	$0.71^{+0.32}_{-0.27}$	$99.0^{+18.3}_{-13.5}$	$0.78^{+0.09}_{-0.18}$	650	$12.6^{+0.2}_{-0.4}$
GW190707_093326	$20.1^{+1.9}_{-1.3}$	$8.5^{+0.6}_{-0.5}$	$11.6^{+3.3}_{-1.7}$	$8.4^{+1.4}_{-1.7}$	$-0.05^{+0.10}_{-0.08}$	$0.77^{+0.38}_{-0.37}$	$0.16^{+0.07}_{-0.07}$	$19.2^{+1.9}_{-1.3}$	$0.66^{+0.03}_{-0.04}$	1300	$13.3^{+0.2}_{-0.4}$
GW190708_232457	$30.9^{+2.5}_{-1.8}$	$13.2^{+0.9}_{-0.6}$	$17.6^{+4.7}_{-2.3}$	$13.2^{+2.0}_{-2.7}$	$0.02^{+0.10}_{-0.08}$	$0.88^{+0.33}_{-0.39}$	$0.18^{+0.06}_{-0.07}$	$29.5^{+2.5}_{-1.8}$	$0.69^{+0.04}_{-0.04}$	14000	$13.1^{+0.2}_{-0.3}$
GW190719_215514	$57.8^{+18.3}_{-10.7}$	$23.5^{+6.5}_{-4.0}$	$36.5^{+18.0}_{-10.3}$	$20.8^{+9.0}_{-7.2}$	$0.32^{+0.29}_{-0.31}$	$3.94^{+2.59}_{-2.00}$	$0.64^{+0.33}_{-0.29}$	$54.9^{+17.3}_{-10.2}$	$0.78^{+0.11}_{-0.17}$	2900	$8.3^{+0.3}_{-0.8}$
GW190720_000836	$21.5^{+4.3}_{-2.3}$	$8.9^{+0.5}_{-0.8}$	$13.4^{+6.7}_{-3.0}$	$7.8^{+2.3}_{-2.2}$	$0.18^{+0.14}_{-0.12}$	$0.79^{+0.69}_{-0.32}$	$0.16^{+0.12}_{-0.06}$	$20.4^{+4.5}_{-2.2}$	$0.72^{+0.06}_{-0.05}$	460	$11.0^{+0.3}_{-0.7}$
GW190727_060333	$67.1^{+11.7}_{-8.0}$	$28.6^{+5.3}_{-3.7}$	$38.0^{+9.5}_{-6.2}$	$29.4^{+7.1}_{-8.4}$	$0.11^{+0.26}_{-0.25}$	$3.30^{+1.54}_{-1.50}$	$0.55^{+0.21}_{-0.22}$	$63.8^{+10.9}_{-7.5}$	$0.73^{+0.10}_{-0.10}$	830	$11.9^{+0.3}_{-0.5}$
GW190728_064510	$20.6^{+4.5}_{-1.3}$	$8.6^{+0.5}_{-0.3}$	$12.3^{+7.2}_{-2.2}$	$8.1^{+1.7}_{-2.6}$	$0.12^{+0.20}_{-0.07}$	$0.87^{+0.26}_{-0.37}$	$0.18^{+0.05}_{-0.07}$	$19.6^{+4.7}_{-1.3}$	$0.71^{+0.04}_{-0.04}$	400	$13.0^{+0.2}_{-0.4}$
GW190731_140936	$70.1^{+15.8}_{-11.3}$	$29.5^{+7.1}_{-5.2}$	$41.5^{+12.2}_{-9.0}$	$28.8^{+9.7}_{-9.5}$	$0.06^{+0.24}_{-0.24}$	$3.30^{+2.39}_{-1.72}$	$0.55^{+0.31}_{-0.26}$	$67.0^{+14.6}_{-10.8}$	$0.70^{+0.10}_{-0.13}$	3400	$8.7^{+0.2}_{-0.5}$
GW190803_022701	$64.5^{+12.6}_{-9.0}$	$27.3^{+5.7}_{-4.1}$	$37.3^{+10.6}_{-7.0}$	$27.3^{+7.8}_{-8.2}$	$-0.03^{+0.24}_{-0.27}$	$3.27^{+1.95}_{-1.58}$	$0.55^{+0.26}_{-0.24}$	$61.7^{+11.8}_{-8.5}$	$0.68^{+0.10}_{-0.11}$	1500	$8.6^{+0.3}_{-0.5}$
GW190814	$25.8^{+1.0}_{-0.9}$	$6.09^{+0.06}_{-0.06}$	$23.2^{+1.1}_{-1.0}$	$2.59^{+0.08}_{-0.09}$	$0.00^{+0.06}_{-0.06}$	$0.24^{+0.04}_{-0.05}$	$0.05^{+0.009}_{-0.010}$	$25.6^{+1.1}_{-0.9}$	$0.28^{+0.02}_{-0.02}$	19	$24.9^{+0.1}_{-0.2}$
GW190828_063405	$58.0^{+7.7}_{-4.8}$	$25.0^{+3.4}_{-2.1}$	$32.1^{+5.8}_{-4.0}$	$26.2^{+4.6}_{-4.8}$	$0.19^{+0.15}_{-0.16}$	$2.13^{+0.66}_{-0.93}$	$0.38^{+0.10}_{-0.15}$	$54.9^{+7.2}_{-4.3}$	$0.75^{+0.06}_{-0.07}$	520	$16.2^{+0.2}_{-0.3}$
GW190828_065509	$34.4^{+5.4}_{-4.4}$	$13.3^{+1.2}_{-1.0}$	$24.1^{+7.0}_{-7.2}$	$10.2^{+3.6}_{-2.1}$	$0.08^{+0.16}_{-0.16}$	$1.60^{+0.62}_{-0.60}$	$0.30^{+0.10}_{-0.10}$	$33.1^{+5.5}_{-4.5}$	$0.65^{+0.08}_{-0.08}$	660	$10.0^{+0.3}_{-0.5}$
GW190909_114149	$75.0^{+55.9}_{-17.6}$	$30.9^{+17.2}_{-7.5}$	$45.8^{+52.7}_{-13.3}$	$28.3^{+13.4}_{-12.7}$	$-0.06^{+0.37}_{-0.36}$	$3.77^{+3.27}_{-2.22}$	$0.62^{+0.41}_{-0.33}$	$72.0^{+54.9}_{-16.8}$	$0.66^{+0.15}_{-0.20}$	4700	$8.1^{+0.4}_{-0.6}$
GW190910_112807	$79.6^{+9.3}_{-9.1}$	$34.3^{+4.1}_{-4.1}$	$43.9^{+7.6}_{-6.1}$	$35.6^{+6.3}_{-7.2}$	$0.02^{+0.18}_{-0.18}$	$1.46^{+1.03}_{-0.58}$	$0.28^{+0.16}_{-0.10}$	$75.8^{+8.5}_{-8.6}$	$0.70^{+0.08}_{-0.07}$	11000	$14.1^{+0.2}_{-0.3}$
GW190915_235702	$59.9^{+7.5}_{-6.4}$	$25.3^{+3.2}_{-2.7}$	$35.3^{+9.5}_{-6.4}$	$24.4^{+5.6}_{-6.1}$	$0.02^{+0.20}_{-0.25}$	$1.62^{+0.71}_{-0.61}$	$0.30^{+0.11}_{-0.10}$	$57.2^{+7.1}_{-6.0}$	$0.70^{+0.09}_{-0.11}$	400	$13.6^{+0.2}_{-0.3}$
GW190924_021846	$13.9^{+5.1}_{-1.0}$	$5.8^{+0.2}_{-0.2}$	$8.9^{+7.0}_{-2.0}$	$5.0^{+1.4}_{-1.9}$	$0.03^{+0.30}_{-0.09}$	$0.57^{+0.22}_{-0.22}$	$0.12^{+0.04}_{-0.04}$	$13.3^{+5.2}_{-1.0}$	$0.67^{+0.05}_{-0.05}$	360	$11.5^{+0.3}_{-0.4}$
GW190929_012149	$104.3^{+34.9}_{-25.2}$	$35.8^{+14.9}_{-8.2}$	$80.8^{+33.0}_{-33.2}$	$24.1^{+19.3}_{-10.6}$	$0.01^{+0.34}_{-0.33}$	$2.13^{+3.65}_{-1.05}$	$0.38^{+0.49}_{-0.17}$	$101.5^{+33.6}_{-25.3}$	$0.66^{+0.20}_{-0.31}$	2200	$10.1^{+0.6}_{-0.8}$
GW190930_133541	$20.3^{+8.9}_{-1.5}$	$8.5^{+0.5}_{-0.5}$	$12.3^{+12.4}_{-2.3}$	$7.8^{+1.7}_{-3.3}$	$0.14^{+0.31}_{-0.15}$	$0.76^{+0.36}_{-0.32}$	$0.15^{+0.06}_{-0.06}$	$19.4^{+9.2}_{-1.5}$	$0.72^{+0.07}_{-0.06}$	1700	$9.5^{+0.3}_{-0.5}$

Table B.2: 38 BBHs and 1 BNS candidates were detected during the first half of the third observing run (O3a), between 1 April 2019 15:00 UTC and 1 October 2019 15:00 UTC [28]. The numbers correspond to median values with 90% credible intervals. The units and parameters are the same as in Table. B.1 with SNR shows the matched filter SNR of the corresponding event.

Additional Material

Selected List of Publications

Short author list papers

- **Setyawati Y**, Ohme F. Adding eccentricity to quasicircular binary-black-hole waveform models. Phys Rev D. 2021 Jun; 103: 124011. Available from: https://link.aps.org/doi/10.1103/PhysRevD.103.124011.
- **Setyawati Y**, Pürrer M, Ohme F. Regression methods in waveform modeling: a comparative study. Classical and Quantum Gravity. 2020 mar; 37(7): 075012. Available from: https://doi.org/10.1088%2F1361-6382%2Fab693b.
- **Setyawati Y**, Ohme F, Khan S. Enhancing gravitational waveform models through dynamic calibration. Phys Rev D. 2019 Jan; 99: 024010. Available from: https://link.aps.org/doi/10.1103/PhysRevD.99.024010.
- Dietrich T, Khan S, Dudi R, Kapadia S, Kumar P, Nagar A, Ohme F, Pannarale F, Samajdar A, Bernuzzi S, Carullo G, Del Pozzo W, Haney M, Markakis C, Pürrer M, Riemenschneider G, **Setyawati Y**, Tsang KW, Van Den Broeck C. Matter imprints in waveform models for neutron star binaries: Tidal and self-spin effects. Phys Rev D. 2019 Jan; 99: 024029. Available from: https://link.aps.org/doi/10.1103/PhysRevD.99.024029.

Contribution to collaboration papers

- Abbott BP, et al. GWTC-1: A Gravitational-Wave Transient Catalog of Compact Binary Mergers Observed by LIGO and Virgo during the First and Second Observing Runs. Phys Rev X. 2019 Sep; 9: 031040. Available from: https://link.aps.org/doi/10.1103/PhysRevX.9.031040.
- Abbott BP, et al. Properties of the Binary Neutron Star Merger GW170817. Phys Rev X. 2019 Jan; 9: 011001. Available from: https://link.aps.org/doi/10.1103/PhysRevX.9.011001.

Short Curriculum Vitæ

Yoshinta Eka Setyawati

Personal

Contact	yoshinta@nikhef.nl,
	yoshinta.setyawati@gmail.com
ORCID ID	0000-0003-3718-4491
Nationality	Indonesia

Education

2017 – 2021	**PhD** in gravitational wave Physics-AEI Hannover, Germany. *Supervisor: Dr. Frank Ohme*.
2014 – 2016	**M.Sc.** in Astrophysics-Radboud University Nijmegen, Netherlands. *Supervisor: Dr. Samaya Nissanke, Prof. Dr. Gijs Nelemans*.
2004 – 2007	**B.Sc.** in Physics-Parahyangan Catholic University, Indonesia. *Supervisor: Dr. Paulus Cahyono Tjiang*.

Employment

2020 – present	Postdoc at Utrecht University, Netherlands.
2012 – 2014	Key account manager at Indofood CBP, Indonesia.
2008 – 2012	Sales (category) manager at Orang Tua Group, Indonesia.

Awards

2018	Poster winner in data analysis at the LVC meeting, USA.
2008	The best graduated student in the Physics department with graduation predicate cumlaude, March 2008.
2007	The best Physics student of the year.

Scholarships & grants

2019	CCGWA workshop travel grant at UCLA.
2015	Caltech gravitational waves summer school travel grant.
2014 – 2016	Scholarship for Master's study by the Indonesia endowment fund for education through the LPDP program.
2004 – 2008	Special admission and scholarship for B.Sc. by Unpar foundation through the PMDK program.